UNIVERSIDADE FEDERAL DE MINAS GERAIS
Programa de Pós-Graduação em Engenharia Metalúrgica, Materiais e de Minas

Master's Thesis

Microstructural Control and Evaluation of a FCC Cr-Co-Ni Multi-Principal Element Alloy with Carbon-Doping

Author: Guilherme Cardeal Stumpf
Advisor: Professor Witor Wolf
Co-advisor: Professor Francisco Gil Coury

Belo Horizonte
2023

GUILHERME CARDEAL STUMPF

Controle e Avaliação Microestrutural de uma Liga CFC de Múltiplos Elementos Principais do sistema Cr-Co-Ni com Adição de Carbono

Dissertação de mestrado apresentada ao Programa de Pós-graduação em Engenharia Metalúrgica, de Materiais e de Minas da Escola de Engenharia da Universidade Federal de Minas Gerais, como requisito parcial para a obtenção do título de mestre em Engenharia Metalúrgica, de Materiais e de Minas.

Área de Concentração: Metalurgia Física
Orientador: Professor Witor Wolf
Coorientador: Professor Francisco Gil Coury

Belo Horizonte
Universidade Federal de Minas Gerais
Escola de Engenharia
2023

S934c

Stumpf, Guilherme Cardeal.
Controle e avaliação microestrutural de uma liga CFC de múltiplos elementos principais do sistema Cr-Co-Ni com adição de carbono [recurso eletrônico] / Guilherme Cardeal Stumpf. - 2023.
1 recurso online (136 f. : il., color.) : pdf.

Orientador: Witor Wolf.
Coorientador: Francisco Gil Coury.

Dissertação (mestrado) - Universidade Federal de Minas Gerais, Escola de Engenharia.

Apêndices: f. 130-136.

Bibliografia: f. 121-129.

Exigências do sistema: Adobe Acrobat Reader.

1. Engenharia metalúrgica - Teses. 2. Metalurgia física - Teses. 3. Carbono - Teses. 4. Ligas - Teses. 5. Plástico - Deformação - Teses. I. Wolf, Witor. II. Coury, Francisco Gil. III. Universidade Federal de Minas Gerais. Escola de Engenharia. IV. Título.

CDU: 669(043)

Ficha catalográfica elaborada pela Bibliotecária Ângela Cristina Silva - CRB-6/2361
Biblioteca Prof. Mário Werneck - Escola de Engenharia da UFMG

UNIVERSIDADE FEDERAL DE MINAS GERAIS
ESCOLA DE ENGENHARIA
Programa de Pós-Graduação em Engenharia
Metalúrgica, Materiais e de Minas

PPGEM
UFMG

A dissertação intitulada **"Microstructural Control and Evaluation of a FCC Cr-Co-Ni Multi-Principal Element Alloy with Carbon-Doping"**, área de concentração: Metalurgia Física e de Transformação, apresentada pelo candidato **Guilherme Cardeal Stumpf**, para obtenção do grau de Mestre em Engenharia Metalúrgica, Materiais e de Minas, foi aprovada pela comissão examinadora constituída pelos seguintes membros:

Dr. Witor Wolf
Orientador (UFMG)

Dr. Francisco Gil Coury
Coorientador (UFSCar)

Pereira

Dr. Pedro Henrique Rodrigues Pereira
(UFMG)

gov.br
Documento assinado digitalmente
LUCAS BARCELOS OTANI
Data: 21/02/2023 10:00:32-0300
Verifique em https://verificador.iti.br

Dr. Lucas Barcelos Otani
(DEMa / UFSCar)

Daniel Majuste

____
Coordenador do Programa de Pós-Graduação em
Engenharia Metalúrgica, Materiais e de Minas/UFMG

Belo Horizonte, 17 de fevereiro de 2023

AGRADECIMENTOS

Agradeço a minha família e amigos por todo o apoio, em especial à minha mãe, Zenilda, e meu pai, Humberto.

Agradeço o meu orientador Witor Wolf por me guiar muito bem nessa jornada e por todo apoio. Agradeço o meu coorientador Francisco por apresentar para nós um novo universo da metalurgia.

Agradeço os meus amigos e colegas de laboratório por toda a parceria na minha jornada do mestrado. Em especial Laís e Malu e os meus ICs Júlia e Abraão, por toda a colaboração experimental. Agradeço também meus colegas de pós-graduação, Jéssica, Carol, Pedro, Rapha, Olavo, Denise, Miguel e tantos outros, por todas as dicas e trocas.

Agradeço os meus professores por toda a ajuda dada e todo ensinamento passado. Em especial aos professores Pedro, Dagoberto, Eduardo e Berenice.

Agradeço os técnicos sem os quais esse trabalho não seria possível. Em especial à Patrícia e ao Samuel. Agradeço, também, o Centro de Microscopia da UFMG e CNPEM pelas análises.

Finalmente, agradeço as agências de fomento que financiaram este projeto. O presente trabalho foi realizado com apoio da Coordenação de Aperfeiçoamento de Pessoal de Nível Superior - Brasil (CAPES) - Código de Financiamento 88887.621834/2021-00. Este trabalho também foi apoiado pela Fundação de Amparo à Pesquisa do Estado de São Paulo (FAPESP), números de concessão 2021/04302-8 e 2022/02770-7.

ABSTRACT

The multi-principal element alloys (MPEAs) field is characterized by a change in conception for the design of new materials. By exploring compositions with three or more elements in high concentrations, the limit of possibilities compared to conventional alloys is expanded. In recent years, Cr-Co-Ni fcc (face-centered cubic) alloys have drawn significant attention due to their high mechanical properties, corrosion resistance, and especially due to their toughness ranking amongst the highest of all known materials. This work aims to study the effects of carbon-doping to the microstructure and mechanical properties of the $Cr_{40}Co_{30}Ni_{30}$ alloy. To analyze how this element, be it in solid solution and/or in precipitates, affect the grain size control and refinement, two compositions were designed and fabricated, $Cr_{39.9}Co_{30}Ni_{30}C_{0.1}$ and $Cr_{39.1}Co_{30}Ni_{30}C_{0.4}$, respectively. Both alloys, as well as the base material, were processed in three different routes to study carbon-doping after: solution treatment, coarse (and heterogeneous) precipitation and severe plastic deformation. The microstructure and Hall-Petch relation were investigated with the aid of different characterization techniques. Carbon-doping was observed to be more effective in retarding grain growth with a prior solution treatment, resulting in a homogeneous particle distribution achieved after processing. Additionally, its contribution to hardness was mainly due to grain size refinement, with virtually no observed increments from precipitation or interstitial strengthening. Under sever plastic deformation, carbon-doping deactivated twinning induced plasticity (TWIP) and phase transformation induced plasticity (TRIP), inducing a nanostructured network of stacking faults.

Key-words: Multi-principal element alloys. Cr-Co-Ni. Carbon-doping. Hall-Petch. Microstructure evolution. Severe plastic deformation.

RESUMO

A área das ligas de múltiplos elementos principais (MPEAs) se caracteriza por uma mudança na concepção do design dos novos materiais. Ao se explorar composições contendo três ou mais elementos em altas concentrações, expande-se o limite de possibilidades quando comparado às ligas convencionais. Recentemente, ligas cfc (cúbicas de face centradas) do sistema Cr-Co-Ni têm chamado atenção devido as suas ótimas propriedades mecânicas, boa resistência à corrosão e, especialmente, à alta tenacidade que está dentre as maiores já reportadas para qualquer material conhecido. Este trabalho estuda os efeitos da adição de carbono na microestrutura e propriedades mecânicas da liga $Cr_{40}Co_{30}Ni_{30}$. Para analisar o efeito desse elemento no controle e refino do tamanho de grão, tanto em solução sólida, quanto na forma de precipitados, duas ligas foram produzidas. Sendo suas composições nominais de $Cr_{39,9}Co_{30}Ni_{30}C_{0,1}$ e $Cr_{39,6}Co_{30}Ni_{30}C_{0,4}$, respectivamente. Ambas as ligas, bem como a liga base, foram processadas em três diferentes rotas de processamento para estudar os efeitos de adição de carbono depois de: tratamento de solubilização, precipitação grosseira (e heterogênea) e deformação plástica severa. A microestrutura e relação de Hall-Petch foram investigadas através do auxílio de diferentes técnicas de caracterização. Observou-se que a adição de carbono foi mais efetiva em retardar crescimento de grão quando aplicada uma etapa de solubilização, resultando em uma distribuição homogênea de precipitados ao final do processamento. Além disso, a sua contribuição para a dureza foi principalmente devido ao refino de grão, com virtualmente nenhum incremento referente ao endurecimento por solução sólida ou precipitação. Durante deformação plástica severa o carbono adicionado resultou em uma desativação da maclação induzida e transformação de fase induzidas por deformação, induzindo, assim, a formação de um arranjo nano-estruturado de falhas de empilhamento.

Palavras-Chave: Ligas de múltiplos elementos principais. Cr-Co-Ni. Adição de carbono. Hall-Petch. Evolução microestrutural. Deformação plástica severa.

SUMMARY

1 INTRODUCTION AND MOTIVATION

Metallurgy is the science of metals, starting in the extraction of the wanted elements from ores, to refinement, to final processing, metallography and beyond. The noble metals gold and silver, as well as copper, were the first know metals to be utilized, and for esthetic reasons, mainly as ornaments, or as tools in varied forms [1].

However, it was not until the bronze age, with evidences ranging from before 3000 B.C., that a very revolutionary concept, for both metallurgy and humanity alike, arose. Even if it was not as intentional or as technical and scientifical as today, the alloy concept helped advance the civilizations and cultures of the world, being known as one of the great milestones in history [1].

It is simple to see that our current world would not be the same without alloys. Not only are they considerably more numerous and varied than pure metals (given that they represent a combination of the latter), but also present improved and more diverse properties. A notorious example is the iron-carbon alloys called steels, a class of materials that constitutes most of the constructions of the world, beyond many other common applications. This would not be achieved with pure iron, since its properties (mechanical, metallurgical, corrosion resistances, etc.) are less versatile compared to the range of properties from all the steel family of alloys [1].

Conventional alloys are defined as a cohesive mixture of two or more metals or other elements (with a least one metal), in which one or two elements, in higher quantities, act as the base. Until very recently, the way of making alloys only followed this premise, and so, even with a large array of possibilities, most of the conventional alloy systems of technological interest have been investigated. In contrast, research exists only for a minimal fraction of alloys with higher concentrations of additional elements [2].

Successful multicomponent systems, including those in which more than 2 elements are present in high percentages, have been studied before [3–6]. Other unsuccessful attempts were made on the late 18th century, resulting mainly in multi-brittle-phased alloys [7]. It was only in 2004 that two different research groups concurrently published works that would define the idealization of new approaches to alloy development, and thus, the field of multi-principal element alloys (MPEAs) commenced [8,9]. As the name suggests, more than one element acts as the principal element in these alloys, and this is achieved in solid solution where the principal elements act as solutes rather than solvent [7,9].

This field of "unconventional" alloys went through different naming terms, as knowledge on the subject grew. Such as, high entropy alloys (HEAs), complex concentrated alloys (CCAs), "baseless" alloys and multi-principal element alloys [2]. In this work the latter term, MPEA, will be the one adopted. Gorsse et al. [2] showed that by combining 3 to 6 main elements, choosing from the 67 stable metals in the periodic table, one could devise over 110 million possible multi-principal systems/bases. This is all without considering changes in composition or alloying (with non-principal elements) [2].

To further assess the MPEAs universe of possibilities, the other mentioned variables can also be considered in the estimation, albeit with more complex calculations. For example, to vary the principal elements' compositions with 5 % steps, and with a lower limit of also 5 % for each element, would be a new proposition. Another one could be the addition of 1 to 6 alloying elements, choosing from the 80 stable elements in the periodic table, in compositions varying from 0.1 % to 2 % each, with 0.1 % steps. The equation 1.1, created for the present study, takes all of these variables and propositions in consideration and returns the number of possible unique alloys (A).

$$A = \left[\sum_{r=3}^{6} \frac{n!}{r!\,(n-r)!} \cdot \left(\frac{(P_r + r - 2)!}{(r-1)!\,(P_r - 1)!} \right) \right] \cdot \left[\sum_{a=1}^{6} \frac{q!}{a!\,(q-a)!} \cdot \left(\frac{(P_a + a - 2)!}{(a-1)!\,(P_a - 1)!} \right) \right] \tag{1.1}$$

Where n is the total number of distinguishable principal elements to choose from (67 stable metals), r is the number of principal elements in the alloy, q is the total number of distinguishable alloying elements to choose from (80 stable elements) and "a" is the number of alloying elements in the alloy. P_r and P_a can be described as:

$$P_x = \frac{[l_s - l_i(x-1)]}{\Delta} - \frac{(l_i - \Delta)}{\Delta} \tag{1.2}$$

Where x is the variable (r or a), l_s and l_i are respectively the upper (100 % for principal elements composition and 2 % for alloying elements composition) and lower (5 % for principal elements composition and 0.1 % for alloying elements composition) bounds and Δ is the step size (5 % for principal elements and 0.1 % for alloying elements). That makes P_x the maximum number of variations between l_i to l_s for given x (r or a) and Δ.

With the parameters chosen, equation 1.1 would return a total of 4.3×10^{24} (or 4.3 septillions) distinct conceivable alloys. However, this is a mathematical proposition, it does not take into consideration other aspects, including chemical, physical and economical. For example, chemically incompatible elements, formation of brittle phases, high cost, processing difficulties, etc. All of this can hinder considerably or even invalidate a huge number of MPEAs' compositions or entire systems. Just as only a fraction of conventional alloys is truly viable commercially and industrially, the same can be said for MPEAs. Although the estimation is rough, it helps visualize the vast potential of multi-principal alloys.

The focus of this work is inserted in the Cr-Co-Ni system, one of the millions of possible MPEAs systems. The face-centered cubic (fcc) Cr-Co-Ni alloys have been reported with some exceptional mechanical and functional properties when compared to other MPEAs or conventional alloys, ranking amongst the materials with the highest recorded toughness values [10]. They represent well the promising concept of this new field of metallurgy, or better put, of this unconventional alloy design concept. The CrCoNi equiatomic alloy also has a high Hall-Petch slope [10]. This indicates that its strength and hardness increase significantly with grain size reduction, and justifies the interest in studying grain refinement for the Cr-Co-Ni alloys. As such, in an effort to increase the overall mechanical properties of Cr-Co-Ni alloys, we added carbon to an $Cr_{40}Co_{30}Ni_{30}$ alloy, to promote grain refinement with minimal loss in ductility. To further reduce grain sizes, samples were deformed via severe plastic deformation (with high-pressure torsion). In summary, the motivation behind this work was to improve the mechanical properties of the Cr-Co-Ni fcc alloys by inducing grain refinement with carbon-doping (while studying the effects of carbon in the different processing conditions).

1.1 Introdução

A metalurgia é a ciência dos metais, que começa com a extração dos elementos desejados dos minérios, passando pelo refinamento, processamento final, metalografia e além. Os metais nobres, como ouro e prata, assim como o cobre, foram os primeiros metais conhecidos a serem utilizados, principalmente por motivos estéticos, como ornamentos ou ferramentas em várias formas [1]. No entanto, foi apenas durante a Idade do Bronze, com evidências que remontam a antes de 3000 a.C., que um conceito muito revolucionário, tanto para a metalurgia quanto para a humanidade, surgiu. Mesmo que não tenha sido tão intencional, técnico e científico como é usado hoje, o conceito de liga ajudou a impulsionar as civilizações e culturas do mundo, sendo reconhecido como um dos grandes marcos na história [1].

É fácil perceber que o nosso mundo atual não seria o mesmo sem as ligas. Não apenas são consideravelmente mais numerosas e variadas do que os metais puros (por representarem uma combinação destes), mas também apresentam propriedades aprimoradas e mais diversas. Um exemplo notável são as ligas de ferro-carbono chamadas de aços, uma classe de materiais que constitui a maior parte das construções no mundo, além de muitas outras aplicações comuns. Isso não seria possível com ferro puro, uma vez que suas propriedades (mecânicas, metalúrgicas, de resistência à corrosão, etc.) são menos versáteis em comparação com a gama de propriedades de toda a família de ligas de aço [1].

As ligas convencionais são definidas como uma mistura coesa de dois ou mais metais ou outros elementos (sendo pelo menos um deles um metal), em que um ou dois elementos, em quantidades maiores, atuam como base. Até muito recentemente, a forma de produzir ligas seguia apenas essa premissa, e, assim, mesmo com uma grande variedade de possibilidades, a maioria dos sistemas de ligas convencionais de interesse tecnológico já foi investigada. Em contraste, pesquisas existem apenas para uma fração mínima de ligas com maiores concentrações de elementos adicionais [2]. Sistemas multicomponentes bem-sucedidos, incluindo aqueles em que mais de dois elementos estão presentes em altas porcentagens, foram estudados anteriormente [3-6]. Outras tentativas malsucedidas foram feitas no final do século XVIII, resultando principalmente em ligas com várias fases secundárias frágeis [7]. Somente em 2004, dois grupos de pesquisa diferentes publicaram, simultaneamente, trabalhos que definiriam a idealização de novas abordagens para o desenvolvimento de ligas e, assim, o campo das ligas de múltiplos elementos principais (MPEAs) teve início [8,9]. Como o nome sugere, mais de um elemento atua como elemento principal, e isso é alcançado em uma solução sólida, onde os elementos principais atuam como solutos, em vez de solvente [7,9].

Essas ligas "não convencionais" podem ser denominadas de diferentes maneiras como, por exemplo, ligas de alta entropia [2]. Neste trabalho, o último termo, MPEA, será o adotado. Gorsse et al. [2] demonstraram que, combinando de 3 a 6 elementos principais, escolhidos entre os 67 metais estáveis da tabela periódica, seria possível projetar mais de 110 milhões de possíveis sistemas/bases de elementos principais múltiplos. Isso sem considerar alterações na composição ou ligação com elementos não principais [2]. Para avaliar ainda mais o universo de possibilidades das MPEAs, as outras variáveis mencionadas também podem ser consideradas na estimativa, embora com cálculos mais complexos. Por exemplo, escolher as composições dos elementos principais em intervalos de 5 % (porcentagem atômica) e com um limite inferior também de 5 % para cada elemento. Outra possibilidade seria a adição de 1 a 6 elementos de liga, escolhendo entre os 80 elementos estáveis da tabela periódica, em composições variando de 0,1 % a 2 % cada, com intervalos de 0,1 %. A equação 1.1, criada para o presente estudo, leva todas essas variáveis e proposições em consideração e retorna o número de possíveis ligas únicas (A).

$$A = \left[\sum_{r=3}^{6} \frac{n!}{r!\,(n-r)!} \cdot \left(\frac{(P_r + r - 2)!}{(r-1)!\,(P_r - 1)!}\right)\right] \cdot \left[\sum_{a=1}^{6} \frac{q!}{a!\,(q-a)!} \cdot \left(\frac{(P_a + a - 2)!}{(a-1)!\,(P_a - 1)!}\right)\right] \tag{1.1}$$

Onde n é o número total de elementos principais distinguíveis para escolher (67 metais estáveis), r é o número de elementos principais na liga, q é o número total de elementos de liga distinguíveis para escolher (80 elementos estáveis) e "a" é o número de elementos de liga escolhidos. P_r e P_a podem ser descritos como:

$$P_x = \frac{[l_s - l_i(x-1)]}{\Delta} - \frac{(l_i - \Delta)}{\Delta} \tag{1.2}$$

Onde x é a variável (r ou a), l_s e l_i são respectivamente os limites superiores (100 % para a composição dos elementos principais e 2 % para a composição dos elementos de liga) e inferiores (5 % para a composição dos elementos principais e 0,1 % para a composição dos elementos de liga), e Δ é o tamanho do intervalo (5 % para os elementos principais e 0,1 % para os elementos de liga). Isso faz de P_x o número máximo de variações entre l_i e l_s para um determinado x e Δ. Com os parâmetros escolhidos, a equação 1.1 retornaria um total de $4,3 \times 10^{24}$ (ou 4,3 septilhões) ligas concebíveis distintas. No entanto, isso é uma proposição matemática e não leva em consideração outros aspectos, como os químicos, físicos e econômicos. Por exemplo: elementos quimicamente incompatíveis, formação de fases frágeis, alto custo, dificuldades de processamento, etc. Todos esses fatores podem dificultar consideravelmente ou até mesmo invalidar um grande número de composições de MPEAs ou sistemas inteiros. Assim como apenas uma fração das ligas convencionais é verdadeiramente viável comercial e industrialmente, o mesmo pode ser dito para as MPEAs. Embora a estimativa seja aproximada, ela ajuda a visualizar o vasto potencial das ligas de elementos principais múltiplos.

O foco deste trabalho está inserido no sistema Cr-Co-Ni, um dos milhões de sistemas possíveis de MPEAs. As ligas Cr-Co-Ni cfc (cúbicas de face centrada) têm sido relatadas com propriedades mecânicas e funcionais excepcionais quando comparadas a outras MPEAs ou ligas convencionais, figurando entre os materiais com os valores de tenacidade mais altos já registrados [10]. A liga equiatômica CrCoNi também apresenta uma alta inclinação de Hall-Petch [10]. Isso indica que sua resistência e dureza aumentam significativamente com a redução do tamanho de grão, justificando o interesse em estudar o refinamento de grãos para as ligas Cr-Co-Ni. Portanto, com o objetivo de aumentar as propriedades mecânicas gerais das ligas Cr-Co-Ni, adicionamos carbono a uma liga $Cr_{40}Co_{30}Ni_{30}$ para promover o refinamento de grãos com perda mínima de ductilidade. Para reduzir ainda mais o tamanho de grão, as amostras foram deformadas por meio de deformação plástica severa (por meio de torção de alta pressão). Em resumo, a motivação por trás deste trabalho foi melhorar as propriedades mecânicas das ligas fcc Cr-Co-Ni induzindo o refinamento de grãos com dopagem de carbono (enquanto estudava os efeitos do carbono nas diferentes condições de processamento).

2 OBJECTIVES

2.1 Main Objective

Study the effect of carbon-doping to the multi-principal element alloy $Cr_{40}Co_{30}Ni_{30}$, focusing on gran size refinement, microstructure and mechanical properties.

2.2 Specific Objectives

- Study the effect of the alloying elements, in solid solution and as precipitates, and different processing conditions in recrystallization and grain growth (and their parameters), as well as their effect on the microstructure and substructures;
- Study the influence of solution treatment and carbide distribution;
- Study the Hall-Petch relation, regarding grain size, twinning and hcp transformation;
- Evaluate the effects of carbon-doping after severe plastic deformation.

3 LITERATURE REVIEW

3.1 Multi-Principal Elements Alloys

The conceptions that started the MPEAs field originated from two different approaches to investigate alloys containing multiple principal components. The first was a study, by Cantor et al. [8], on equiatomic multicomponent alloys. The main idea was to assess the central regions of phase diagrams, since even for binary and ternary systems such composition ranges were not commonly studied as much. Following this concept, the authors studied different alloys containing 5 to even 20 principal elements, with a primary focus on the CrMnFeCoNi alloy. They noticed a tendence to form predominantly a face-centered cubic structure (fcc) phase, and always with considerably fewer secondary phases than the Gibbs phase rule allowed for. Alloys with Cr, Mn, Fe, Co and Ni as the principal elements are now commonly known as Cantor alloys, named after the primary author from this study [8].

The other major publication regarded as the ignition of the field was published by Yeh et al. [9]. It was the first to derive a fundamentally theorized approach, with the goal of producing alloys with multiple principal elements [9]. They discussed how, until then, there was mainly a disbelief over mixing numerous different elements together, since the general agreement was that it should progressively promote the formation of an increasing number of intermetallic compounds. Those are typically brittle and hard to process and thus would hinder the viability of alloys with large numbers of elements (principal or alloying) [7,9].

Yeh et al. theorized how the mixture entropy, which increases with increasing number of principal elements, would compensate the numerous possibilities of intermetallic compounds, favoring solid solutions. The configurational entropy is a key variable to explain this theory since it is the major component for the mixture entropy, which is often simplified by the former. This simplification is made because the other components (vibrational, magnetic dipole and electronic randomness) tend to not be as significant in value. For an equiatomic mixture with n (principal) elements, the configurational entropy per mole can be simplified as equation 3.1 demonstrates [7,9].

$$\Delta S_{conf} = -k_B ln(w) = -R\left[\frac{1}{n} ln\left(\frac{1}{n}\right) + \cdots + \frac{1}{n} ln\left(\frac{1}{n}\right)\right] = R\ ln(n) \qquad (3.1)$$

Where k_B is Boltzmann´s constant, w is the number of configurational possibilities and R is the gas constant (8,314 J/K·mol). Given this simplification, the (ideal) mixture entropy will be the same for any one mole of any equiatomic alloy with a set number of n-elements. For example, the ideal configurational entropy is 1.39R, 1.61R and 1.79R for 4, 5 and 6 elements equi-atomic alloys respectively [7,9].

The increase of the mixing entropy with the number of principal elements would favor the formation of random solid solutions, augmenting the mutual solubility between the elements. Yeh et al. noted that, by disregarding the lattice distortion energy effect from the difference in atomic sizes, phase equilibrium would depend on a balance between the mixings entropy and enthalpy [7,9]. With that, equiatomic alloys containing 5 or more elements would favor a solid solution instead of most of the system’s possible intermetallic compounds. This illustrates the importance of configurational entropies in the formation of these alloys, enhancing simple solid solution over complex systems with increased number of intermetallics [7,9]. Historically, this led to the high-entropy alloys (HEAs) concept becoming the main guideline of the MPEAs field for some time [2,7,11].

The main definitions for HEAs reside not only in the high configurational entropy concept, but also in compositions thresholds. For the first guideline, $\Delta S_{conf} \geq 1.5R$ is the lower boundary to define a HEA and, as such, it was regarded as a reasonable denomination for most MPEAs. At intermediate ΔS_{conf} values, between 1.5R and 1.0R there are medium-entropy alloys, characterizing everything bellow this as low-entropy alloys. The other definition states that, preferably, for a HEA, the compositions of each of the at least 5 major elements should be between 5 and 35 %, with the upper compositional limit for the minor elements being of 5 % [7].

Literature has debated that the HEA concept is not the best classification for MPEAs. Other effects previously regarded as secondary, like the different enthalpies’ contribution and the fact that the configurational entropy from intermetallics in these concentrated alloys tends to be significantly high, have questioned the initial entropy stabilization proposed by Yeh. As such, and considering the vastness of possibilities that MPEAs represent, the broader definitions should be preferred [2,11,12].

The high-entropy approach discussed above, together with lattice distortion, sluggish diffusion and the cocktail effect, are four concepts that governed the early understandings of HEAs (and thus, MPEAs). They are commonly known as the “four core effects” [7,10,11,13].

Different elements have different sizes and, when they randomly exist in the same structure, this will affect the lattice locally. These differences can strain the lattice making it distorted, as opposed to a pure and single element crystal, which would have all chemical bonds of same length. In a conventional single-phase alloy, substitutional and interstitial solutes are punctual sources of lattice distortion, exactly because they are atoms with different sizes to the principal element. However, in a multi-principal element solid solution all atoms act as solutes and, therefore, the lattice can be severely distorted [7,10,11,13]. Figure 3.1 exhibits an illustrative scheme of this effect on MPEAs solid solutions.

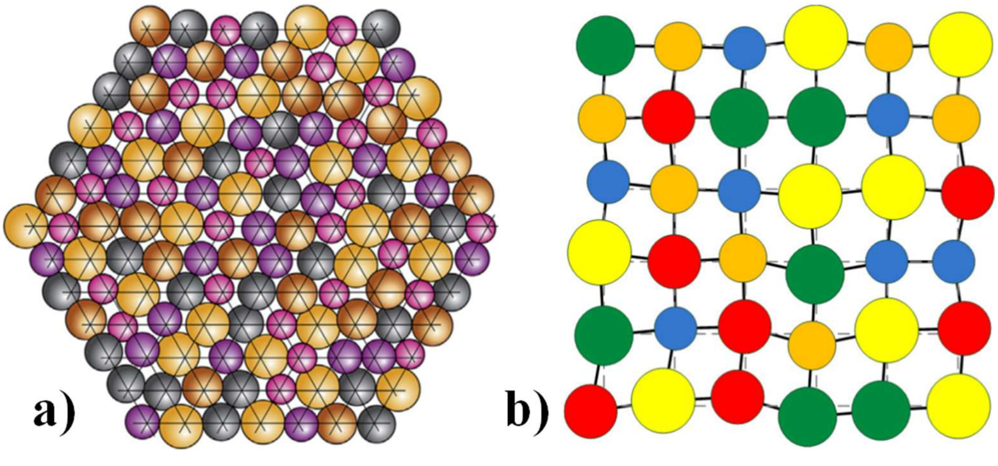

Figure 3.1. Illustrations the lattice distortion effect on multi-principal element structures. Figure (a) portrays the displacement of different atoms in regards to the lattice sites. Adapted from [11]. In (b) the distortion effect is better depicted, as it emphasizes the different bond lengths and angles of the crystal structure. Adapted from [13].

The lattice distortion explained above is one of the “core effects” mentioned. In conception, it is attributed as responsible for some general characteristics of MPEAs, such as higher strengths and hardness. This would also correlate to decreases in thermal and electrical conductivities, in X-ray diffraction peaks' intensities and in the overall thermal dependence of the alloy's properties. The type of atoms and quantity of principal elements, as well as their local configuration, will all affect the displacement in each individual lattice site and the overall distortion. In dilute solid solutions, i.e., those with a clear solvent, the displacement is significative only around solute atoms, while on MPEAs it is virtually everywhere, as can be seen in Figure 3.1 [7,10,11,13].

However, literature has shown that the lattice distortion guideline, specifically the said consequences to the final properties, can be misleading [10,11,14]. Coury et al. [10] demonstrated how a ternary MPEA can have higher lattice distortions then one with five principal elements [10]. Varvenne et al. [14] proposed a strengthening theory for fcc materials, and showed how neither the number of principal elements nor an equiatomic composition will directly result in higher strengths [14]. Miracle et al. [11] pointed out how there is insufficient study to assess how this phenomenon affects alloy properties when isolating contributions from other effects [11]. Nevertheless, it is an important phenomenon that will affect properties of the MPEAs, albeit with different magnitudes and implications for each individual alloy [10,11,14].

Sluggish diffusion is the third "core effect" theorized for HEAs. It stipulates that vacancy concentration is lower because of higher associated free energies (when compared to conventional alloys). Also, the mean path for each diffusion step will be irregular due to the atomic size differences. Thus, diffusion would be hindered [7,11,13]. Once again, other effects of the system can influence on the related properties, those being the low diffusivity rates and higher activation energies. There are studies reporting cases where the diffusion rates were lower, others where the values were in the same range of similar conventional alloys and, finally, studies where it was higher [7,10,11]. This indicates, as was for the other two core effects, that MPEAs can be significantly distinct between each other and should be studied regarding their individualities rather than uncertain generalities.

The last “core effect” is not a technical or pragmatical theory, neither does it stipulates on general properties of HEAs/MPEAs, it is but an axiom. The cocktail effect, as it is called, is the idea of finding new and advanced alloys, as well as exploring an undiscovered universe of properties and possibilities. All this from the mixture of different elements, from which the metaphor of a cocktail is conceived [7,10,11,13].

Regarding the discussion above, it becomes clear that the conceptions for these alloys are evolving over time. The MPEAs field is expanding out of the initial motivation of forming simple solid solutions, and an increased number of studies have manifested interest in complex microstructures and even solely on intermetallic compounds [2,15]. The sheer number of unexplored possibilities reflects in high hopes for the field’s versatilities in closing properties and application gaps, overcoming engineering and materials science boundaries, which are some of the main interests since its early conceptions [2,7].

3.2 Cr-Co-Ni System and Properties

The Cantor family of alloys (Cr-Mn-Fe-Co-Ni) are among the most studied multi-principal elements alloys since the field’s conception in 2004 [16]. Likewise, the sub-systems formed with 3 or 4 of its principal elements are consistently objects of study reported in international literature. The Cr-Co-Ni system caught special attention regarding its higher strengths and ductilities, for some compositions, when compared to the equiatomic alloys from the other Cantor sub-systems [10,17–20]. By presenting a good compromise between these two properties, the Cr-Co-Ni alloys, consequently, have been reported with toughness values in the highest ranges of previously studied alloys [10,20,21].

The Cr-Co-Ni alloys can be identified as medium-entropy alloys, since their maximum configurational entropy is around 1.1R (for the equiatomic alloy). They are also occasionally referred to as a part of the 3d transition MPEAs (since they are composed of transition metals on the 3d electron sub-shell block/row). Niu et al. [22] investigated the magnetic properties of the Cantor and of some of its sub-systems of alloys and concluded that the magnetic identities were a major point of influence in the overall properties. And that, the higher degree of similar magnetic properties between the CrCoNi elements, explains this alloy's superior mechanical properties when compared to the Cantor alloy and its other sub-systems [22].

To better contextualize the Cr-Co-Ni system, Coury et al. [10] plotted, by the CALPHAD (calculation of phase diagram) method, isotherms for three different temperatures, as well as the binary Cr-Co equilibrium phase diagram. These CALPHAD calculations were made with the *Pandat*^{TM} software and the PanHEA2021 database and are presented in Figure 3.2.

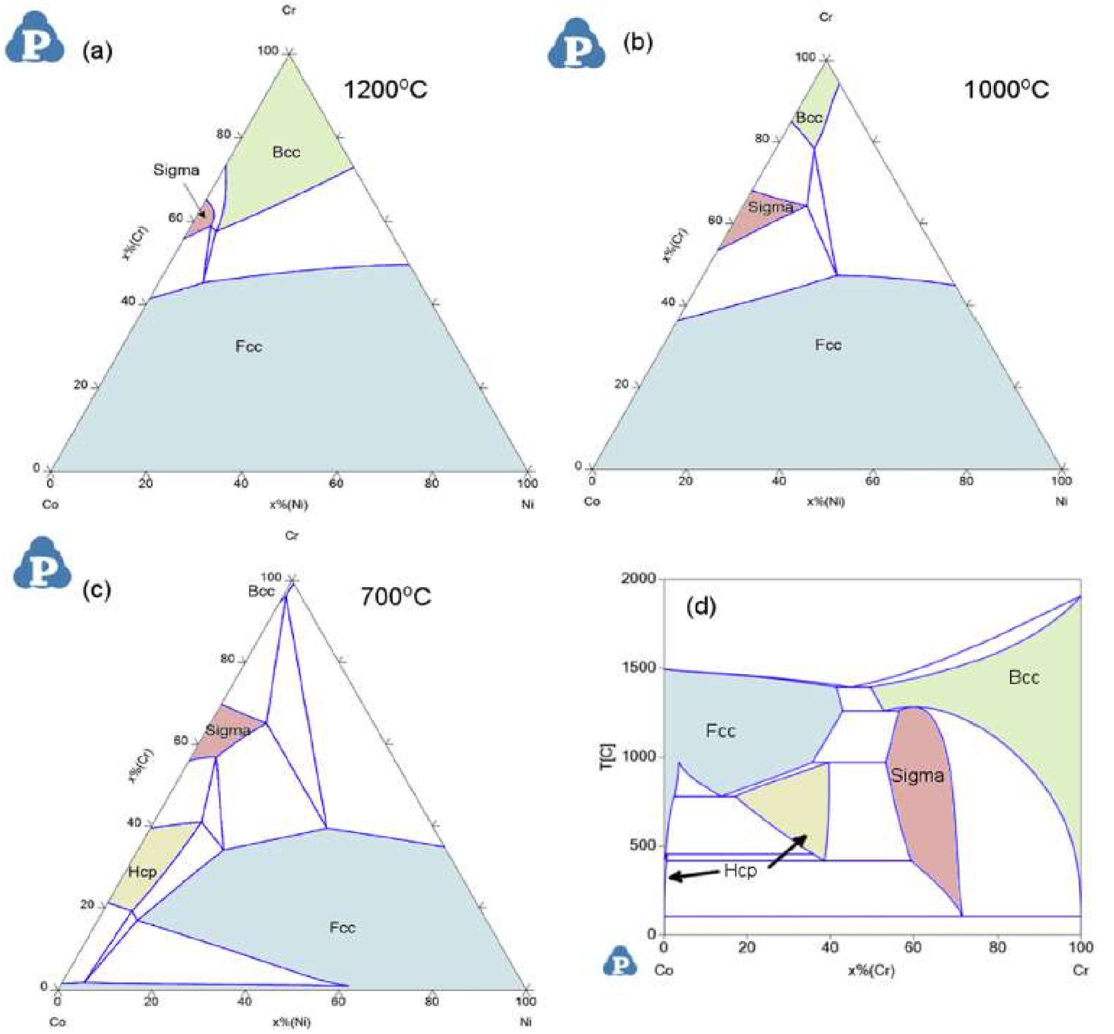

Figure 3.2. Figures (a-c) are the equilibrium isotherms for the Cr-Co-Ni ternary system at (a) 1200 °C, (b) 1000 °C and (c) 700 ºC. Figure (d) is the Cr-Co binary phase diagram. The single-phase regions are highlighted and identified. Adapted from [10].

Analyzing Figure 3.2, it is perceivable that, even though only Ni has a fcc structure at room temperature, the fcc single-phase composition field is significantly large, and is favored at higher temperatures. Besides it, base-centered cubic (bcc), sigma (which is an intermetallic phase) and close-packed hexagonal (hcp) are the other notably structures that can form in a single phase, for certain compositions. Nevertheless, the studies reported in literature, are mainly for the equiatomic alloy $Cr_{33}Co_{33}Ni_{33}$, as well as other compositions with similar components [10]. They are composed mainly of a single fcc phase in higher temperatures, as can be seen in the diagrams, but have a tendency to maintain this non-equilibrium structure even at room temperature, although the presence of sigma phase is occasionally reported [10].

Some Ni or Co based super alloys have compositions similar to the external regions of the Cr-Co-Ni ternary diagram close to these elements. One can assume that, since those alloys are commercially important, at least a part of the MPEAs alloys from this system should be viable as well, especially considering their higher mechanical properties. The relevancy of the fcc Cr-Co-Ni principal elements alloys is further encouraged due to other valuable characteristic, as reported in literature, such as excellent mechanical performances in cryogenic temperatures. Fatigue resistance showed promising results, but more studies need to be carried out for certainty. The same can be said overall for all the functional properties, since these investigations have been carried out only in a few works. Nevertheless, the alloys close to the equiatomic composition, notably those with higher Cr contents, showed very good corrosion resistances in chlorine-rich, acidic and saline environments, even when compared to the Inconel 625 alloy, a benchmark alloy for corrosion resistance. Good oxidation resistances were observed in dry environments, but not in high temperatures humid conditions [10].

3.3 Deformation Mechanisms in fcc Cr-Co-Ni Alloys

Despite the MPEAs field being very recent, it does not mean that the properties and functioning mechanisms that govern these materials will also be new and undiscovered. In fact, the deformation mechanisms of Cr-Co-Ni fcc alloys seem to operate in a very similar fashion to conventional fcc metallic materials. As such, dislocation glide is, generally, their primary plastic deformation mode. And, they can also manifest plasticity mechanisms well-known for conventional fcc alloys, depending on strain levels and phase compositions. Those being twinning induced plasticity (TWIP) and transformation induced plasticity (TRIP). Which type of mechanism will govern the deformation is highly dependable on the stress-strain state, as well as on the stacking fault energy (SFE) [10].

3.3.1 Stacking Fault Energy

By the definition of their long-range periodicity and symmetry, crystal structures can be alternatively understood as the stacking of a repeating crystal plane (a layer of atoms). The visualization of stacking planes is particularly important to differentiate fcc and hcp crystals. Both structures are made with a plane of the highest compacting order possible, i.e., the compact plane. The difference in the stacking of this repeating plane is what defines a fcc or hcp structure. Figure 3.3 demonstrates the stacking order ABABAB for hcp, and ABCABC for fcc, where the planes are defined as A, B and C, those being the different positions/sites between atoms of the adjacent planes which one can be positioned [23–25].

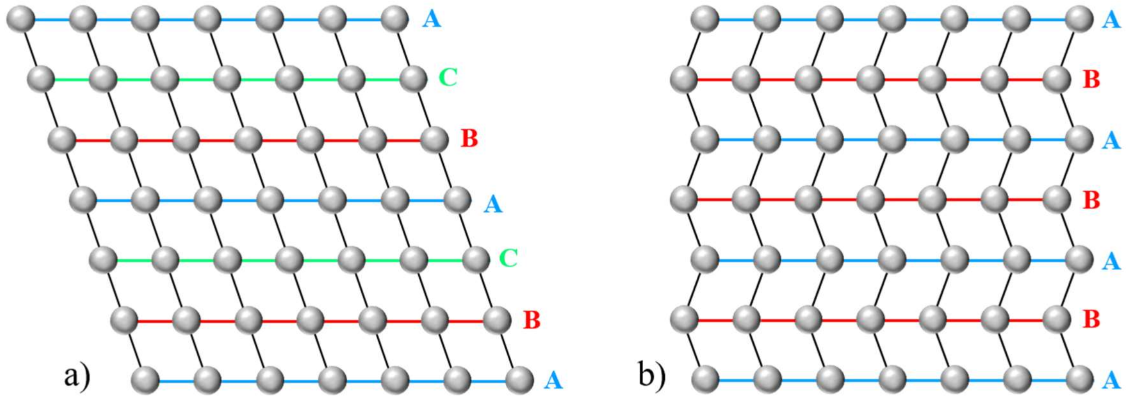

Figure 3.3. Illustrations of the stacking sequences in the (a) fcc and (b) hcp structures. The color-coding refers to the position occupied by each layer.

Stacking faults (SFs) are planar defects formed by the dissociation of a single dislocation into two partial dislocations. This happens when it is energetically favorable to reduce the elastic energy of a dislocation (with a larger burgers vector) into two (or more) imperfect dislocation withs smaller burgers vectors, even if it creates a new surface. In fcc phases, the most common SFs develop in the {111} planes (which are the compact ones). When the partial dislocations have a burger's vector of $^1/_6$<112> they are called Shockley partials, and their motion explains TWIP and TRIP effects [23–25]. Figure 3.4 demonstrates how the dissociation of a full dislocation in two Shockley partials, that repelled themselves into an extended dislocation, can alter the stacking sequence locally [23].

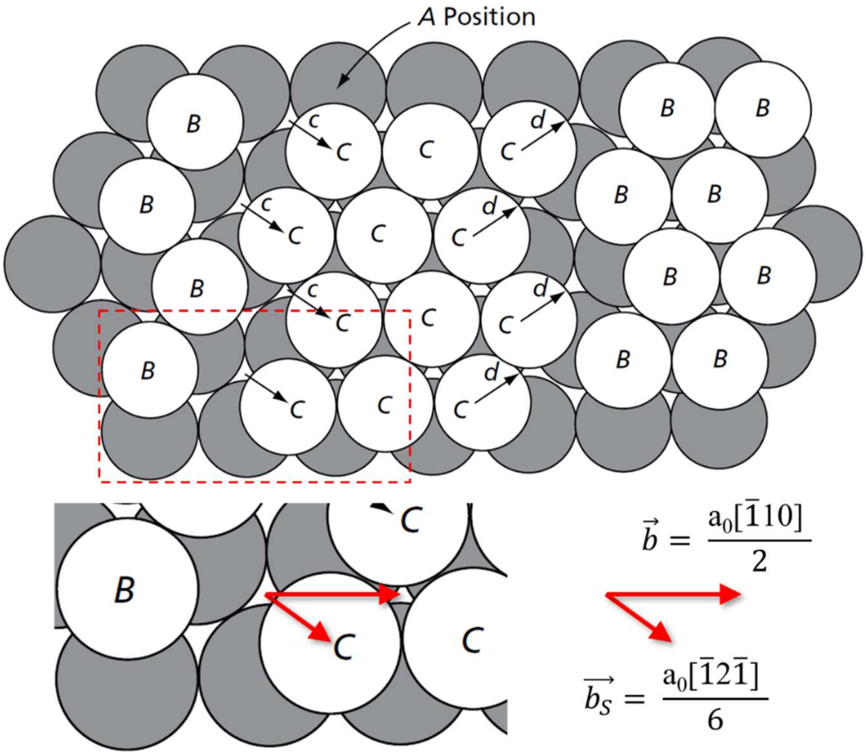

Figure 3.4. Representation of an extended dislocation. Atoms are denoted in relation to their position in the stacking sequence. The gray circles represent the atoms in the A layer, which is below the plane emphasized on the figure. Each of the regions between the "B" and "C" atoms are Shockley partials, as indicated by the black arrows analogous to $^1/_6$<112> burger's vectors. The total dislocation's (b) and Shockley partial dislocation's (b_S) burger's vectors are portrayed in an enlarged section of the top image. Adapted from [23].

The size of the stacking fault's surface, and its stability, depends on the SFE, which is the energy associated with this defect. Low SFEs will favor the stacking fault formation and their increase in size. Conversely, higher SFEs will cause the faults to be shorter or to not form at all. Chemical composition highly affects the SFE and, logically, this is very relevant for MPEAs. Grain size, temperature and short range order (SRO), are other parameters that also influence this property [10,23–25]. Figure 3.5 portrays the intrinsic and extrinsic stacking faults. The atomic layers represented in Figure 3.5 are {111} planes, just as the ones in Figure 3.4 (although those were normal to the image plane, and now the layers are perpendicular).

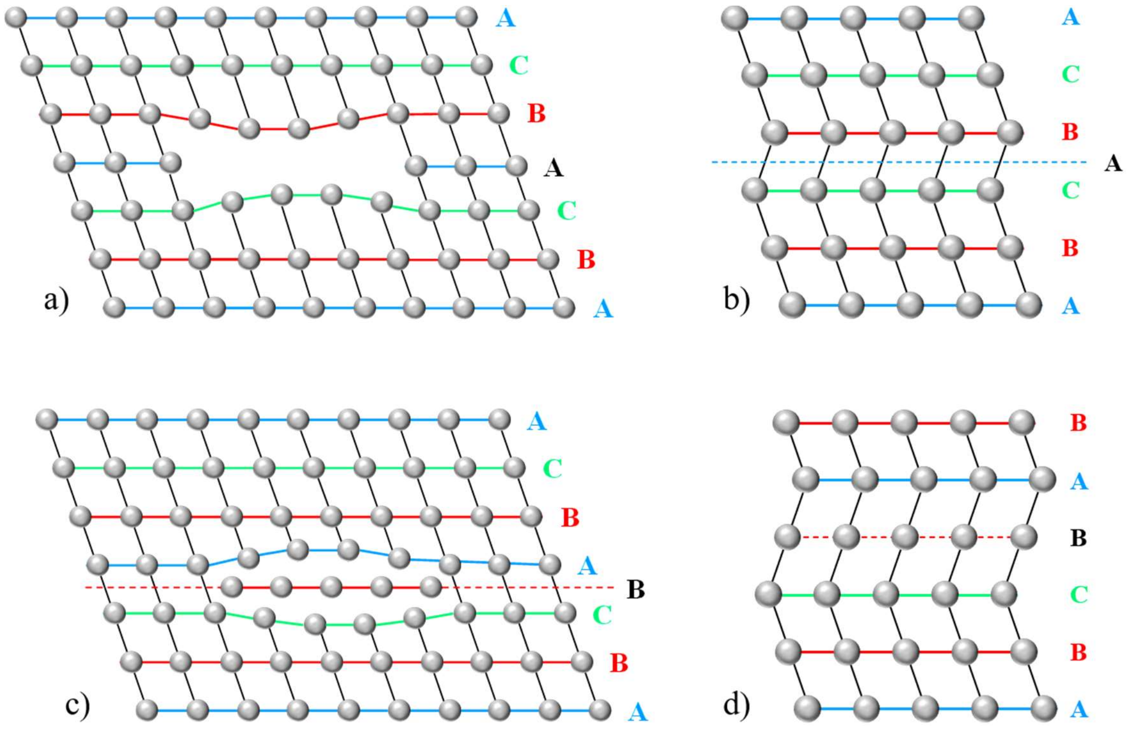

Figure 3.5. Illustrations of an (a-b) intrinsic and (c-d) extrinsic stacking faults in a fcc crystal structure. Each type of stacking fault is represented in two manners. On (a,c) images, they are fully contained within a dislocation ring and can occur, for example, by the formation or collapsing of vacancies. Intrinsic and extrinsic stacking faults can also form during deformation by the motion of a single Shockley partial dislocation (for the intrinsic) or a pair, but in parallel planes (for the extrinsic). If they are formed as the latter, the faults would look like what is shown in the (b,d) images and might cross the entire grain. The color-coding refers to the position occupied by each layer. Dashed lines and black font indicate a fault in the stacking sequence.

From Figure 3.5 it is possible to see that, while an intrinsic SF is characterized by the absence of a layer (type A, in the figure) in the stacking sequence, an extrinsic is defined by an extra one (an extra type B layer, in the figure's example). In Figure 3.5(b), because of the intrinsic fault a sequence of -BAB-, rather than -CAB-, is formed. Therefore, it means that, in this region, the crystal can be thought as a single layer of hcp structure. Subsequential SFs can form between each other and the hcp region will become larger

[10,25]. Alternatively, if these subsequential SFs form directly next to each other, as to produce a multi-layer fault, the local configuration will be that of a twin. Figure 3.6 illustrates both these situations. The image shows the motion of Shockley partial dislocations on {111} planes with the subsequential formation of stacking faults.

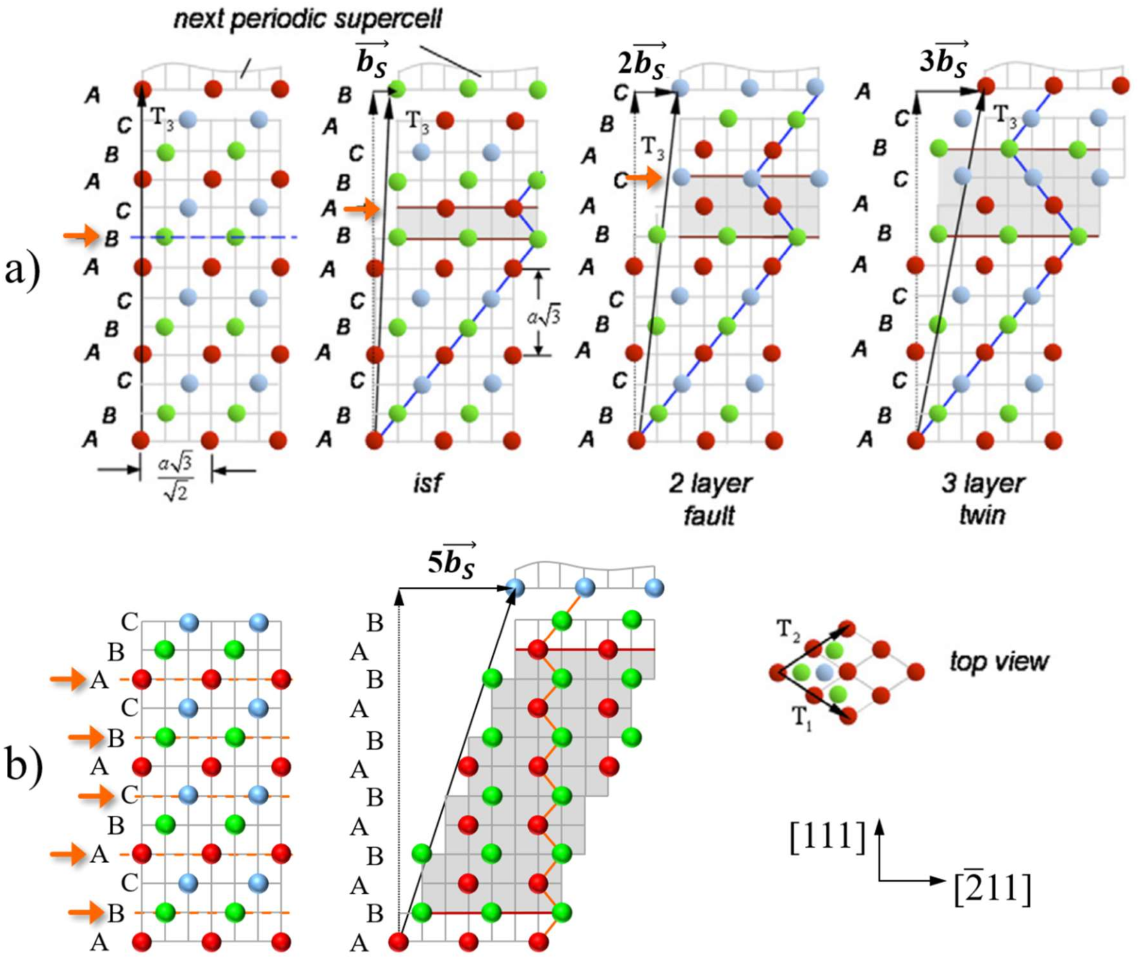

Figure 3.6. For {110} crystal plane view: a fcc supercell has its stacking sequence and structure altered by the motion of Shockley partial dislocations (orange arrows). In (a), first, the passage of a single partial produces an intrinsic stacking fault (isf). Second, another partial dislocation passes through, now in a parallel plane directly above the first. This forms a 2-layer fault which is an extrinsic stacking fault (esf), as it is equivalent to an "A" layer being introduced between the B and C. Subsequently, the passage of the third partial, forming the 3-layer fault, which is now a twin, completes the mirrored stacking sequence (i.e., BCA/B/AC/B/CA, with the "B" atoms characterizing the limits of the twin). The motion of subsequential (and directly above) partial dislocations would continue to increase the twin's size. Alternating partials (b) will change the crystal structure forming a hcp stacking sequence, rather than a twin. The amount and direction

the crystal structure is sheared is given in terms of b_S (equal to $^{a_0}/_{6}$<112>). The translation vector T_3 shows the equivalence to the original stacking sequence. Adapted from [26].

As mentioned before for a fcc material, the lower the SFE, the larger the separation between the Shockley partials. In accordance to this, the harder it becomes for dislocations to cross-slip and climb, consequently, for the structure to be deformed by dislocation glide. With this mechanism hindered, TWIP and TRIP become energetically more viable [10,27]. Bertoli et al. [27], collected data from various publications on fcc Cr-Co-Ni alloys and proposed an empirical equation, with a R^2 of 98 %, to determine the SFE based on Cr and Co atomic fractions (X_{Cr} and X_{Co}, respectively). Their equation (3.2), does not consider the effects of SRO and local atomic configuration, and was constructed with data obtained at room temperature with relatively large grain sizes [27].

$$SFE\left[\frac{mJ}{m^2}\right] = 248 - 835 \cdot X_{Cr} - 323 \cdot X_{Co} + 682 \cdot X_{Cr}^2 - 39 \cdot X_{Co}^2 + 777 \cdot X_{Cr} \cdot X_{Co} \quad (3.2)$$

Figure 3.7(a) compares SFE values calculated by equation 3.2 with thresholds for the predominance of different deformation values, as proposed for steels.

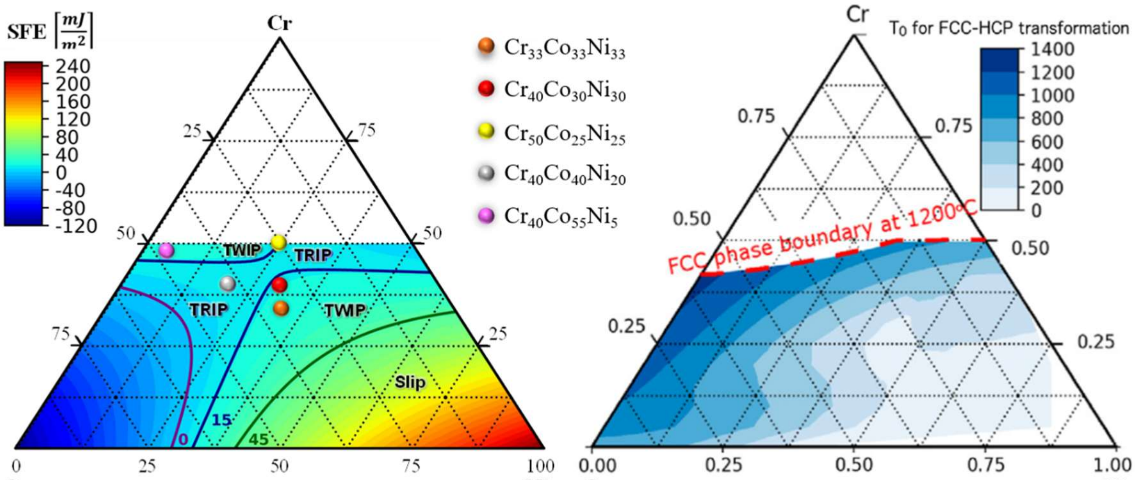

(a) (b)

Figure 3.7. Cr-Co-Ni ternary plots overlaid with (a) the SFE values calculated by equation 3.2, and (b) T_0 values. In (a), the SFE limits proposed to steels for TRIP-predominance (< 15 mJ/m^2), for TWIP-predominance (15 < SFE < 45 mJ/m^2) and deformation by slip (> 45 mJ/m^2), are displayed. Adapted from [27]. (b) is adapted from [10].

The figure shows that the base alloy from this work, $Cr_{40}Co_{30}Ni_{30}$, is predicted to have a TWIP-predominant behavior (a SFE of 16 mJ/m^2), considering SFE at room temperature (cold work) and for relatively large grain sizes. Alternatively, according to Figure 3.7(b), TRIP is expected to occur at room temperature deformations, since T_0 is the temperature where the hcp and fcc phases are equally stable. It means that in T_0 their Gibbs free energies (G) are equal ($G_{fcc} = G_{hcp}$). Below T_0 the driving force for the partitionless transformation of fcc into hcp increases, favoring the TRIP effect [10,27]. These diagrams are not free from errors, and can vary due to many factors, by the method employed and due to accuracy. Even more, SFE is not a definite parameter for determining deformation mechanisms [28,29]. Although, the values on both plots should not be utilized as guidelines to determine which deformation mechanisms will occur, their trend is interesting. That is, increasing Cr and Co contents favors the occurrence of TWIP and TRIP mechanisms rather than just dislocation glide [10,27].

3.3.2 TWIP and TRIP

Deformation twinning (TWIP) will occur when the critical resolved shear stress for twin formation is reached during deformation. In most fcc metals this stress is not achieved before fracture occurs. The reason why SFE is a defining factor in the plastic deformation modes is relative to the twin boundary surface energy, which is intimately connected with the surface energy of stacking faults. A great fraction of the energy needed to create a twin is relative to its boundaries. The lower the SFE, the lower these energies will be, and the lower the critical resolved shear stress to nucleate twins [23].

Both twinning (Figure 3.6a) and the hcp formation by stacking faults (Figures 3.5 and 3.6b) promote the realignment of the crystal structure. Except that, for twinning, the structure and stacking sequence remains the same, albeit with a mirrored orientation. The twinning planes demarks this mirrored symmetry [23]. A twin is represented in Figure 3.8.

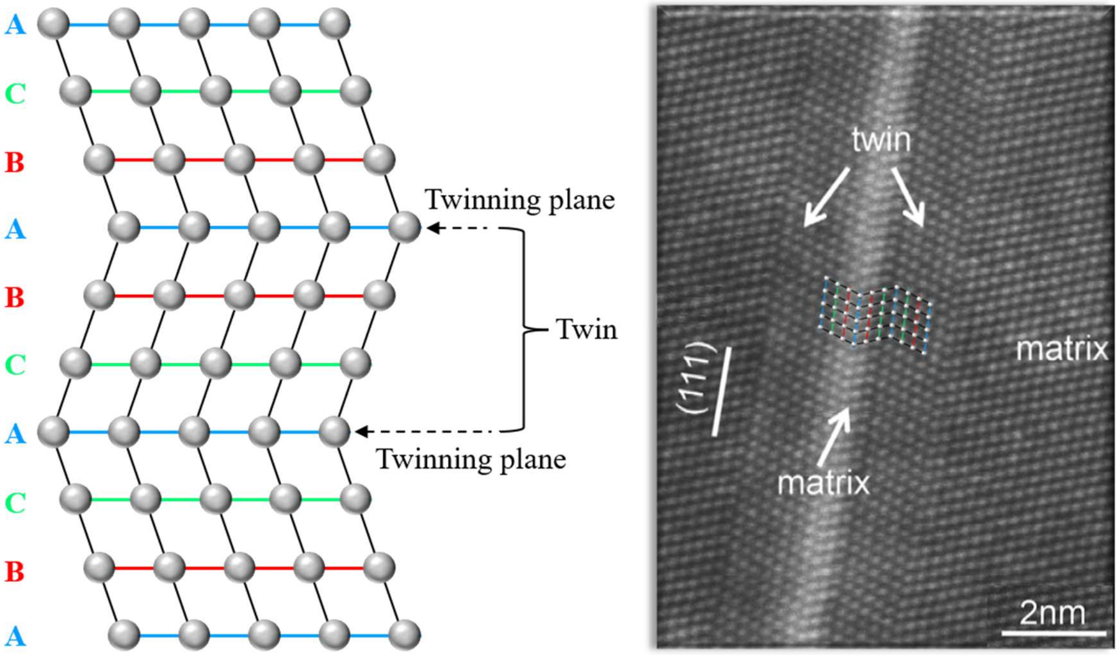

Figure 3.8. In the left, an illustration of a twin in a fcc matrix, as indicated by the stacking sequence. At the right side, an example of a real twin, made with angular dark field (ADF) imaging mode in a scanning electron transmission microscopy (STEM) along a <110> zone axis, for a CrCoNi alloy tensile tested at room temperature until 25 % strain. In the ADF-STEM image, two nanotwins are visible, and the drawn twin structure of the left was inserted to illustrate the atomic arrangement in a didactic manner. Right image adapted from [30].

Coherent twin boundaries are parallel to the twinning planes, whereas the incoherent ones are not, and dislocations will exist to maintain cohesion with the parent lattice. It appears that these interfaces can behave in a similar fashion to grain boundaries (GBs) and, as such, will have an influence (however small) in reducing the average grain size [23].

Just as for slip, there is an amount of deformation associated with twinning, although its contribution to the total plastic strain tends to be much smaller. This is correlated to the fact that the shear strain produced by twinning only distorts the lattice by less than an interatomic spacing, differently than by slip. Also, in contrast to dislocation glide, twinning in fcc metals is shown to decrease the work hardening rate. This is true for single crystals' early stages of twinning in a deformation initially dominated by slip, in which the increment of stress needed is not as significant as the quantity of strain generated by the twin. Since this mechanism occurs in the same {111} family of planes that for slip, twinning will happen in a primary plane with the orientation relative to the highest resolved shear stress. In other words, the stress responsible for dislocations' movement will also promote twinning (when the critical value is reached) without the need for additional increments. Additionally, this will proceed without a significant amount of work hardening due to the twins affecting dislocation movement, since the slip plane and twin plane are the same. But, eventually, with the increase in stress, twinning starts happening in intersecting planes to the primary, and the work hardening rate rises [23].

The hcp phase, product of TRIP in CrCoNi appears to be mostly nanostructured, as nanoscale laths for example. The same seems to be true for twinning [10,20,30]. For the equiatomic alloy, it has been suggested that the hcp could possibly revert to fcc with additional strains, due to its formation nature. Further study is needed to prove this reversibility and to correlate with SFE i.e., for alloys with more TRIP-predominant compositions [10,22,31]. Miao et al. [30] showed, for the CrCoNi equiatomic alloy, that the hcp phase laths can form in a "interspersed" configuration with the nanotwins and, as such, this type of arrangement was denominated as nanotwin-hcp lamellae. In accordance with the identification of these type of structures, they observed, for room and cryogenic temperatures, that hcp seem to form preferably in conjunction with nanotwins [30]. This can be seen in Figure 3.9. The evolution of the substructure observed by the mentioned study is coherent with what is reported in the literature for Cr-Co-Ni fcc alloys and other similar MPEAs under quasi-static tensile testing [22,30,32–40].

The hcp phase and twins (and the stacking faults) can be identified and differentiated between each other through some analysis techniques. For ADF or high angle annular dark field (HAADF) images, and other high-resolution electron transmission microscopies, filtered fast Fourier transformations (filtered FFT) and center of symmetry (COS) maps are useful image processing techniques. The former, highlights the individual atoms and detect deviations in symmetry, therefore aiding in the stacking sequence (consequently, SFs, twins and hcp, as well as the matrix) visual identification. Figure 3.9 has examples of COS maps and filtered FFT images for a CrCoNi alloy STEM image.

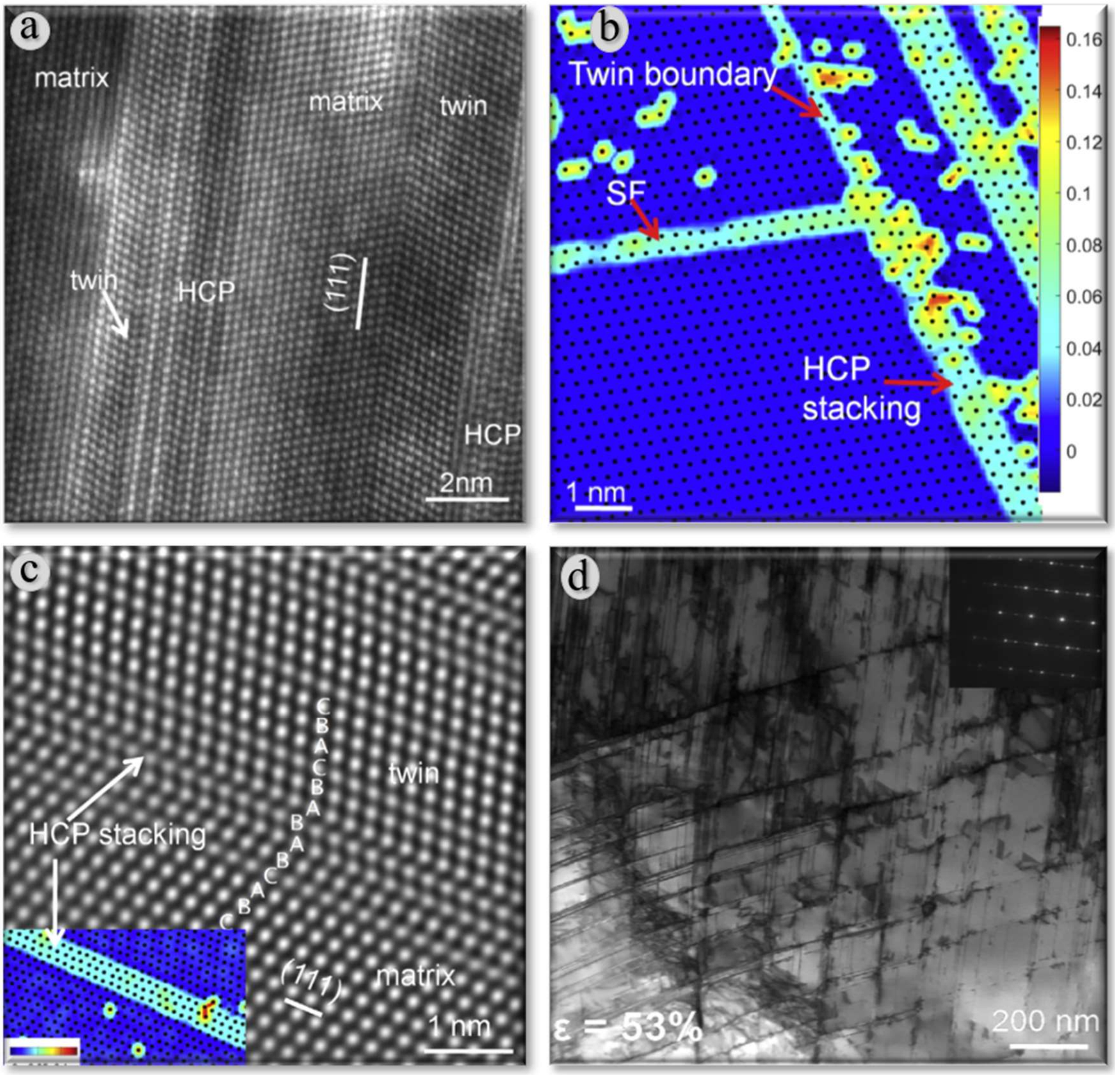

Figure 3.9. STEM images for an CrCoNi equiatomic alloy, from Miao et al. [30] work. Figure (a) is an ADF image, taken along a <110> zone axis, for the sample tensile tested at room temperature until 25 % true strain. In (a) the nanotwin-hcp lamellae structure is clearly visible. The other figures are from samples tested at liquid nitrogen temperature, until 25 % (b) and 53 % (c-d) true strain. Figure (b) is a COS map of an ADF-STEM image, that shows an interaction between a SF and a twin boundary. The regions that diverge from the stacking symmetry are clearly visible due to the color coding. Figure (c) is an ADF-STEM FFT filtered image, it shows the nanotwin-hcp lamellae and highlights the stacking sequence. A COS map is also added to help visualize the hcp stacking. Figure (d) is a bright field diffraction contrast imaging STEM image along the <101> zone, with a SAED pattern inserted. Twinning and hcp spots can be clearly seen. Adapted from [30].

An essential technique to all types of transmission electron microscopy (TEM) analyses, is electron diffraction. In Figure 3.9(d), a selected area electron diffraction (SAED) pattern was utilized to identify each constituent. Crystallographic understanding, mainly to identify lattice planes and directions, is needed since all the mentioned microstructure elements have a highly directional character. X-ray diffraction (XRD), as well as other crystallographic identification techniques can also be used. Although, the lack of resolution can render some of these fruitless depending on the scenario, since the microstructure (or substructure) features often occur in small quantities and nanometric sizes.

3.4 Strengthening Mechanisms

One of the objectives of this work is to study the effects of carbon-doping (CD) to the Cr-Co-Ni system, more specifically to the $Cr_{40}Co_{30}Ni_{30}$ alloy. As will be seen in section 4 of this text, this element, in the compositions and processing conditions employed, is expected to result in precipitation and/or stay in solid solution in the fcc matrix. According to CALPHAD calculations (section 4.3), when precipitated, C will appear mainly as Cr-rich carbides. Carbon should occupy interstitials sites when in solid solution, due to the size of its atomic radius (approximately 77 pm in the diamond lattice) when compared to those of Cr (128 pm), Co (125 pm) and Ni (124 pm) [23,41].

Due to a decrease of elastic energy, solutes tend to interact with dislocations and grain boundaries. For plastic deformation to be possible, i.e., to overcome this interaction, increments of stress are needed. Cr has a significant atomic volume mismatch (around 11~13 %) in relation to Co and Ni, which are both more similar in size (less than 2 %). It also has the highest shear module out of the elements from the Cantor alloy. That being said, CrCoNi was shown to have a high solid solution strengthening effect when compared to other alloys from Cantor sub-systems [10].

3.4.1 Carbon-Doping: Solid Solution Strengthening and Precipitation hardening

Similar to solutes, precipitates will also interact with microstructural defects. Since they are static obstacles that need to be surpassed for the motion of dislocations and GB to be possible, the stress increment necessary for deformation is even higher in their presence. The two main means of dislocation bypassing precipitates are the cutting and Orowan bowing mechanisms, demonstrated in Figures 3.10a-b [23].

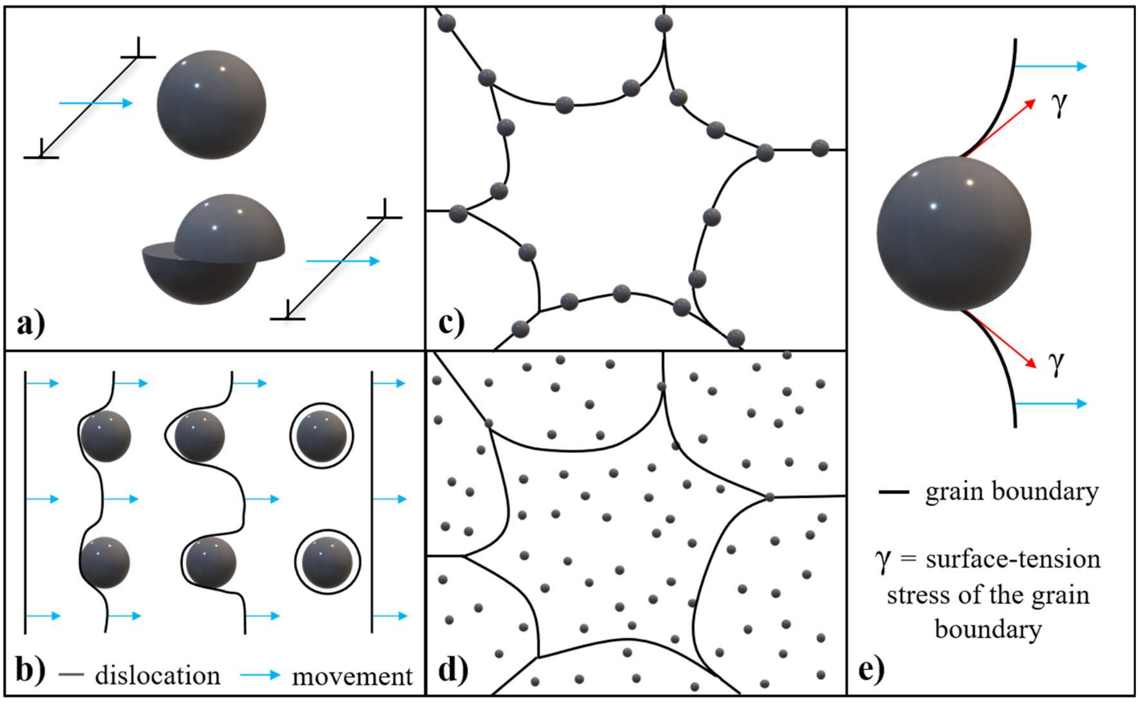

Figure 3.10. Illustrations of the described interactions second phase particles have in metallic structures. Figures (a) and (b) represent, respectively, the cutting and Orowan bowing mechanisms for edge dislocations. A heterogeneous distribution of precipitates in the grain boundaries, and a homogenous distribution inside the grains matrix, are shown in Figures (c) and (d) respectively. Figure (e) represents the Smith-Zener drag phenomenon. All the blue arrows denote movement.

The precipitates will generally be formed favorably in grain boundaries and other interfaces since heterogeneous nucleation, as illustrated by Figure 3.10c, is energetically advantageous. A homogeneous formation (which Figure 3.10d portrays), which occurs in typical precipitation hardened alloys, can be induced when less atomic mobility and higher driving forces are present (at lower temperatures, for example). Starting with a solution treatment, followed by quenching (to form an excess of vacancies and generate a supersaturated solid solution) and, finally, with an ageing step to obtain intermediate precipitates wielding superior hardness, when compared to other precipitate structures (totally incoherent equilibrium particles, for example) [23]. In further sections of this work a more in depth discussion of the expected precipitations scenarios for the studied alloys is found.

In a heterogenous distribution, precipitates will not contribute as much for strengthening, as the interaction between them and the dislocations outside the GB will be minimal. Nevertheless, they still are significant in their interaction with the GB, affecting grain sizes, coarsening kinetics and shapes through a process known as Smith-Zener drag/pinning. This is true especially during recrystallization, but also whenever there is GB movement, such as in plastic deformation [23,42]. The Smith-Zener drag is illustrated on Figure 3.10e, in which a grain boundary in motion is pinned by a particle with a radius of R. The maximum drag force exerted between the GB and the particle, if the latter is incoherent with the matrix, is given by equation 3.3 [42]:

$$F_{max} = \pi \cdot R \cdot \gamma \tag{3.3}$$

Where γ is the surface-tension of the GB (or other type of boundary depending on the scenario). Low angle boundaries will have lower values of γ than those with high angle, because the boundary energies of the former ones are lower. Alternatively, for a coherent particle, the force will be equal to [42]:

$$F_{max} = 2\pi \cdot R \cdot \gamma \tag{3.4}$$

The reason why the maximum drag force in a coherent particle is double of that for an incoherent, of the same size and shape, is because of the loss of coherence when a high angle GB overcomes the particle. For this change, the boundary will need to offer additional energy, since the incoherent interface produced is more energetic than the previous coherent one. Alternatively, other effects can happen to less stable (smaller, for instance) particles, such as its dissolution (which can be followed by a re-precipitation), a reorientation of the particle to maintain coherence or even it being cut by the GB [42].

The boundary will overcome the restraining effect when the force it exerts in the particle is higher than F_{max}. This additional requirement of energy will, in the annealing for example, affect the migration of GBs, thereby hindering the recrystallization process as well as the grain growth. The recrystallization temperatures will, then, become higher. Particle pinning will also greatly affect grain sizes, leading to overall smaller average sizes, as well as limiting the final grain sizes (i.e., limiting grain growth) considerably. As discussed before, solutes have, themselves, influence in GB (and consequently, in GB migration), and will contribute, as well, in the rise of recrystallization temperatures and hindering of grain growth. Precipitates and solutes also affect other phenomena such as recovery and plastic deformation, as they interact with dislocations. Both these effects have influence in the stored energy of deformation and, consequently, on recrystallization [23,42].

Having considered the effect of a single second-phase particle on coherent and incoherent boundaries, it is now interesting to discuss the modeling for the full precipitation. As such, for a random distribution, the number of precipitates per unit volume (N_v) is given by [42]:

$$N_v = \frac{3 \cdot f_v}{4\pi \cdot r^3} \tag{3.5}$$

Where fv is the particles' volume fraction and r the average particle radius. These two factors are fundamental in basically all second-phase strengthening theory. The number of precipitates per unit of surface area (Ns) intersecting a planar boundary can be estimated as [42]:

$$N_s = 2 \cdot r \cdot N_v = \frac{3 \cdot f_v}{2\pi \cdot r^2} \tag{3.6}$$

The drag generated by these particles will result in a pinning pressure per unit of area and is known as the Smith-Zener pinning pressure (P_{SZ}). It relates to N_s and to the area fraction of the particles (f_s) such as [42]:

$$P_{SZ} = N_s \cdot f_s \tag{3.7}$$

Where f_s can be determined in term of N_s, f_v or N_v as:

$$f_s = N_s \cdot \pi r^2 = \frac{3 \cdot f_v \cdot r}{2} = N_v \cdot 2\pi \cdot r^4 \tag{3.8}$$

From equations (3.8), (3.3) and (3.7), we have that the Smith-Zenner pinning pressure for particles on unit area of a planar boundary will be [42]:

$$P_{SZ} = \frac{3 \cdot f_v \cdot \gamma}{2 \cdot r} \tag{3.9}$$

The relationship proposed in equation 3.9 is an approximation and was made with different ideal considerations (the planar morphology is an example). However, more complex simulations generally do not differ much from the correlation obtained and confirm the Smith-Zener relationship [42]. A separate study with finite element calculations and considering precipitate-precipitate interactions obtained a value for P_{SZ} twice the one stablished by equation 3.9 [42]:

$$P_{SZ} = \frac{3 \cdot f_v \cdot \gamma}{r} \tag{3.10}$$

For a mean grain boundary intercept length l (which is similar to the grain size, d), the planar boundary consideration is only adequate if: l >> interparticle spacing (l_p). Simplifying the grains to squares, it is possible to consider the possible scenarios for different particle distributions as shown in Figure 3.11 [42].

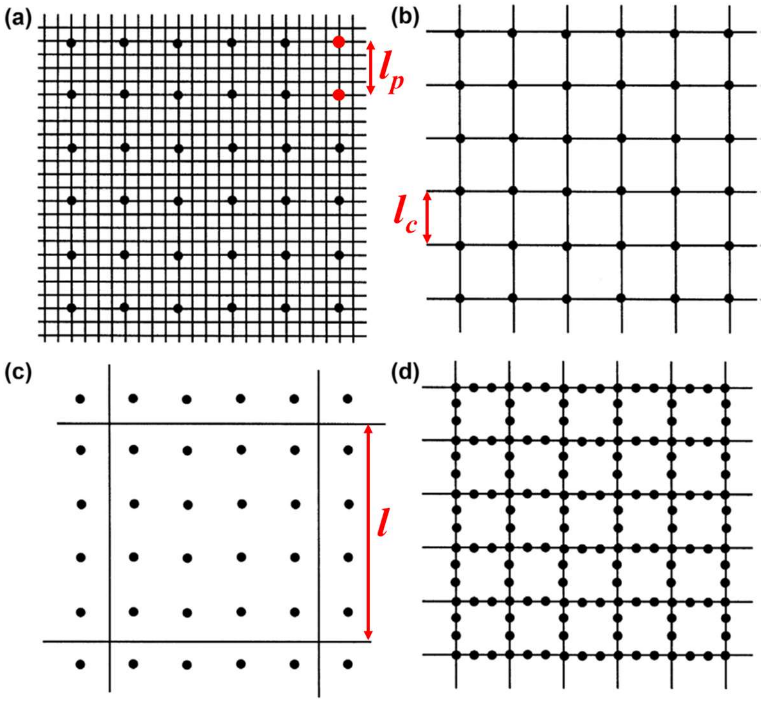

Figure 3.11. Simplified representation of particles and boundaries distributions. (a) $l << l_p$. (b) $l = l_p$. For $l >> l_p$, both (c) homogeneous and (d) heterogeneous distributions are considered. Adapted from [42].

The number of precipitates per unit area of boundaries (N_b) can be estimated as [42]:

$$N_b = \frac{N_v \cdot l}{3} \tag{3.11}$$

For distributions such as those seen in Figures 3.11a-b, N_b will be [42]:

$$N_b = \frac{N_v \cdot l}{3} = \frac{f_v \cdot l}{4\pi \cdot r^3} \tag{3.12}$$

As such, the Smith-Zenner pinning pressure for an incoherent precipitate with a near spherical morphology can be calculated as [42]:

$$P_{SZ}^{IS}(l \leq l_p) = \frac{1.82 \cdot f_v \cdot l \cdot \gamma}{4 \cdot r^2} \tag{3.13}$$

Equation 3.13 will be valid for $l \leq l_p$. The value for which l is the same size as the interparticle spacing (Figure 3.11b) is called lc, and is given by [42]:

$$l_c = l_p = N_v^{-1/3} = \left(\frac{4\pi \cdot r^3}{3 \cdot f_v}\right)^{1/3} \tag{3.14}$$

For grain sizes in this range, the Smith-Zenner pinning pressure will be the highest possible. Substituting (3.14) in equation (3.13) we have that [42]:

$$P_{SZ}^{IS}\,(MAX) = \frac{2.2 \cdot {f_v}^{2/3} \cdot \gamma}{r} \tag{3.15}$$

For sizes larger than l_c, i.e., if $l > l_p$ then the pinning pressure will follow a different relationship, given by [42]:

$$P_{SZ}^{IS}\,(l > l_p) = \pi r \cdot \gamma \cdot \left[\frac{1.82}{l^2} + \left(1 - \frac{1}{N_v \cdot l^3}\right) \cdot 2 \cdot N_v \cdot r\right] \tag{3.16}$$

Eventually, as grain sizes get larger, equation 3.16 will become equal to equation 3.10. Figure 3.12 shows the usual aspect of the graphs for the Smith-Zener pinning pressure as a function of mean intercept length of the boundaries.

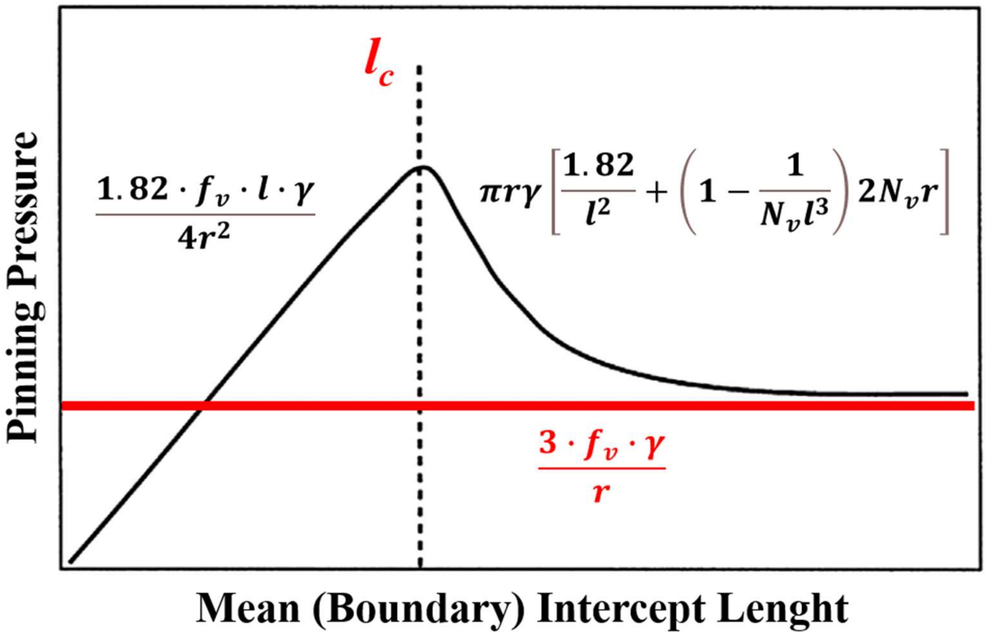

Figure 3.12. Effect of intercept length on the pinning pressure for a specific distribution of precipitates. Adapted from [42].

Not always the second-phase particles will be randomly distributed. As such, when there is a specific concentration of particles, relationships different from the discussed above will be best suited. For precipitates banded into planar arrays of particles we have the following equation [42]:

$$P_{SZB} = \frac{P_{SZ} \cdot L}{h_B} \tag{3.17}$$

Where L is the spacing between two neighboring bands of particles, and h_B is the average thickness of these bands. Equation 3.17 is only for boundaries that are parallel to the bands. For perpendicular boundaries, the pinning pressure will generally be P_{SZ} in the contact regions, while zero in between since it does not experience pinning [42]. If the particles are neither banded nor in a random distribution, they can, for example, be located mainly on grain boundaries (just like the distribution shown in Figure 3.11d). As such, when there is a heterogeneous dispersion, the pinning pressure can be estimated as [42]:

$$P_{SZH} = f_s N_b = \frac{f_v \cdot l \cdot \gamma}{4 \cdot r^2} = \frac{P_{SZ}^{IS}(l \leq l_p)}{1.82} \tag{3.18}$$

A random dispersed second-phase particles distribution can hinder the nucleation of recrystallized grains during annealing of a deformed sample. However, for large enough particles distributed in insufficient quantity, the drag effect will not prevent nucleation and growth and recrystallization can be accelerated. This is because the precipitates will serve as substrate for the nucleation of new undeformed grains. The mentioned phenomenon is known as particle-stimulated nucleation (PSN) [42]. A general rule of thumb is that retardation occurs for dispersions with f_v^n/r ($1/3 < n < 1$) greater than approximately 0.2 μm^{-1}. This critical value will be greater the higher the amount of stored plastic deformation. The explanation is that the driving force for recrystallization grows with strain (which is not the case for pinning pressure) [42]. Humphreys et al. [42] concluded that, regarding recrystallization, the Smith-Zener drag effect is more influential in the nucleation of new grains rather than on the growth stage [42].

As mentioned before, for a totally recrystallized sample, the grain growth will be hindered by the presence of a second-phase particle dispersion. When the Smith-Zener pining pressure is higher or equal to the driving pressure for grain growth (P_{GG}), then the latter will be interrupted. For $P_{GG} = P_{SZ}$ and a random distribution of particles, using equation 3.10 we have [42]:

$$\frac{\alpha \cdot \gamma}{R_c} = \frac{3 \cdot f_v \cdot \gamma}{r} \tag{3.19}$$

Where α is a correlation parameter (with the best reported range between $0.25 < \alpha < 0.5$), and R_c is the mean curvature radius. If the mean grain size is considered as twice the size of R_c, than the limiting grain size during grain growth can be estimated as [42]:

$$D_L = \frac{2 \cdot \alpha \cdot r}{3 \cdot f_v} \tag{3.20}$$

Alternatively, considering the P_{SZ} of equation 3.9, D_L would be double that of equation 3.20. If nearly all the particles are heterogeneously and randomly distributed in the grain boundaries, applying $P_{GG} = P_{SZH}$ will result in a limiting grain size of [42]:

$$D_{LH} = r \cdot \sqrt{\frac{8 \cdot \alpha}{f_v}} \tag{3.21}$$

Finally, for particles arranged in bands, the limiting grain size can be calculated by determining the value for which PGG = PSZB:

$$D_L = \frac{4 \cdot \alpha \cdot r}{3 \cdot f_v} \cdot \frac{h_B}{L} \tag{3.22}$$

Many other considerations can be made regarding second-phase particles and drag effects. However, this is out of the scope of this dissertation, and reading other references is suggested. Nevertheless, some additional interesting remarks from Humphreys et. al. book are [42]:

- If grain growth is suppressed, the alloy can become more susceptible to abnormal grain growth (secondary recrystallization) at high annealing temperatures;
- The pinning pressure will also affect subgrain sizes;
- Particle distribution can affect recrystallization textures.

3.4.2 Grain Refinement Strengthening

Grain size is directly correlated to mechanical properties due to the pile-up of dislocations mechanism. The smaller the grain size, the greater the increments to mechanical properties. Furthermore, there seems to be a regular relationship between these factors. This dependency can be mathematically stablished by an empirical relation, the Hall-Petch (HP) relation, just as equation 3.23 indicates [23].

$$H = H_0 + k_H d^{-1/2} \tag{3.23}$$

Where H stands for hardness, H_0 and k_H are specific constants of the material and d is the average grain size. The Hall-Petch relation also applies to some properties other than hardness, like yield-stress, flow-stress and the ultimate tensile strength. The correlation with grain size is the same (inversed square root), but the constants are relative to each property. The HP relation does not hold well for very fine nanocrystalline size distributions (in the order of tenths, or even hundreds, of nm). That is because dislocation pile-up ceases to occur or becomes less relevant, and other mechanisms take place. In this scale it is believed that GB migration and other GB-mediated mechanisms are predominant for plastic deformation [23,43,44].

The Hall-Petch relation for the CrCoNi equiatomic alloy has already been studied by multiple authors. Regarding yield strength (σ_y) as a function of inverse square root of grain size, Yin et al. [45] gathered data found in the literature and plotted an aggregated curve that can be seen in Figure 3.11. In the same plot, HP curves for other multi-principal alloys are also portrayed. Between all materials, the CrCoNi TRIP dominated sub-system alloy, $Cr_{40}Co_{40}Ni_{20}$, obtained by Bertoli et al. [27], displayed the highest friction stress (σ_0) and k (HP slope) coefficients.

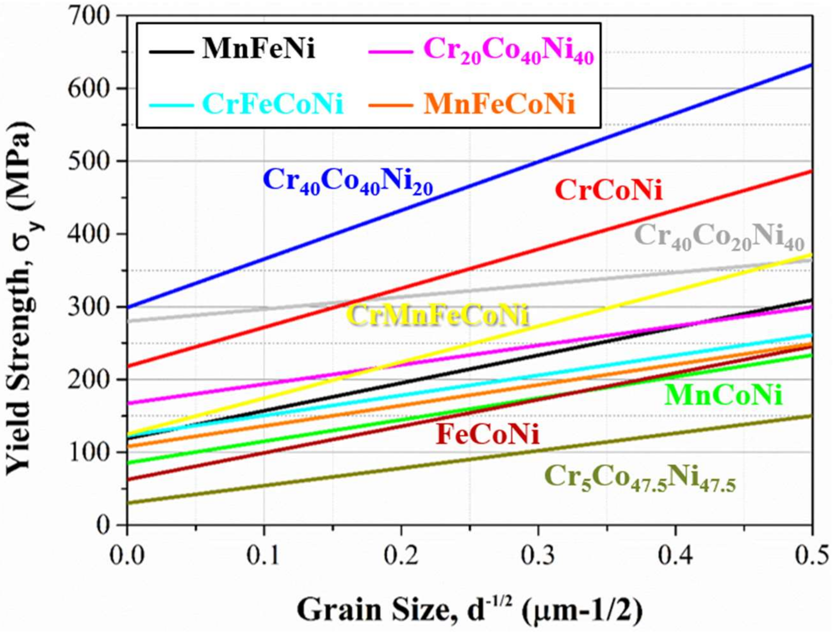

Figure 3.11. Hall-Petch relationships, on yield strength as a function of the inverse square root of average grain size, for various annealed MPEAs. Tensile-testing at room-temperature. The CrCoNi curve was obtained from [45], the $Cr_{40}Co_{40}Ni_{40}$ from [27], and the others from [46].

Hardness HP relationship curves, plotted for various MPEAs as well, can be seen in Figure 3.12. And, just as for the yield strength results, the CrCoNi alloy stands out for its high HP coefficients. The high slope values on both figures, which are rightfully depicted on Table 3.1 (along with the other coefficients used), justify the interest in studying grain-refinement for the CrCoNi and its sub-system of alloys. It can be noted that as Cr content decreases there is a tendency to decrease the friction stress. A similar correlation (with the current available data) cannot be made between Cr and the HP slopes (k). However, comparing $Cr_{40}Co_{40}Ni_{20}$ and $Cr_{40}Co_{20}Ni_{40}$, the σ_0 is very close in value whereas the alloy with higher Co content displayed a k coefficient four times higher. Alternatively, higher contents of Ni seem to result in lower values of both HP coefficients. This may be due to a rise in the SFE. A $Cr_{40}Co_{30}Ni_{30}$ alloy studied by Puosso et al. [38] showed HP parameters very similar to those of the $Cr_{40}Co_{40}Ni_{20}$ alloy (table 3.1).

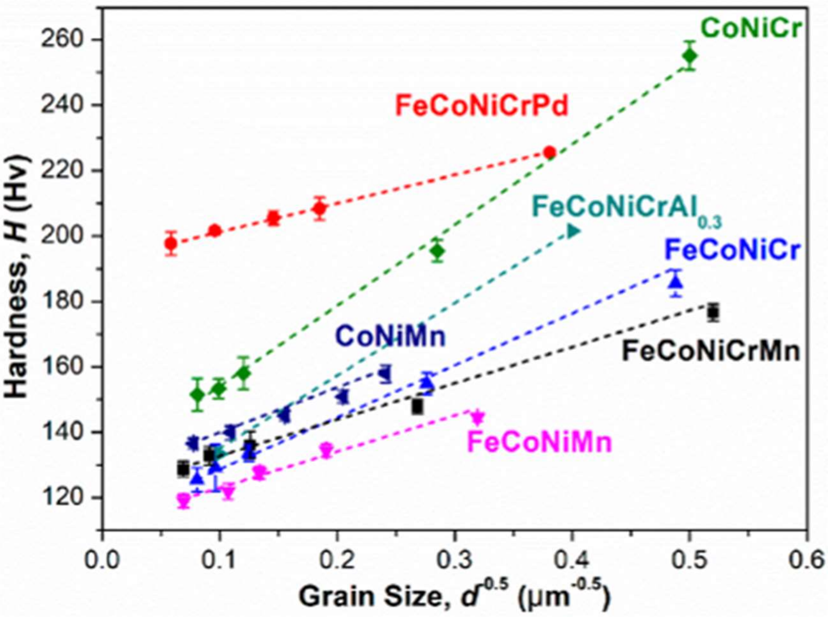

Figure 3.12. Hall-Petch relationships, on Hardness as a function of the inverse square root of average grain size, for various annealed MPEAs. Adapted from [19].

Table 3.1. Hall-Petch coefficients for the various MPEAs present on Figures 3.11 and 3.12

Alloys	**σ_0 (MPa)**	**k ($MPa\cdot\mu m^{-1/2}$)**	**H_0 (HV)**	**k_H ($HV\cdot\mu m^{-1/2}$)**	**Reference**
$Cr_{40}Co_{40}Ni_{20}$	299	667	-	-	[27]
$Cr_{40}Co_{30}Ni_{30}$	247	655	-	-	[38]
CrCoNi	218	537	129	249	[45], [19]
$Cr_{40}Co_{20}Ni_{40}$	280	168	-	-	[46]
$Cr_{20}Co_{40}Ni_{40}$	167	266	-	-	[46]
$Cr_5Co_{47.5}Ni_{47.5}$	30	240	-	-	[46]
CrMnFeCoNi	125	494	122	103	[46], [19]
CrFeCoNi	123	276	115	146	[46], [19]
MnFeCoNi	108	282	112	104	[46], [19]
MnCoNi	86	296	126	127	[46], [19]
FeCoNi	63	366	-	-	[46]
MnFeNi	119	381	-	-	[46]
CrFeCoNiPd	-	-	193	85	[19]
$Al_{0.3}CrFeCoNi$	-	-	111	227	[19]

3.4.3 TWIP and TRIP Effects on Strengthening Mechanisms

The increments in work hardening rate promoted by TWIP and TRIP will contribute positively to the mechanical properties of the material. The value of strain in which the uniform plastic deformation state ends, and necking begins, is dependent on the work hardening rate. Increasing the work hardening rate will reflect in an increasing work hardening exponent, and consequently on the maximum uniform strain, as stated by Considère's criterion. Hence, these plasticity phenomena benefit the ductility and toughness as a whole. Accordingly, it was proposed that the deformation twinning on the CrCoNi alloy will promote a "dynamic Hall-Petch effect" because of the interactions between dislocations in slip motion and the twin boundaries formed. This effect is correlated to improvements in ductility because it raises the work hardening rate [10,20,47]. As mentioned in section 3.3.2, twin boundaries can often act as GBs [23].

The critical resolved shear stress (CRSS) for twinning in CrCoNi seems to be comparable, if not higher, to Cantor and other sub-family alloys [10,21]. Nevertheless, the yield strength and work hardening rate also appear to be higher, enough so that nanotwins nucleate for smaller strains. All this contributes to improved mechanical performances [20,48]. Laplanche et al. [20] pointed out that temperature does not seem to have much effect on the CRSS. Therefore, twinning will tend to occur at lower strains the lower the temperature, since yield strength is shown to rise with the decrease of temperature in these alloys. The extended strain range of TWIP helps explain the great mechanical properties in cryogenic temperatures of the CrCoNi alloys [20,21]. Concurrently, TRIP was also reported to benefit from lower temperatures (starting at lower deformation stages) and to similarly improve these properties [10,21,30].

4 MATERIALS AND METHODS

The object of study for this work is the alloy $Cr_{40}Co_{30}Ni_{30}$ (at.%) with and without carbon-doping (i.e., addition of small quantities of carbon as an alloying element). Three compositions where intended: "pure" $Cr_{40}Co_{30}Ni_{30}$, which was called material "A". Material "C" consisted of $Cr_{40-x}Co_{30}Ni_{30}$ with 0.4 at.% of carbon. And finally, an intermediate composition range with an (intended) addition of 0.2 at.% of carbon (half of the quantity added for material C) called material "B" (it will be shown later that the real carbon composition achieved was of 0.1 at.%).

4.1 Alloy Selection

As mentioned before, the main objective of this study is to evaluate the effect of small additions of carbon on the average grain size distribution and, consequently, on the final mechanical properties of the $Cr_{40}Co_{30}Ni_{30}$ alloy. To better formulate this idea thermodynamic pseudo-binary diagrams were plotted utilizing the *Thermo-Calc^{TM}* software following the CALPHAD method. TCHEA5 was the chosen database, as all of the 6 possible binary and 4 ternary systems between Cr, Co, Ni and C were critically assessed. An isopleth ranging from the $Cr_{40}Co_{30}Ni_{30}$ to the $Cr_{39}Co_{30}Ni_{30}C_1$ compositions was calculated and is presented in Figure 4.1.

For the isopleth of Figure 4.1, in the regions between approximately 900 °C and the *solidus* curves, only the main fcc phase and $M_{23}C_6$ precipitation are predicted. The maximum C solubility in the matrix is achieved approximately at 1313 °C for 0.47 at.% of C. The *solvus* curve shape is adequate for precipitation hardening treatments, although the second phase fraction will not be high due to the low C mole percentages. Considering this scenario, two possible alloys were envisioned, as well as the $Cr_{40}Co_{30}Ni_{30}$ alloy for comparison purposes. First, with a composition of 0.2 at.% C (material "B") an alloy that would experience precipitation hardening at 900 °C, but would be single phase (all carbon in solid solution) above 1092 ºC. A homogenized (above the solvus curve) and water quenched sample should display no precipitation.

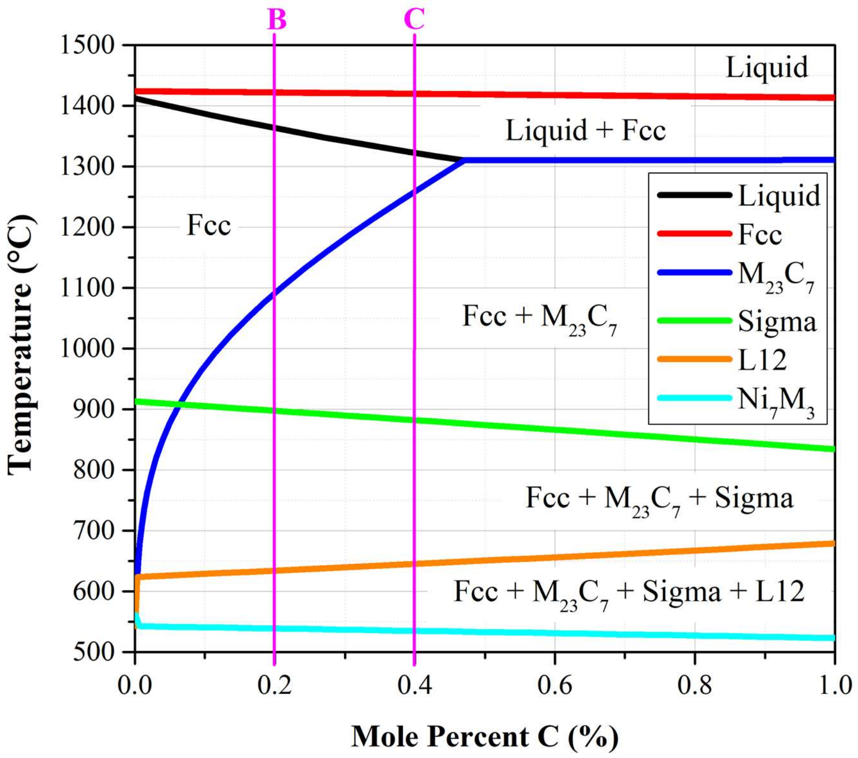

Figure 4.1. Isopleth with a composition starting at $Cr_{40}Co_{30}Ni_{30}$ and up to $Cr_{39}Co_{30}Ni_{30}C_1$. This graph was plotted in Thermo-Calc with the TCHEA5 database. Materials "B" and "C" compositions ($Cr_{39.8}Co_{30}Ni_{30.2}$ and $Cr_{39.6}Co_{30}Ni_{30}C_{0.4}$ respectively) are evidenced by magenta vertical lines.

The second alloy was intended to have higher concentrations of C, namely 0.4 at.%. From Figure 4.1, it is possible to see that, for this composition (and for 0.2 at.% as well), precipitation hardening can happen through the ideal stages (dissolution, quenching and ageing). As will be pointed out further on the text, some processing stages were carried out at 1100 °C. CALPHAD predicts that in this temperature, for material C, half carbon content should be in solid solution (SS) and half constituting precipitates. This was intended so that in the initial processing stages of this work, the carbides should be present. With this, materials B and C in equilibrium at 1100 °C should have the same amount of carbon in SS, as to allow an evaluation of the specific contributions of CD to the mechanical resistance (precipitation versus SS).

At 900°C the main difference between both alloys (after processing at 1100 °C) should be the volume fraction of precipitates (and their distribution), which is also of interest. Alternatively, with adequate solution treatment, all carbon in B and C should be in the form of interstitials. The mentioned differences between the two alloys are intended to study the effects of CD and carbide distribution on the microstructure and mechanical properties of these elements in SS and as precipitates.

4.2 Alloy Production

Figure 4.2 is a flowchart summarizing all the stages of sample production and processing. Additionally, colors are often used to indicate each material, those being red for $Cr_{40}Co_{30}Ni_{30}$ (A), green for $Cr_{39.9}Co_{30}Ni_{30}C_{0.1}$ (B) and blue for $Cr_{39.6}Co_{30}Ni_{30}C_{0.4}$ (C). In the appendix, Figure A.3 shows a compilation of all samples, with their respective processing and naming.

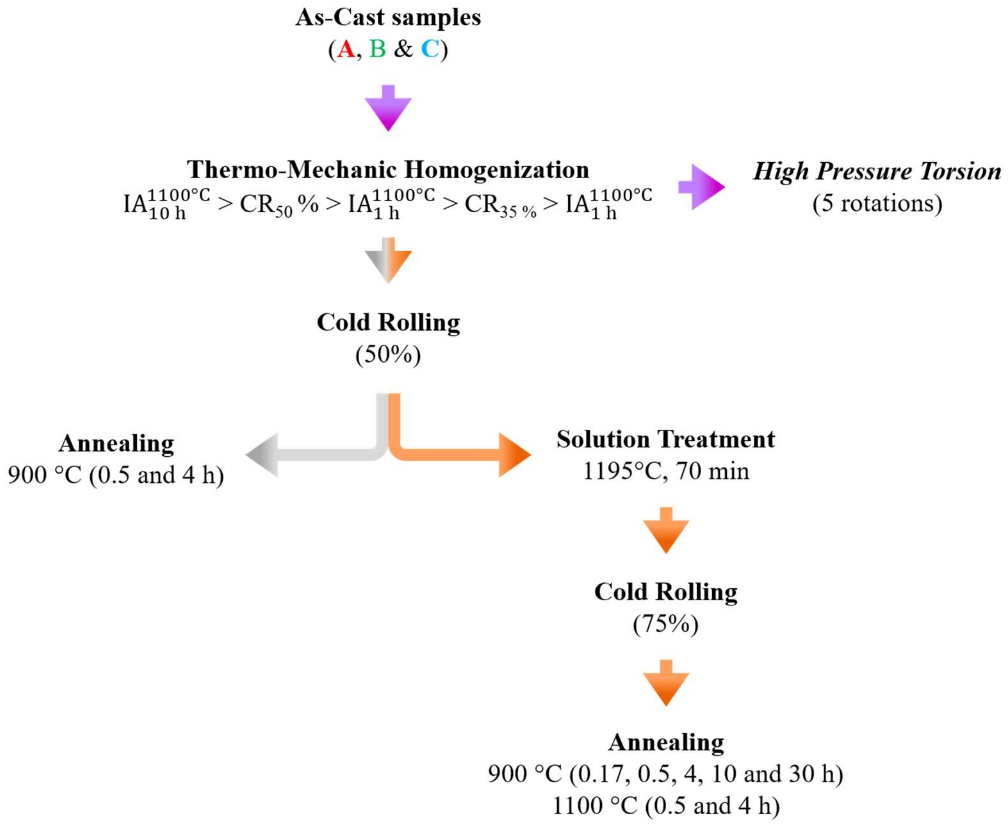

Figure 4.2. The full fabrication and processing of the A, B and C samples is represented through a flowchart. The three routes are indicated by light green (HPT), Grey (no dissolution) and orange (with solution treatment). three processing routes are: HPT (purple), with solution treatment (orange) and without solution treatment (grey).

The alloys were obtained through arc melting Cr, Co and Ni (purities above 99.9 w.%) under a controlled argon atmosphere. Carbon was added via a Cr-C pre-alloy. Samples were flipped and re-melted four times on a copper crucible to ensure chemical homogeneity. An Edmund-Bühler furnace was used. To assess the real carbon concentration in the as-cast condition, the samples B and C were analyzed via LECO® Sulfur/Carbon combustion analysis technique. The results are presented on table 4.1. The nominal compositions observed were $Cr_{40}Co_{30}Ni_{30}$, $Cr_{39.8}Co_{30}Ni_{30}C_{0.2}$ and $Cr_{39.6}Co_{30}Ni_{30}C_{0.4}$ for the A, B and C materials respectively.

Table 4.1. Intended and corrected (for carbon) samples compositions

Material	Evaluation	Composition (at. %)			
		Cr	Co	Ni	C
A	intended	**40.000**	**30.000**	**30.000**	-
B	intended	39.800	30.000	30.000	0.200
	corrected	**39.850**	**30.012**	**30.012**	**0.126**
C	intended	39.600	30.000	30.000	0.400
	corrected	**39.577**	**30.005**	**30.005**	**0.383**

4.3 Initial Processing

The as-cast samples were submitted to a homogenization heat treatment in a *Linn Elektro Therm* electric furnace, at 1100 °C for 10 hours, followed by water quenching with agitation. The samples were only inserted on the furnace after it reached the 1100 °C temperature. This heat treatment step is essential not only as it secures a better homogenized composition throughout all of the sample's volume, but also as it promotes the dissolution of precipitates eventually formed during casting. However, it should not dissolve all the carbides in sample C, as can be seem in the phase diagram (Figures 4.1). All high temperature (above 0.5 homologous temperature) treatments in this work were followed by water quenching with agitation (at room temperature) to prevent the formation of second phase particles.

To refine the microstructure, accumulate deformation for the recrystallization process, and give the samples a more adequate shape, cold rolling (CR), at room temperature, was chosen as the mechanical forming process. This processing stage was accomplished, after the annealing at 1100 °C and water quenching, with a *Fröhling* rolling mill at 6.5 m/min rolling speed. Since the arc melted samples' shape was not ideal to undergo high rolling reductions without material cracking, it was decided to separate the forming process in three stages. Between each stage the samples underwent an intermediate annealing (IA) at 1100 °C for 1 hour, so that there could be a full stress relief (with recrystallization) and, therefore, the next rolling stage would be less prone to cracking. At this temperature and duration, the heat treatment process was more likely to promote a homogeneous recrystallization of the samples [49].

Thus, the first cold rolling stage purpose was mainly to change the samples' shape closer to a plate-like shape. The second stage objective was to help refine the microstructure and amplify the sample's area (so there would be a larger size to remove subsequent samples and perform this study). The third and final stage was conducted aiming for a final thickness of around 2 mm (equivalent to a 50 % reduction), and no further homogenization was done as the main goal was to accumulate deformation energy for the recrystallization process. As such, the processing after casting and up to the last cold rolling mentioned above (which is the third), can be understand as a Thermo-mechanical homogenization (TMH). The full TMH main purpose was to achieve chemical and microstructural homogeneity beyond what would be possible with only heat treatments. During any CR processing in this work there was no control of sample's width.

Table 4.2 summarizes the primary results of the cold rolling forming process for each sample. It must be recalled that the samples underwent homogenization treatments at 1100 °C, for 10 hours before the start of the cold rolling process, and for 1 hour between the first and second stages as well as between the second and third stages.

Table 4.2. Cold rolling results overview

Samples (rolling stage)	Initial thicknes (mm)	Final thickness (mm)	reduction (%)	number of steps	average reduction by step (%)
A (1)	11.28	6.28	44%	17	3%
A (2)	6.28	4.08	35%	9	4%
A (3)	4.08	2.00	51%	15	3%
B (1)	11.50	6.29	45%	19	2%
B (2)	6.25	4.09	35%	9	4%
B (3)	4.09	2.04	50%	11	5%
C (1)	12.32	6.10	50%	24	2%
C (2)	6.10	4.01	34%	21	2%
C (3)	4.05	2.03	50%	33	2%

After the CR procedure discussed above, the subsequent processing was separated in two parts/routes. Firstly, to study the effect of precipitation occurring only during the annealing treatment, an additional solution treatment (ST) was carried out at 1195 °C (with both 1 and 4 h treatment's durations tested, for which the results are discussed in section 5), after the third CR step from Table 4.2. Then the samples were CR once again and, at last, they were annealed at different conditions. The cold rolling after this ST reduced the thickness of each sample from the approximately 2 mm size to an average of 0.5 mm (75 % reduction). The second processing route studied in this work consisted in, instead of performing the carbide dissolution step (ST), performing the annealing treatments immediately after the third CR step from table 4.2.

4.4 Annealing Treatments

After cold rolling, the "mother" samples (A, B and C rolled plate-like samples) needed to be sectioned into multiple pieces so that different heat treatments conditions (annealing) could be studied. The sectioning was made by wire electrical discharge machining, since it generates less heat when compared to simple mechanical machining or laser machining. It also yields a better surface finish.

The main annealing treatment temperature chosen was 900 °C with times of 0.5 and 4 h being tested for all the samples. However, the samples in the ST route were also annealed at 900 °C for 0.17, 10 and 30 h. Additionally, the A and C alloys in this processing route were studied after annealing at 1100 °C for 0.5 and 4 h. 900 °C was chosen because it is the limit of sigma phase (which is deleterious) formation (for material A) and literature indicates that its precipitation kinetics are slow [49]. As well as being a temperature for which most carbon should be outside of SS. As mentioned before, at 1100°C for the material C, half of the carbon content should be in SS and the other half precipitated in carbides, that is why it was also selected.

Phase fraction as a function of temperature graphs were plotted, on Thermo-calc™ software with the TCHEA5 database, for each sample composition. These graphs are shown in Figures 4.3 to 4.5. It is important to note that these simulations already consider the real C content measured by the LECO® combustion analyzer (as presented in table 4.1).

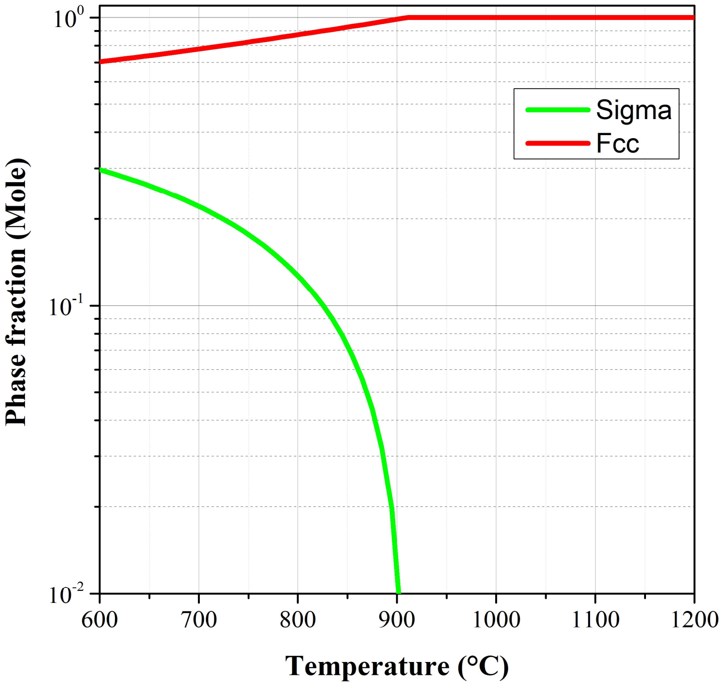

Figure 4.3. Phase fraction as a function of temperature for the sample A ($Cr_{40}Co_{30}Ni_{30}$).

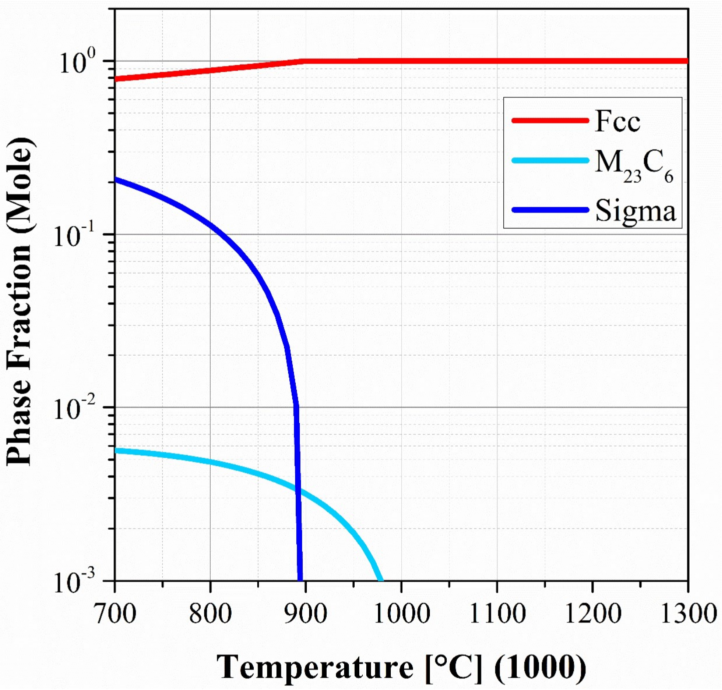

Figure 4.4. Phase fraction as a function of temperature for the sample B ($Cr_{39.9}Co_{30}Ni_{30}C_{0.1}$).

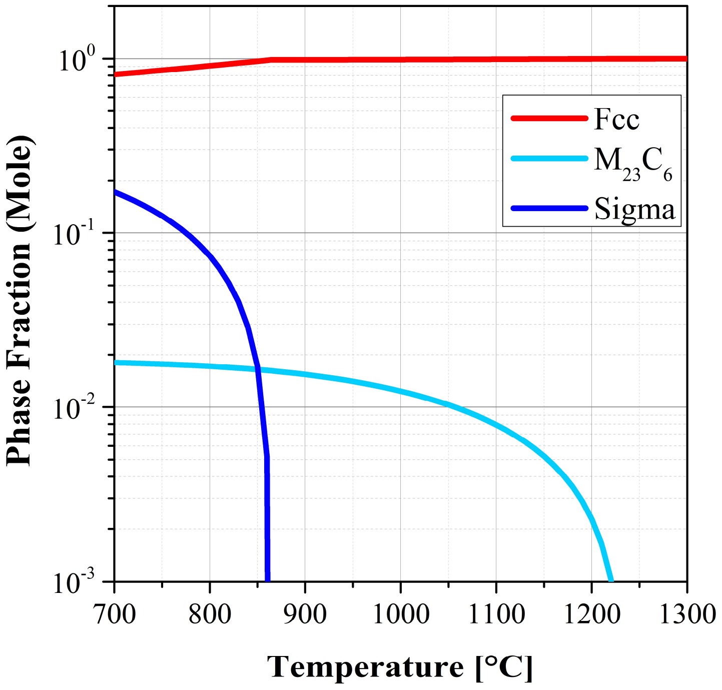

Figure 4.5. Phase fraction as a function of temperature for the sample C ($Cr_{39.6}Co_{30}Ni_{30}C_{0.4}$).

As it can be noticed in the phase fraction graphs, the sigma phase starts to precipitate, around 900 °C, for each of the compositions. However, the annealing treatments (as mentioned before) will be performed in temperatures equal or superior to 900 °C.

4.5 High Pressure Torsion

After the end of TMH, a sample from material A and one from C were prepared and further processed under quasi-constrained High Pressure Torsion (HPT) after being compressed and machined to fit the equipment [50]. The procedure was carried out with a pressure of 6 GPa pressure at 1 rpm for up to 5 rotations (1800°). The produced disks had a diameter of 8 mm and 0.8 mm thickness. HPT processing was chosen to study the effect of carbon-doping under severe plastic deformation, and the characteristics of an ultra-fine grained distribution of grain sizes for the A and C materials.

4.6 Microstructural Characterization

Figure 4.6 is a flowchart summarizing all the stages of sample production and processing. In text, the identification of each individual sample is made in agreement with Figure 4.6. Additionally, colors are often used to indicate each material, those being red for $Cr_{40}Co_{30}Ni_{30}$ (A), green for $Cr_{39.9}Co_{30}Ni_{30}C_{0.1}$ (B) and blue for $Cr_{39.6}Co_{30}Ni_{30}C_{0.4}$ (C). In the appendix, Figure A.3 shows a compilation of all samples, with their respective processing and naming

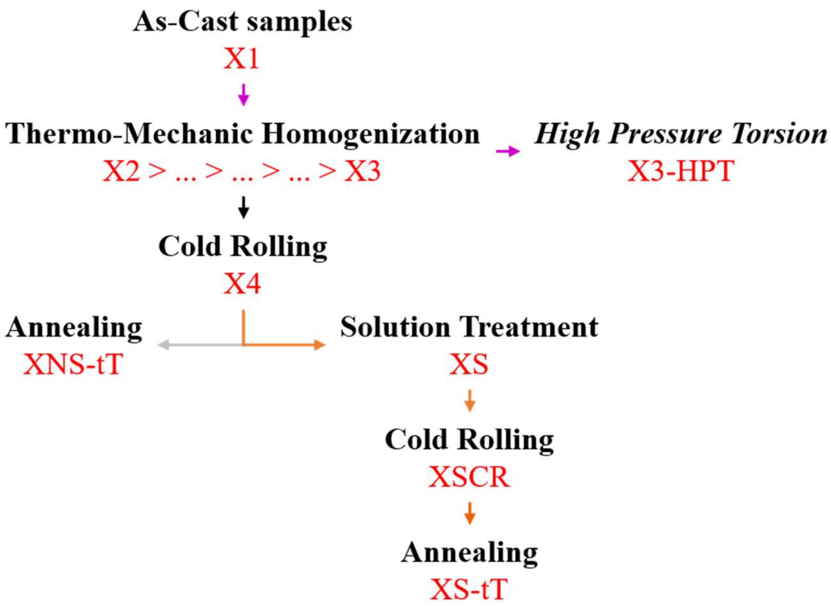

Figure 4.6. Identification coding for each processing condition. X is a variable indicating A, B or C material. S and NS define the processing routes with and without solution treatment respectively. “T” indicates the annealing treatment temperature, while “t” is the duration. For example, a $Cr_{40}Co_{30}Ni_{30}$ sample without prior solution treatment annealed at 900 °C for 4 h was named ANS-4h900.

Optical microscopy (OM), scanning electron microscopy (SEM) and transmission electron microscopy (TEM) were the main techniques utilized to study the microstructure and its features for all the samples. To assist the microstructure characterization, analysis such as X-ray diffraction and energy dispersive spectroscopy (EDS) were also employed

4.6.1 Sample Preparation

For the OM, SEM, EDS techniques, it was adopted a standard metallography preparation sequence, consisting of selecting the region of interest, mounting, grinding, polishing and etching when needed. For the XRD and microhardness analysis, a similar sequence was employed, but with grinding as the final step. Since the forming process was CR and one of the main interests is the characterization of grain size, the preferred region of analysis was the longitudinal section (in regard to the rolling direction). However, the transversal section can also be considered for grain size evaluation, and so, it may become an alternative due to sample sizes being small, or even be characterized purely for comparison purposes [51].

The samples were prepared by hot mounting with Bakelite resin. Grinding was performed with SiC papers following a grit sequence consisting mainly of # 200, # 400, # 600, # 1200 and # 2000 with water. After grinding, polishing started in a polishing cloth with 9 μm diamond abrasive paste applied, then with 3 μm and the final polishing with 1 μm abrasive granulometry. Samples were etched with Kallings number II, applied with cotton pressed rapidly multiple times (30 s for annealed and 15 s for the deformed samples) without scrubbing.

4.6.2 Optical and Scanning Electron Microscopy

Optical Microscopy analysis and imaging was carried out in a Leitz Metallux II microscope equipped with a 51 MP resolution digital microscope camera at 10 times zoom. A FEI microscope, model Inspect S50 (with W source), was used for SEM imaging and EDS analysis. As mentioned before, the longitudinal section was the main region selected for both microscopies analyses. Unless specified otherwise, all micrographs in this work are from the longitudinal sections with the rolling direction parallel to the page's width.

Average grain size measurements were made by the "Abrams Three-Circles Intercept Procedure", in accordance to the American Society for Testing and Materials (ASTM) standard test methods for determining average grain size, or ASTM E112-13 [52]. The error was estimated as the 95 % confidence interval. Error propagation was used when necessary. Twins were not considered for the measurements, only grain boundaries.

4.6.3 X-Ray Diffraction

XRD technique was carried out with a PW1710 Philips-Panalytical diffractometer, that has a Bragg-Brentano geometry. A Cu Kα (1.540589 Å) radiation produced with a 50 kV voltage and 35 mA current, and filtered by a graphite monochromator. The characterization range comprehended 10 to 120° coverage (for most samples, however, some were characterized from 10 to 90°), with a 0.02° step size and 2.5 s scan time by step. The analyses were made on the sections normal to rolling.

4.6.4 Transmission Electron Microscopy

Samples of key conditions were chosen for TEM analysis on a Tecnai G^2 F20 SuperTwin FEI electron transmission microscope with a 200 kV operating tension. The HPT were also analyzed with a Thermo-Fisher/FEI Titan electron transmission microscope operating at 300 kV, equipped with a STEM system and a High Angle Annular Dark Field (HAADF) detector. The main goal was to characterize the second-phase particles and the less prominent features of the microstructure such as precipitates and possibly stacking faults and nanotwins. Bright field (BF), dark field (DF), selected area electron diffraction (SAED) and high-resolution TEM (HRTEM) were the imaging techniques utilized. Center of Symmetry (COS) maps were plotted to help identify and differentiate the microstructure on HAADF-STEM images . This method measures the geometric variation from an ideal fcc array (on a <110> zone axis), such as that stacking faults and hcp regions are highlighted. A programming code was created from the guidelines of Vorontsov et al.'s work [53] and is described in Appendix B.

The HPT samples were further characterized on a Tecnai G20 TEM for orientation and phase mapping using the "Automatic Crystal Orientation/Phase Mapping for TEM" (ASTAR), performed on areas of 990 x 990 nm^2 at a step size of 10 nm. This method is analogous to EBSD (Electron Backscattered Scanning Diffraction) for SEM. The data treatment was carried out on the OIM^{TM} software. Grain size measurement for the HPT samples were made with the ASTAR data, and in agreement with the ISO 13067:2020 guidelines.

4.7 Mechanical Tests

All samples had their hardness measured with a Vickers microindenter coupled on a Zeiss Axiophot optical microscope, in accordance to the ASTM standard test method for microindentation hardness of materials, or ASTM E384-17 [54]. The microidentation conditions were: 500 gf load with a hold time of 10 s. All the error bars from the hardness plots were estimated from the standard deviations and with error propagation when necessary.

For the HPT samples hardness was evaluated throughout the full diameter of each disk. Figure 4. illustrates the pattern of indentations made for the rolled (Figure 4.8, left) and HPT (Figure 4.8, right) samples. For the latter, an average value was estimated for each set of 4 groups, as indicated by the red dots in Figure 4.7. The mechanical strength of the HPT processed samples was also measured with a plane strain compression test [55] at a strain rate of 10^{-3} s^{-1}.

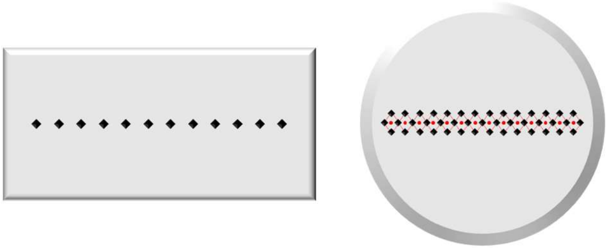

Figure 4.7. Indentation pattern for the Vickers microhardness measurements of the rolled (left) and HPT (right) samples. For HPT the hardness values were evaluated in respect to the disk radius, and are given by the average value between each group of 4 indentations (red dots).

5 PRIMARY PROCESSING

5.1 Overall Characterization of The Microstructure Features.

In this section the general and common observed characteristics of the studied materials' microstructure and its features are shown. With a focus on simple fundamentals that will serve as a guide to further sections.

As mentioned in the materials and methods section of this work, after casting the $Cr_{40}Co_{30}Ni_{30}$ (A1), $Cr_{39.9}Co_{30}Ni_{30}C_{0.1}$ (B1) and $Cr_{39.6}Co_{30}Ni_{30}C_{0.4}$ (C1) ingots were thermo-mechanically homogenized in 5 stages. The first one consisted in an intermediate annealing (IA) or simply homogenization treatment at 1100 °C for 10 h. Samples were removed from the ingots both at this (indicated by the number 2) and in the as-cast (referred as 1) conditions, and their microstructures were characterized. Figure 5.1 and 5.2 show the main observations from these analyses for the $Cr_{40}Co_{30}Ni_{30}$ and $Cr_{39.6}Co_{30}Ni_{30}C_{0.4}$ samples respectively.

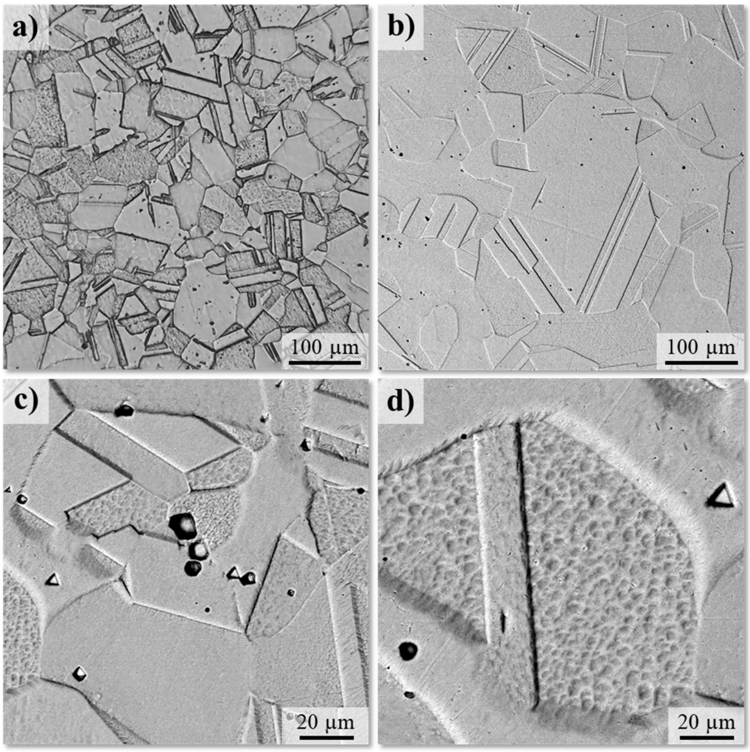

Figure 5.1. Microstructure characterization of the $Cr_{40}Co_{30}Ni_{30}$ alloy after homogenization at 1100 °C for 10 h (A2). Figure (a) is an optical micrograph, whereas (b-d) are SEM images in the backscattered electron (BSE) mode. The microstructure was revealed with Kallings N°II etchant.

The A2 sample's micrographs were chosen to depict the fcc matrix features that are seen throughout all the samples from this work (with exception to the HPT route). As such, it is possible to see that the studied materials exhibit a common fcc microstructure, with a considerable amount of annealing twins. The grain size distribution is somewhat heterogeneous. Both polishing and etching can result in pitting corrosion which leaves the images full of small black spots (Figures 5.1a-b). The shape of these features can be seen at Figure 5.1c. Finally, depending on grain orientation, the etched (with Kallings N°II) surface can appear rough, this is exemplified by Figure 5.1d.

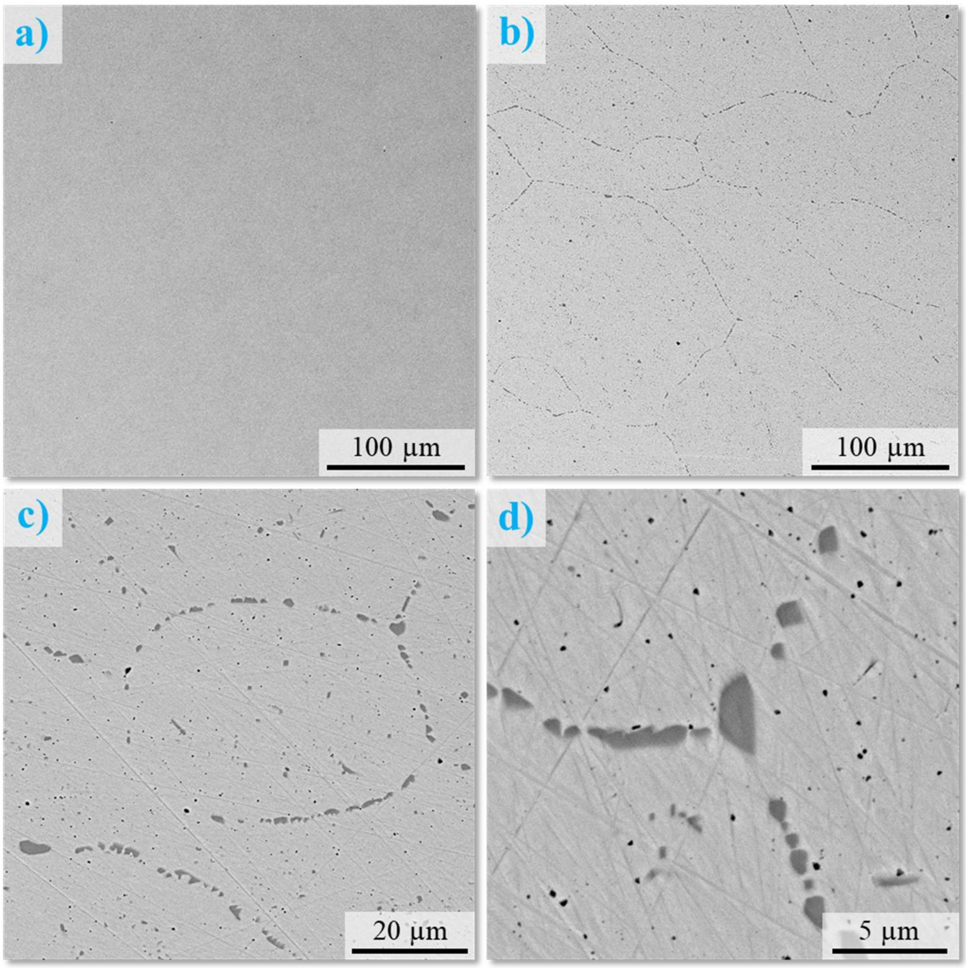

Figure 5.2. SEM-BSE imaging of the $Cr_{39.6}Co_{30}Ni_{30}C_{0.4}$ alloy in the as-cast condition (a) and after homogenization at 1100 °C for 10 h (b-d). Dark grey spots are $M_{23}C_6$, and are located primarily on grain boundaries. Black spots are form pitting corrosion. A triple point grain boundary junction can be better seen at (d). No etching was applied.

For the $Cr_{39.6}Co_{30}Ni_{30}C_{0.4}$ material, the difference between C1 and C2 samples' microstructures is noticeable in Figure 5.2. While there are virtually no second phases present in the as-cast condition (a consistent screening was made in the whole sample), dark grey spots were detected after homogenization at 1100 °C. According to the CALPHAD calculations made (Figure 4.5), these particles should be $M_{23}C_6$ carbides. This is confirmed by characterizations presented later on the text. The carbides are observed mainly on grain boundaries, hinting to their contour at the micrograph. As such, the images indicate that heterogenous precipitation occurred after heating at 1100 °C for 10 h. No carbides were detected for the B samples up to the mentioned processing stage (for B1 and B2).

It is important to keep in mind that the effects of CD are different for the carbon in solid solution (acting as an interstitial) or when it precipitates as the $M_{23}C_6$ particles. Figure 5.3 shows the predicted volumetric phase fraction (%) of the carbide and the carbon composition (at.%) in the fcc matrix, for C and B samples at different temperatures. These graphs were plotted with the CALPHAD calculations results. At 900 °C, both B and C have the same amount of carbon dissolved in the matrix (0.06 at.%), and should experience similar interstitial strengthening. However, as temperature rises to about 1000 °C and beyond, the B samples' carbon content remains constant (0.126 at.%) since there will be no $M_{23}C_6$ in equilibrium. For the $Cr_{39.6}Co_{30}Ni_{30}C_{0.4}$ alloys, as mentioned before, there should always be some fraction of carbide precipitated (except after casting, which involved higher temperatures). And thus, solid solution strengthening should be improved the higher the thermal processing temperature.

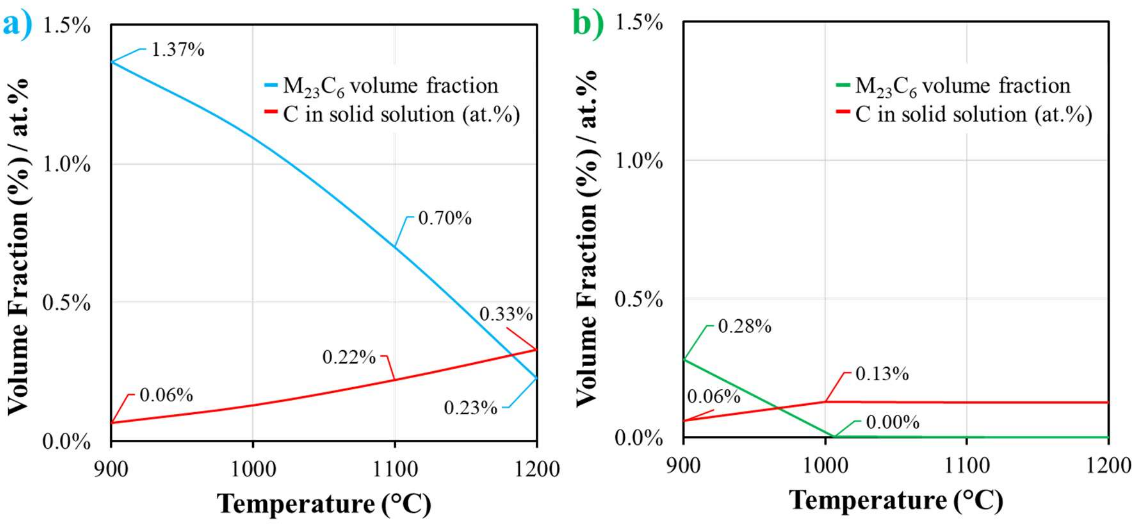

Figure 5.3. Thermodynamic prediction of the amount of carbon (at.%) in solid solution and $M_{23}C_6$ carbide's volume fraction (%) as a function of the (a) $Cr_{39.6}Co_{30}Ni_{30}C_{0.4}$ and (b) $Cr_{39.9}Co_{30}Ni_{30}C_{0.1}$ alloys temperatures.

The chemical compositions of the studied materials were measured with SEM-EDS from multiple samples throughout the whole processing. Table 5.1 summarizes the observed results and it is possible to see that not only the $Cr_{40}Co_{30}Ni_{30}$ composition was achieved, but also with good homogeneity (small standard deviation values). The carbide's characterization shows that, although the measured compositions are comparable to the expected (> 70 at.% of Cr and 20.7 at.% carbon), the higher carbon content (and thus difference in the $M_{23}C_6$ predicted stoichiometry) can be explained by the EDS detector's limited sensitivity for lighter elements.

Table 5.1. EDS micro-analysis of each materials' matrix regions and of the $M_{23}C_6$ carbide

Phase	**Composition (at.%)**			
	Cr	**Co**	**Ni**	**C**
A	40.4 ± 0.4	29.3 ± 0.5	30.2 ± 0.6	-
B (matrix)	40.3 ± 0.3	29.3 ± 0.3	30.5 ± 0.5	-
C (matrix)	40.5 ± 0.6	29.4 ± 0.2	30.1 ± 0.5	-
$M_{23}C_6$	63.1 ± 3.9	4.6 ± 0.8	4.2 ± 0.5	28.1 ± 4.2

The precipitation particles seen in Figure 5.2 are present in all the $Cr_{39.6}Co_{30}Ni_{30}C_{0.4}$ annealed samples, as well as some other samples. To confirm these are indeed $M_{23}C_6$ carbides, a SAED analysis was carried out on the CS-0.5h900 sample and is presented in Figure 5.4 alongside the respective TEM image of the observed region. The SAED patterns confirm that both the matrix (Figure 5.4b) and the carbide (Figure 5.4c) are fcc (Fm-3m space group). However, their cell parameters (*a*) are different, being 3.57 Å and 10.65 Å respectively (measuring via the SAED pattern). This matches the observed carbides with $M_{23}C_6$, since the other possible carbides (M_7C_3 as an example) are all non-cubic.

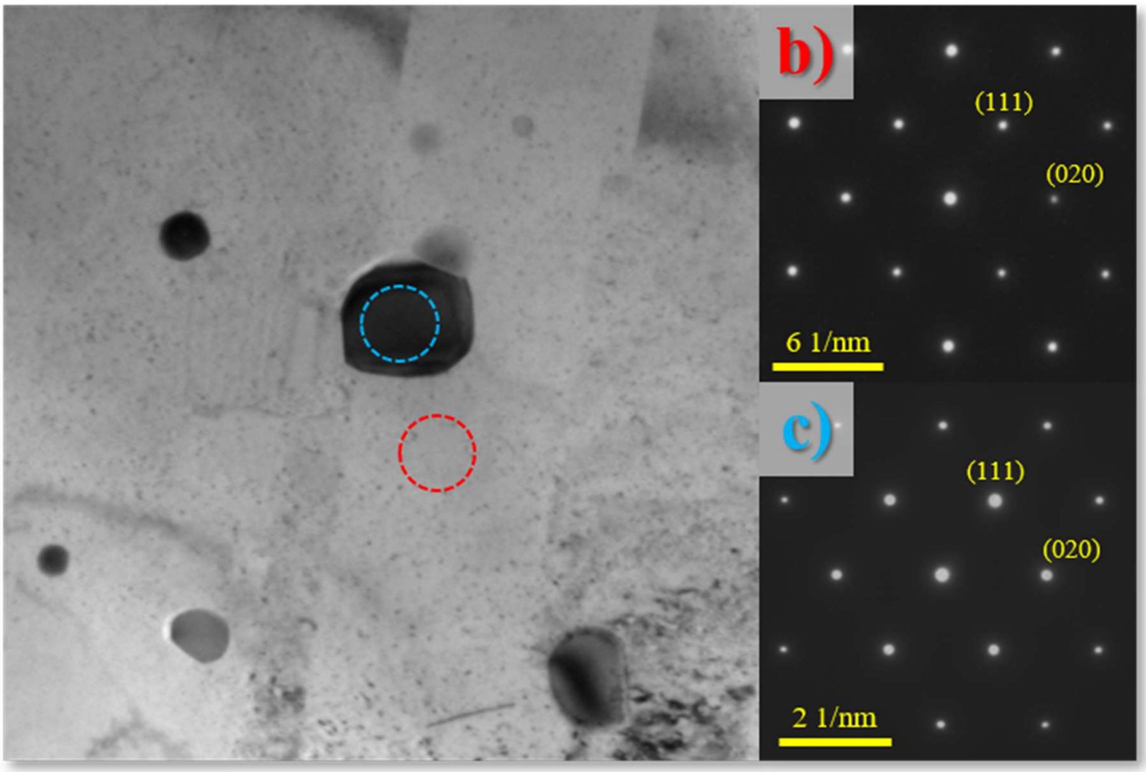

Figure 5.4. TEM bright field image and SAED analysis of the CS-0.5h900 sample in the normal rolling plane. The [101] zone axis SAED patterns for the (b) matrix and the (c) carbide were measured in the areas indicated by the red and blue circles respectively.

The materials were also characterized via XRD analysis, for some key conditions. The experimental results obtained are represented at Figure 5.5. The $M_{23}C_6$ diffraction peaks are only noticeable for the CS-0.5h900 samples' pattern. For all other conditions, only the fcc matrix peaks are present. A more in detail discussion of the XRD results will be made in the next sections of this work. Utilizing the peak position (converted to theta) data from Figure 5.5, the lattice parameter was measured to be 3.571 ± 0.006 Å for $Cr_{40}Co_{30}Ni_{30}$ (material A), matching the value observed for the SAED. The unit cells calculated with the XRD and SAED results were plotted for the $Cr_{40}Co_{30}Ni_{30}$ and $M_{23}C_6$ phases respectively, and are shown in Figure 5.6.

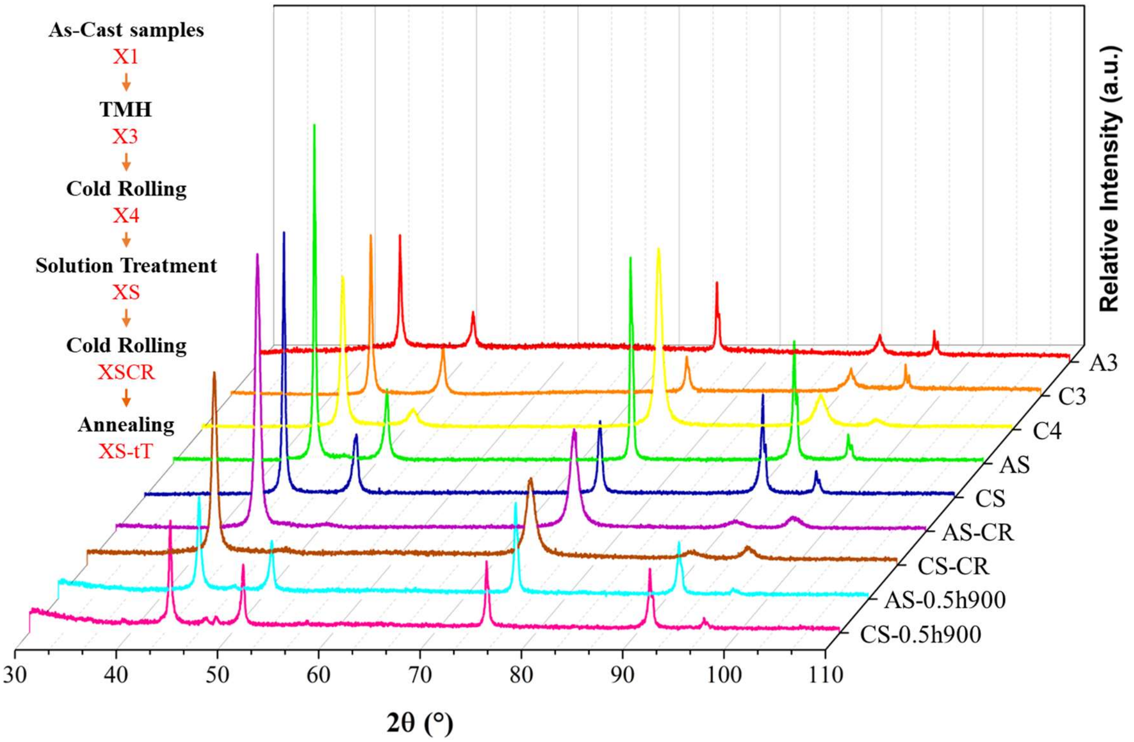

Figure 5.5. XRD results for the solution treated processing route. All samples are FCC.

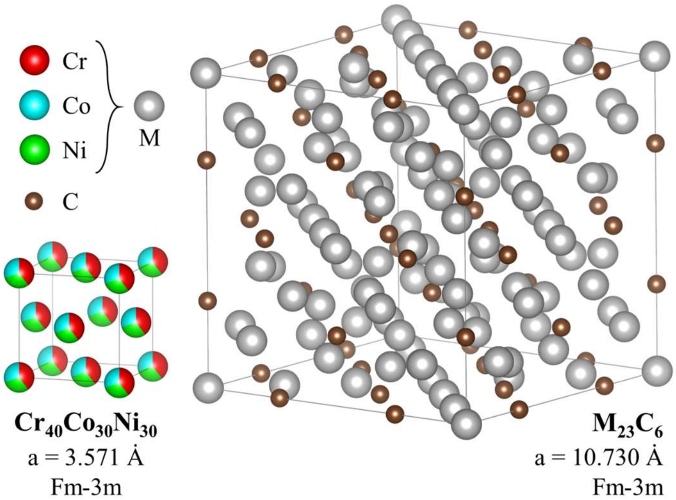

Figure 5.6. Fcc (Fm-3m) unit cells plotted with the VESTA^{TM} software for the $Cr_{40}Co_{30}Ni_{30}$ (matrix, calculated with XRD results) and $M_{23}C_6$ carbides (from SAED analysis). $Cr_{40}Co_{30}Ni_{30}$ was considered as having an ideal random solid solution.

From the XRD results, it was observed an increase in the matrix's lattice parameter the higher the carbon content in solid solution (Figure 5.7). This is expected since the interstitial solutes generate elastic compression fields and thus expand the structure [23,25]. From figure 5.7 it is possible to see that the lattice value went from 3.571 (without carbon) to 3.577 (0.22 at.%) and then to 3.582 Å (0.33 at.%). One-way ANOVA analysis proved this to be a statistically significant increase.

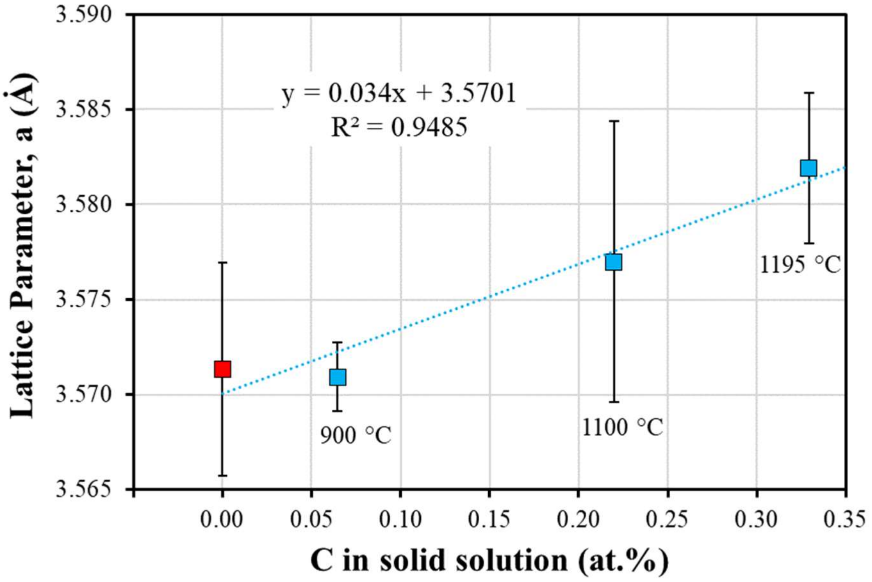

Figure 5.7. Change in the fcc matrix's lattice parameter with carbon content. Blue indicates the experimental data collected from $Cr_{39.6}Co_{30}Ni_{30}C_{0.4}$ samples, while red is from the A alloys. The annealing times are represented below the respective experimental points.

5.2 From Thermo-Mechanical Homogenization to Solution Treatment

After annealing for 10h at 1100 °C, the alloys were further homogenized through multiple CR and IA (with water quenching) processing, as mentioned before. After the complete thermo-mechanical homogenization (TMH) their microstructure was again characterized. Figure 5.8 shows Vickers microhardness histogram results comparing the samples at the first (2) and last (3) stages of TMH.

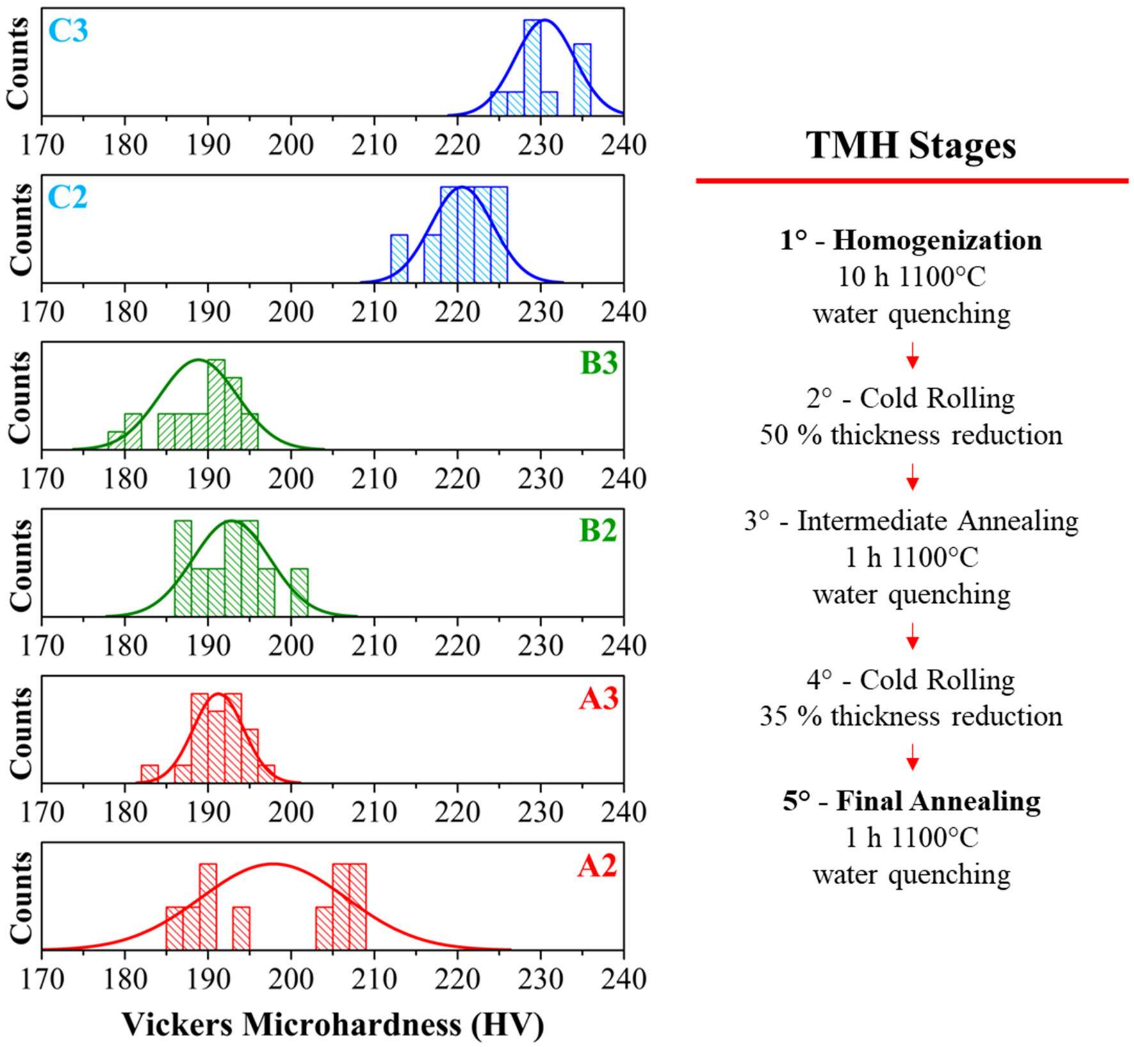

Figure 5.8. Hardness histogram plots for the (a) $Cr_{40}Co_{30}Ni_{30}$ (b) $Cr_{39.9}Co_{30}Ni_{30}C_{0.1}$ and (c) $Cr_{39.6}Co_{30}Ni_{30}C_{0.4}$ alloys after the start (2) and end (3) of TMH. A descriptive flowchart with all the thermo-mechanical homogenization processing stages is presented on the right.

From the microhardness measures it is possible to see that a well stablished homogeneity was achieved for the B and C alloys since the first stage. However, it was beneficial for A to undergo the full TMH, since A2 showed a disperse microhardness. The differences in the hardness values (between 2 and 3 for each alloy) are probably due to grain size distributions, since before TMH their morphologies were not equiaxial. As such, the processing was also important to change the remaining regions of the microstructure with as-cast columnar shaped grains (see appendix Figure A.1) to fully equiaxial. The microstructures for A3, B3 and C3 are shown in Figure 5.9. Their grain sizes are also represented and it is possible to see that 0.4 at.% carbon-doping resulted in an average grain size 60 % smaller.

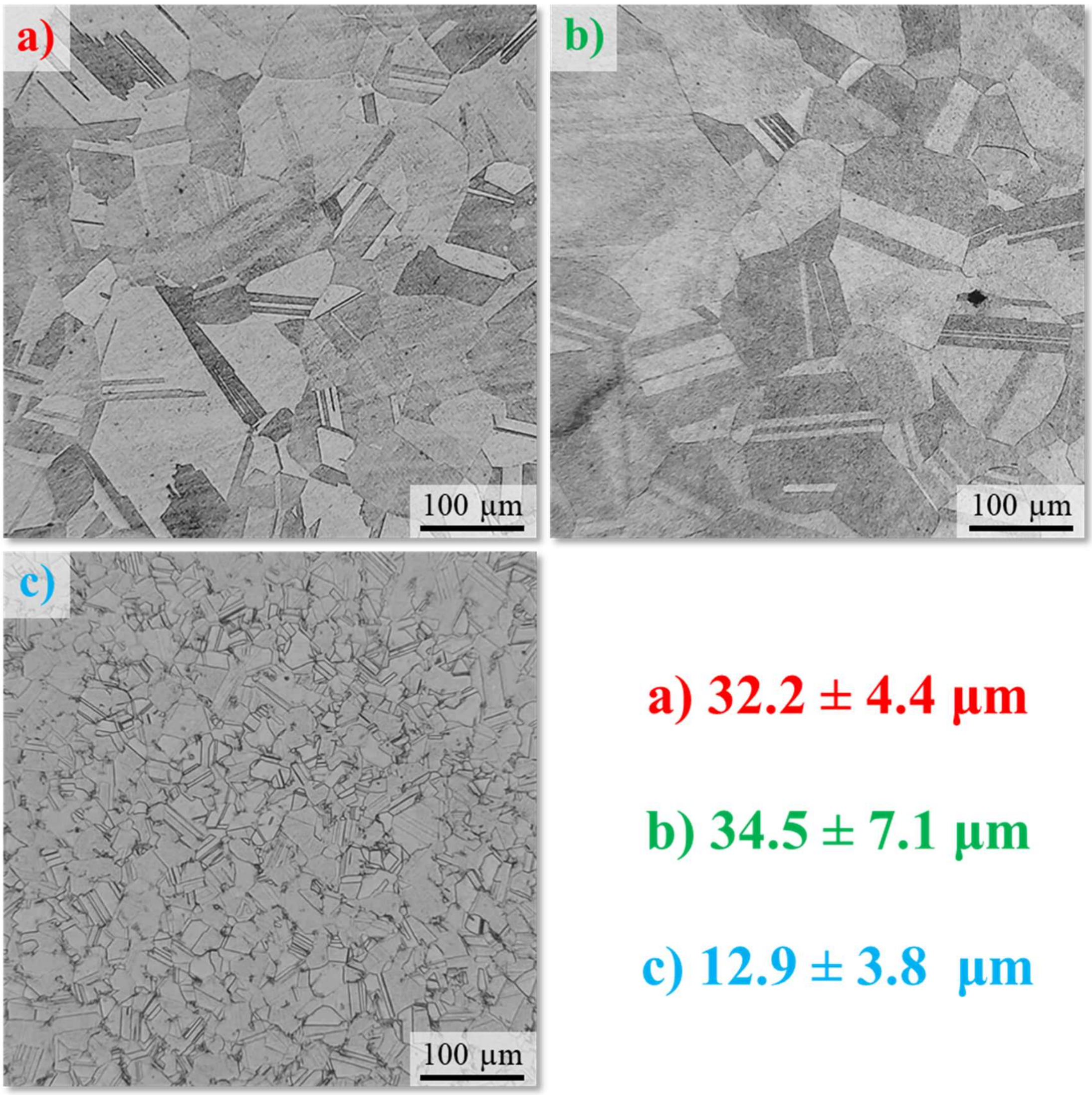

Figure 5.9. Microstructural characterization with OM of the (a) $Cr_{40}Co_{30}Ni_{30}$ (b) $Cr_{39.9}Co_{30}Ni_{30}C_{0.1}$ and (c) $Cr_{39.6}Co_{30}Ni_{30}C_{0.4}$ alloys after TMH. Etched with Kallings N°II. The respective average grain sizes are disclosed in the bottom right corner of the image.

The microstructure for the C3 Sample can be seen more closely in the SEM and OM micrographs shown in Figures 5.10 to 5.12. At the end of TMH the carbide distribution is not concentrated only on grains boundaries as it was on the first stage. This is clearly visible in Figure 5.10a and is an outcome of the cold rolling and annealing processing. Figure 5.10b is a zoomed view on the precipitates. A higher fraction of sub-micron particles is seen when compared to Figure 5.2 (C2).

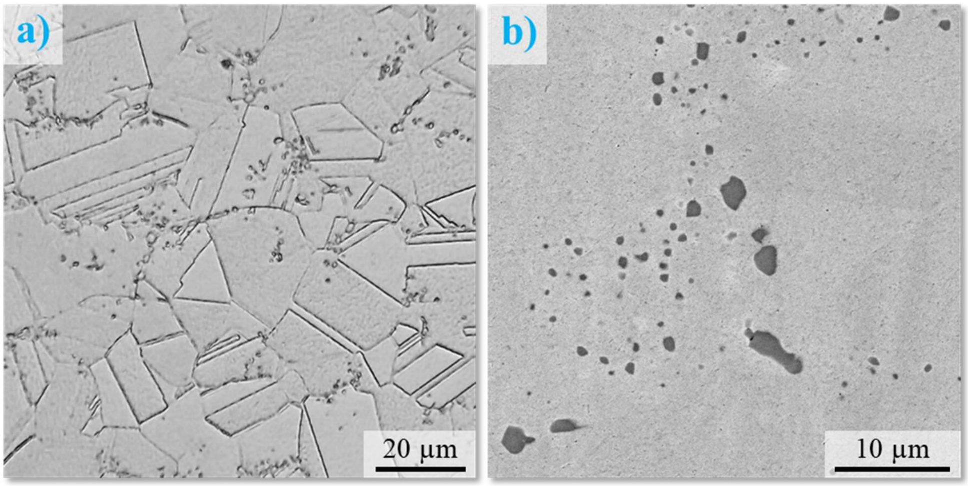

Figure 5.10. Microstructural characterization of the $Cr_{39.6}Co_{30}Ni_{30}C_{0.4}$ (C3) sample with (a) OM and (b) SEM on BSE mode.

A spatial distribution map for the chemical elements was made via EDS for the C3 sample and is presented in Figure 5.11. Figures 5.12a-b show that for some regions of sample C3 the $M_{23}C_6$ particles have become concentrated on bands. This morphology could be a result of the significant differences in the hardness values between each phase affecting their distribution under processing with high levels of strain. However, non-banded regions are also present in large scale, as shown in Figure 5.12c.

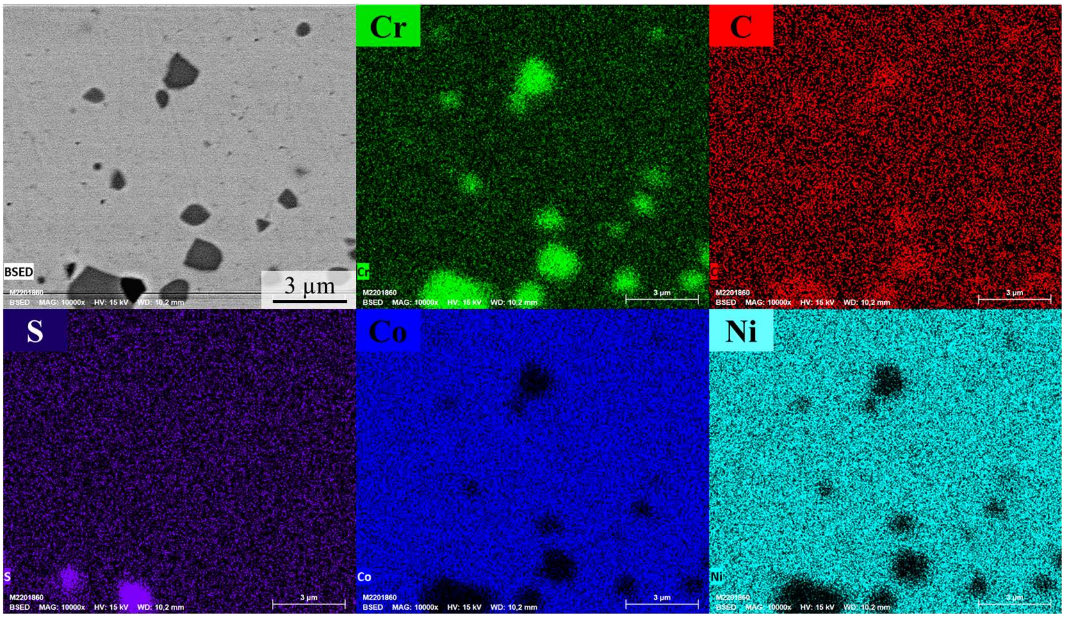

Figure 5.11. EDS spatial distribution map for the $Cr_{39.6}Co_{30}Ni_{30}C_{0.4}$ alloy after TMH. Grey particles are $M_{23}C_6$ carbide and the dark spots are sulfide inclusions.

After TMH, the A, B and C materials were cold rolled to a thickness reduction of 50 %. This is equivalent to 70 % true strain. The C4 samples' microstructures are shown in Figure 5.12d. The CR appeared to have broken to some degree a fraction of the $M_{23}C_6$ carbides. Etching revealed a high amount of what appears to be deformation bands after deformation, which can be seen in Figure 5.13. These features were observed as parallel (Figure 5.13b) or interpenetrated lines (Figure 5.13c). For the latter scenario, it seems the average angle between the bands is around 57 ± 3°. This is an indication that these features are deformation bands (due to the characteristic angles) [42].

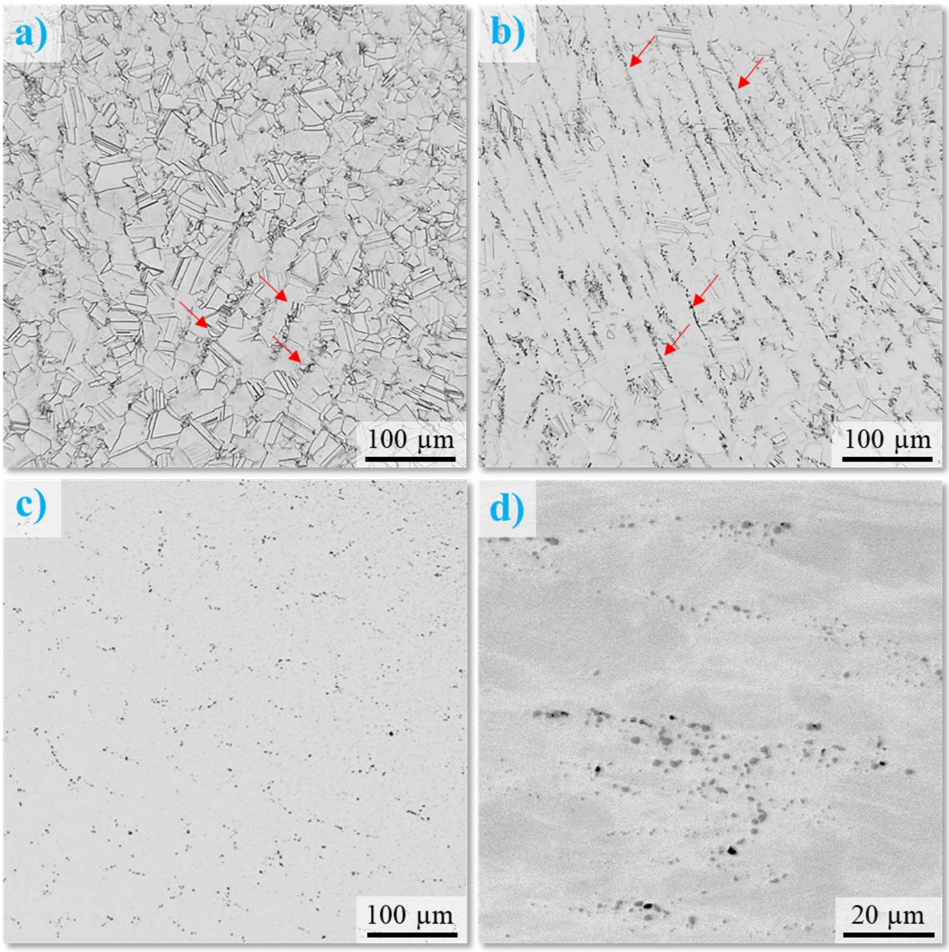

Figure 5.12. Microstructural characterization of the $Cr_{39.6}Co_{30}Ni_{30}C_{0.4}$ samples (a-c) after full TMH and (d) after cold rolling with 50 % thickness reduction. (a-b) are OM micrographs in which banding is seen for the carbide particles in the fcc matrix (as indicated by red arrows). (c) SEM imaging on BSE mode showing a non-banded region of C3. (d) SEM-BSE micrograph for the C4 sample. (a-b) Etched with Kallings N°II. The rolling direction in the images is parallel to the page's width (horizontal, left to right). The same is true for the annealed samples, albeit they are fully recrystallized.

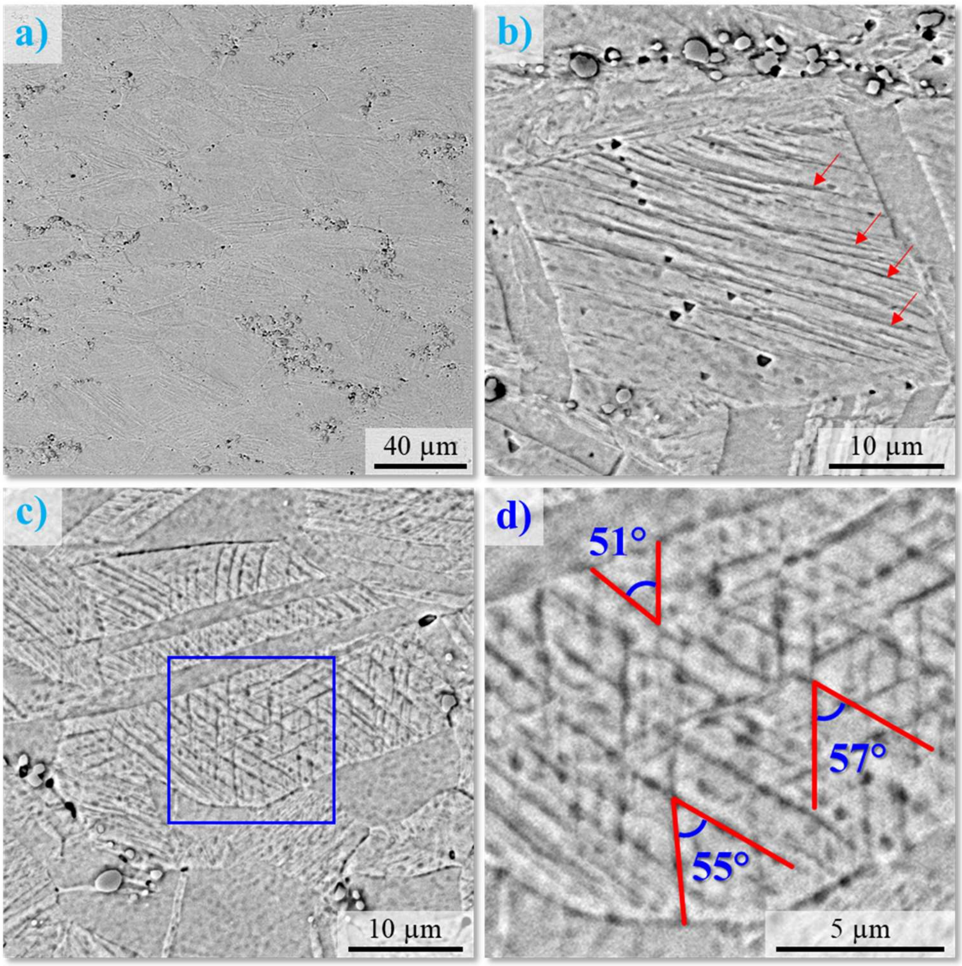

Figure 5.13. SEM-BSE microstructural characterization of the $Cr_{39.6}Co_{30}Ni_{30}C_{0.4}$ sample after CR to 50 % thickness reduction. Deformation bands are indicated by red arrows in (b) and the angle between some bands was measured for (d). Etched with Kallings N°II.

As explained on section 4.4, after CR the materials underwent a solution treatment, at 1195 °C for 1h and 4 h, to dissolve the $M_{23}C_6$ particles. The processing route without the dissolution is discussed on section 7. Figure 5.14a shows that the great majority of carbides were dissolved for $Cr_{39.6}Co_{30}Ni_{30}C_{0.4}$. It seems that the volumetric fraction left is lower than the predicted (0.23 %) by thermodynamic calculations (Figure 5.3). Darker spots observed at Figure 5.14a are (for this sample) generally not pitting corrosion spots. They are oxides formed in the solution treatment and are better visualized at higher magnifications. In the samples' edge, shown in Figure 5.14b, it is possible to see a thick dark grey layer (identified by a white arrow). It was characterized as being composed by different types of chromium-rich oxides and is simply the surface oxidation layer characteristic to high temperature processing [56,57]. The observed compositions ranged from 46 to 49 at.% of Cr and 49 to 53 at.% for O.

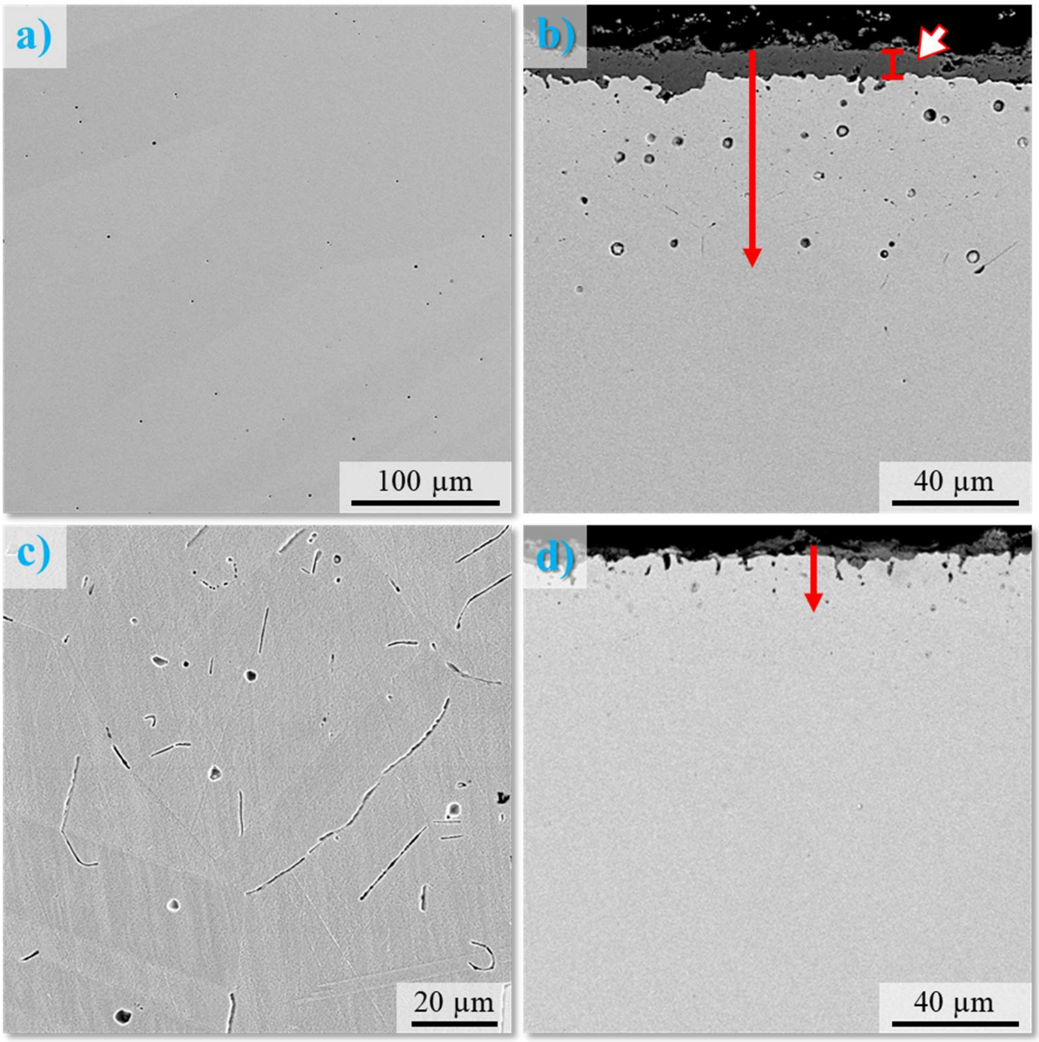

Figure 5.14. SEM-BSE characterization of the $Cr_{39.6}Co_{30}Ni_{30}C_{0.4}$ solution treated samples' microstructures in the longitudinal section. (a-c) 1195 °C for 4h, and (d) 1195 °C for 1h. (a) Black spots are mainly oxides. Micrographs showing the surface chromium oxide (white arrow) and degree of oxygen penetration (red arrow) in the (b) 4 h and (d) 1 h samples. (c) Higher magnification of the edge region, full of particles with different morphologies. (c) Etched with Kallings N°II.

Another interesting phenomenon was observed in the inner part of the samples' edge in Figure 5.14b. Different oxides have formed a second and deeper (in the thickness) layer. In Figure 5.14c, different morphologies can be seen for these second phase particles. The chemical composition and spatial distribution for each microstructure constituent with distinct morphology was evaluated by energy dispersive spectrometry (EDS) microanalysis and is shown in Figures 5.15 and 5.16. It can be observed a high concentration of Al and O, and depletion of Cr, Co and Ni in all images. As such, all second phase particles were detected as aluminum oxides. The excess of aluminum probably came from the raw materials used to manufacture the cast alloys, or from contamination at the arc-melting furnace.

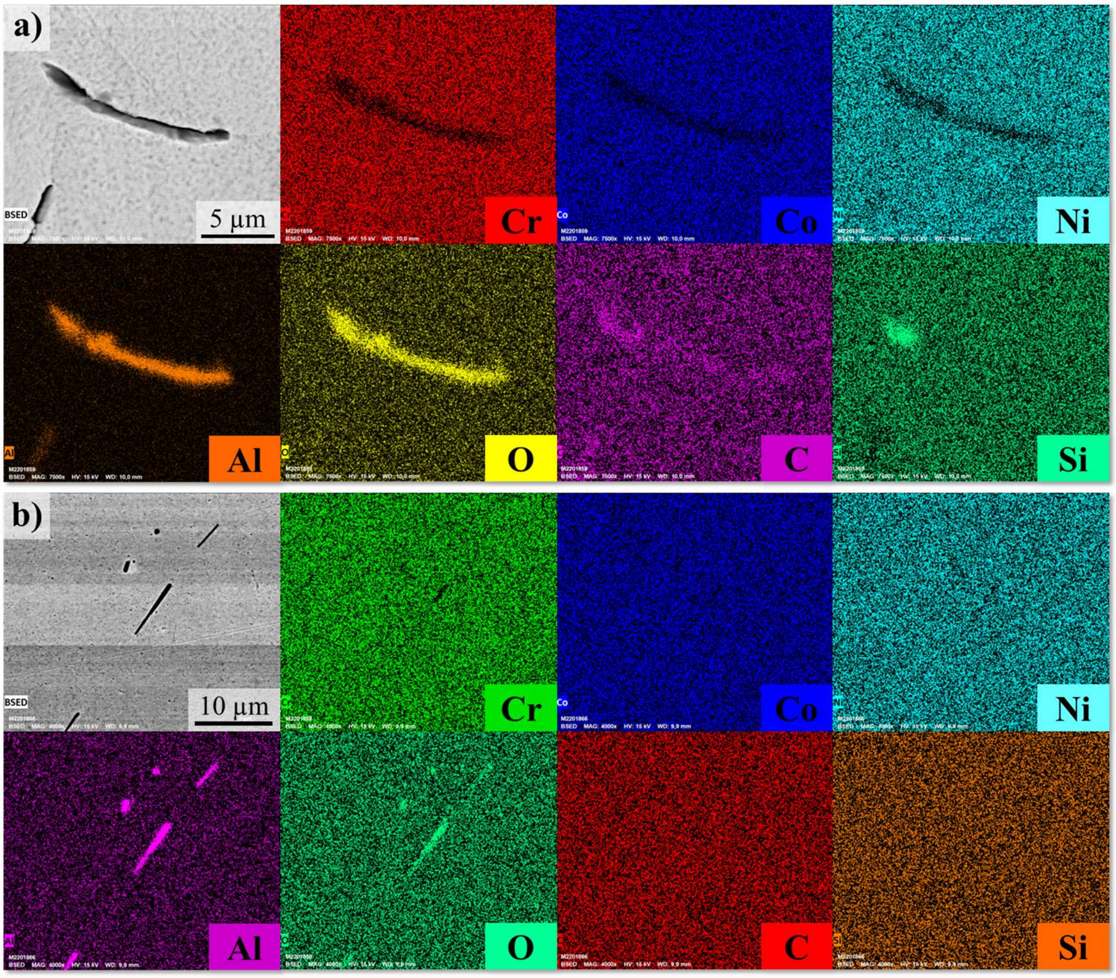

Figure 5.15. Chemical characterization with EDS for the $Cr_{39.6}Co_{30}Ni_{30}C_{0.4}$ sample after solution treatment for 4 h. The spatial distribution of chemical elements maps here are for the different (a and b) elongated particles observed.

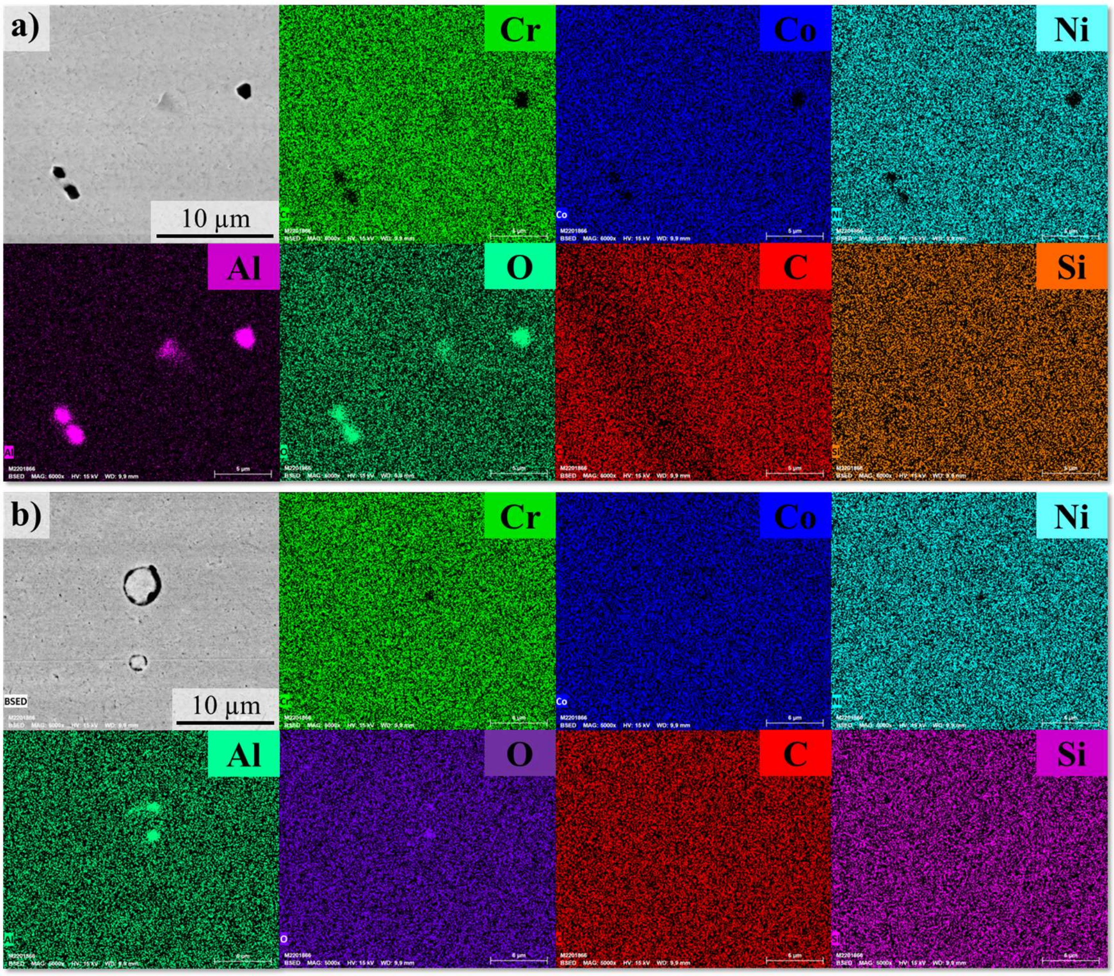

Figure 5.16. Chemical characterization with EDS for the $Cr_{39.6}Co_{30}Ni_{30}C_{0.4}$ sample after solution treatment for 4 h. The spatial distribution of chemical elements maps here are for the different (a and b) round particles observed.

This phenomenon, where the main element of a gaseous oxidant penetrates the alloy's bulk is known as internal oxidation. It is governed by dissolution and diffusion mechanisms [58]. To avoid the high levels of oxidation observed, the solution treatment time was reduced from 4 h to 1h. Figure 5.14.d shows that with the lower exposure time to a high temperature atmosphere, the penetration depth (red arrow) became significantly smaller. Likewise, the surface oxidation was also diminished. Figure 5.17 shows a comparison between the solution treatment times with a full thickness profile for the $Cr_{39.6}Co_{30}Ni_{30}C_{0.4}$ material. Both 4 and 1 h resulted in very similar amounts of carbide dissolution. Nevertheless, the latter showed very few oxides present in all of the samples' bulk, and was chosen for the solution treatment processing route.

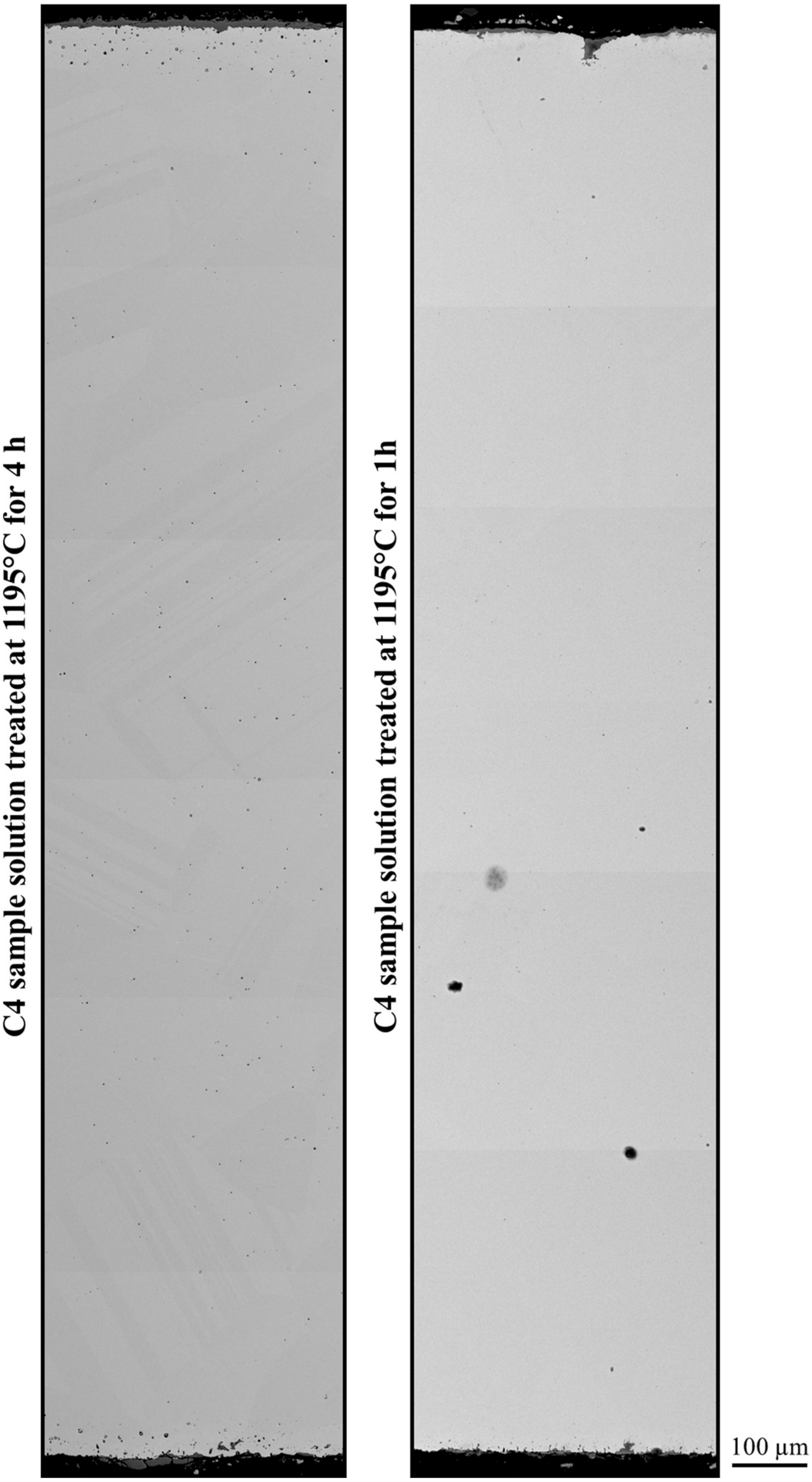

Figure 5.17. In-thickness microstructural profile for the $Cr_{39.6}Co_{30}Ni_{30}C_{0.4}$ samples solution treated for 4 and 1 hours.

The depth of penetration for internal oxidation, $X_{(i)}$, has a parabolic relationship with time (t), as indicated by equation 5.1 [58].

$$X_{(i)}^2 = 2k_p t \tag{5.1}$$

Where k_p is the internal oxidation rate constant. Figure 5.18 shows the depth of penetration versus the square root of oxidation time curves for different materials. k_p is 293 μm^2/s for the $Cr_{39.6}Co_{30}Ni_{30}C_{0.4}$ alloy under a 1195 °C uncontrolled atmosphere. From figure 5.18 it is clear that this rate gets higher with increasing temperatures [56] and the more humid the conditions become [57].

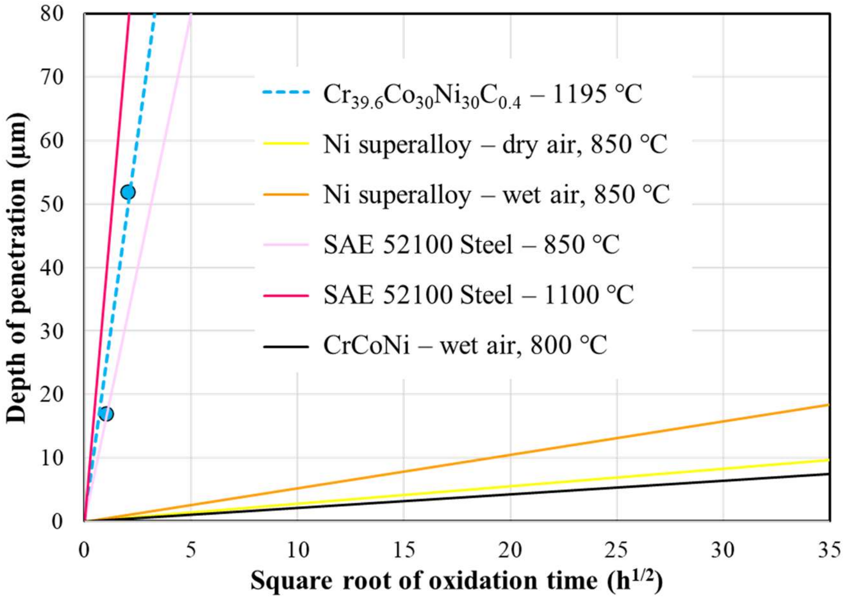

Figure 5.18. Measured internal oxidation kinetics for $Cr_{39.6}Co_{30}Ni_{30}C_{0.4}$ at 1195 °C and for other materials (obtained in literature) at different conditions: ATI 718Plus, which is a Ni-based superalloy [57]. A SAE 52100 steel [56]. And a equiatomic CrCoNi alloy [59].

As far as it is known in this work, there is a lack of studies about internal oxidation of CrCoNi alloys. The equiatomic alloy was shown to have a very high oxidation resistance in dry environments [10]. The measured kp for CrCoNi was much lower (2.3 x 10^{-2} μm^2/h) than the one measured in this work for $Cr_{39.6}Co_{30}Ni_{30}C_{0.4}$ (2.9 x 10^2 μm^2/h). This could be the effect of CD, or simply the experimental conditions were not ideal. Whichever the case, internal oxidation will be more prominent at 1195 °C when compared to the 800 °C. This could be a critical factor for these alloys, since internal oxidation can lead to structural failure [58].

6 SOLUTION TREATMENT ROUTE

As reported in the previous section of this work, the preferred parameters for solution treatment were 1195 °C and 1 h. Although the $Cr_{39.9}Co_{30}Ni_{30}C_{0.1}$ (B) alloys also have carbon, their content of this element is lower just as their dissolution temperature, when compared to $Cr_{39.6}Co_{30}Ni_{30}C_{0.4}$ (C). This is why the chosen conditions for dissolving the $M_{23}C_6$ carbides were with respect only to the C alloys. Nevertheless, the microstructures of the AS and BS samples are shown in Figure 6.1.

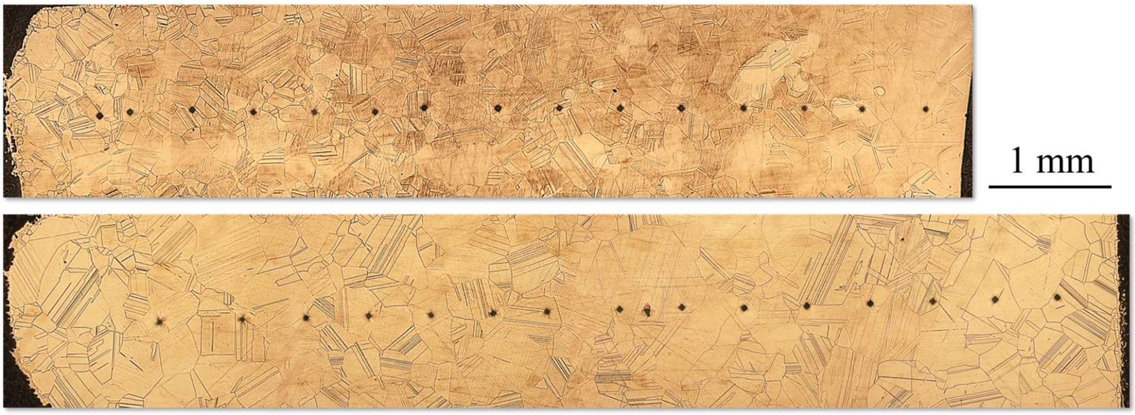

Figure 6.1. Microstructural characterization of the $Cr_{40}Co_{30}Ni_{30}$ (top) and $Cr_{39.9}Co_{30}Ni_{30}C_{0.1}$ (bottom) samples after solution treatment at 1195 °C for 1 h. Etched with Kallings N°II.

6.1 75 % Thickness Reduction Cold Rolling

After solution treatment samples were cold rolled for 75 % thickness reduction. This is equivalent to a true strain of approximately 140 %. The amount of deformation is more severe when compared to the CR before the carbide dissolution (50 % reduction and 70 % true strain). Figure 6.2 shows the microstructure for the ASCR sample. The grains are highly elongated in the rolling direction and show marks perpendicular to their lengths (indicated by red arrows). These features are probably not cracks, since they are found enclosed to each grain. It also does not appear to be deformation bands, since the morphology is very different from what was shown in Figure 5.13.

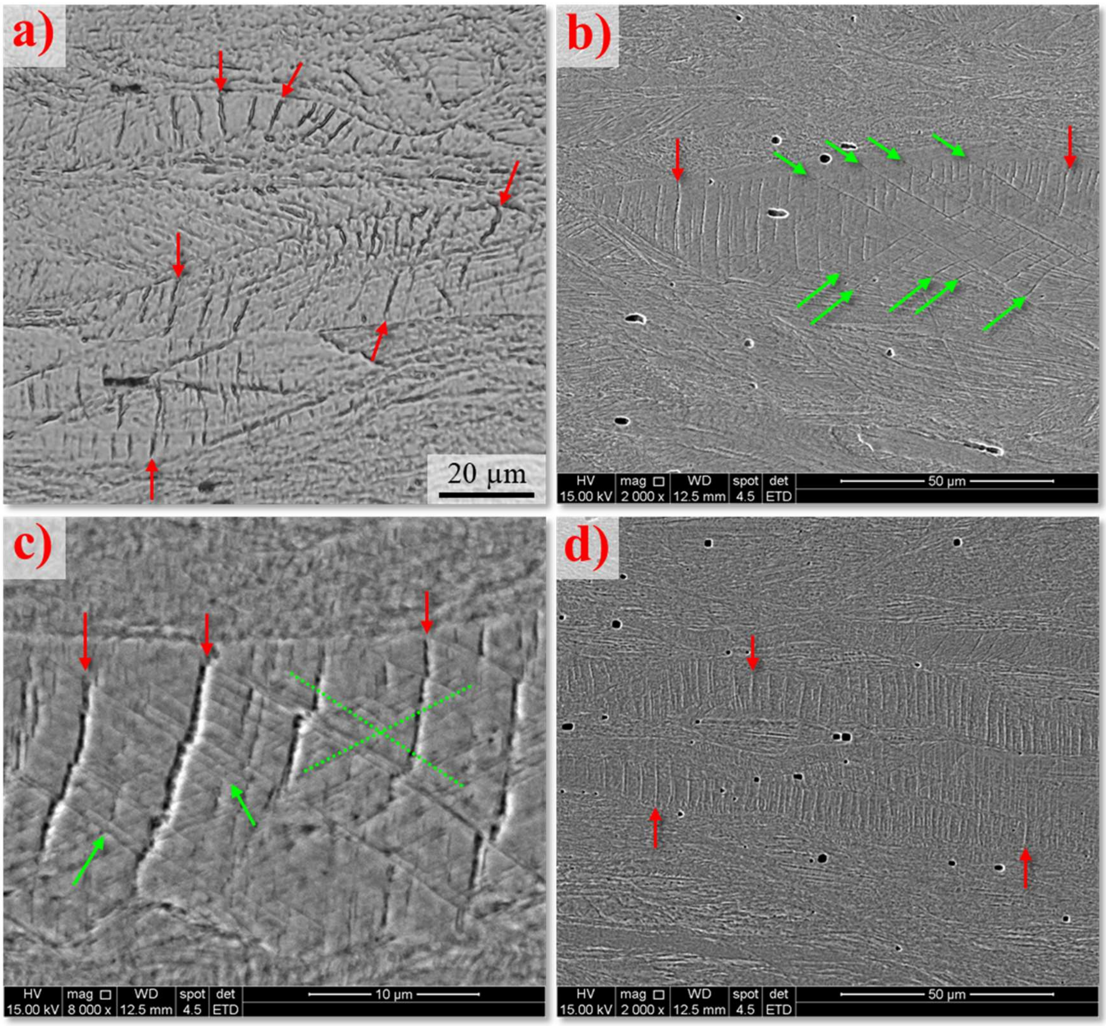

Figure 6.2. Microstructural characterization of the Cr$_{40}$Co$_{30}$Ni$_{30}$ after CR for 75 % thickness reduction. Images were taken with (a) OM at the longitudinal section and with SEM-SE at the (b-c) longitudinal and (d) transversal sections. Red arrows point to the planar features perpendicular to the grains' lengths. Etched with Kallings N°II.

Deformation bands are present in the ASCR sample, as indicated by green arrows and lines. However, they show a different orientation when compared to what is indicated by the red arrows (and approximately 57 °C between themselves). A possibility for the perpendicular features is that they are deformation twins. This would be possible if TWIP has activated to high degrees and is visible even with OM. In Figure 6.2d, at the transversal section, these (allegedly) twining defects have a different aspect, and were observed as protruding to the image plane. These features could also be microcracks [60]. Nevertheless, additional characterization is needed to identify these features. They were not observed for the BSCR (Figure 6.3a) and CSCR (Figures 6.3b-d) samples. However, deformation bands, and likely shear bands as well, are seen in large quantities.

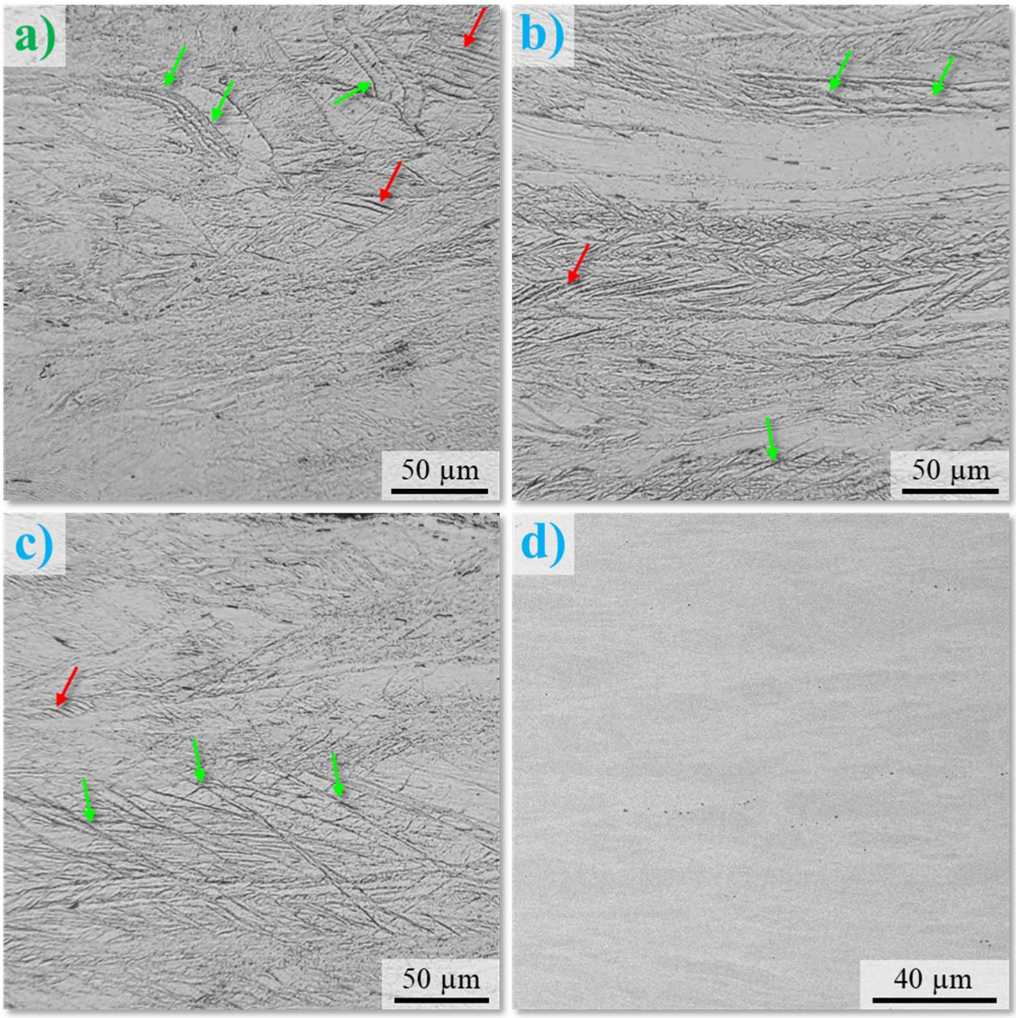

Figure 6.3. Microstructural characterization of the $Cr_{39.9}Co_{30}Ni_{30}C_{0.1}$ (a) and $Cr_{39.6}Co_{30}Ni_{30}C_{0.4}$ (b-d) samples after CR for 75 % thickness reduction. OM (a-c) and SEM-BSE (d) Red and green arrows indicate deformation and shear bands respectively. (a-c) Etched with Kallings N°II.

The curved pattern showed by the elongated grains is an indicative of shear banding (this is seen for ASCR as well, but in lower frequencies). Both features mentioned are a result of plastic deformation heterogeneity, with the latter occurring for higher strains [42]. If the planar features showed at Figure 6.2 are indeed deformation twins, this could indicate that ASCR experienced better strain accommodation. A less localized plastic flow is beneficial for ductility [23]. Figure 6.3d shows that the carbide volume fraction for CSCR did not seem to change when compared to the CS sample. In the work of Moravcik et al.

[61] atom probe tomography analysis indicated that carbon segregates preferentially to grain boundaries in a CrCoNi equiatomic alloy.

6.2 Solution Treatment Route – Annealing

After ST and CR, the alloys were annealed at different times (0.17, 0.5, 4, 10 and 30 h) and temperatures (900 and 1100 °C) to study Hall-Petch behavior and grain growth kinetics. For B and C samples it is important to keep in mind that most of the carbon content is dissolved in a supersaturated state and should precipitate during annealing if the conditions are appropriate. As such, the annealing processing can also be seen as a precipitation treatment.

Starting with the 0.17 h (10 min) and 900 °C heat treatment, the microstructure for the CS-0.17h900 sample is shown in Figures 6.4 and 6.5. From the SEM images, in secondary electron (SE) detection mode, it is clear that recrystallization was not fully achieved. Although some recrystallized grains (proved by their morphology and the presence of annealing twins) can be seen (blue arrows), a reasonable amount of shear/deformation bands are still present (green arrows). Not only that, but precipitation seems to have widely occurred throughout the sample. Virtually all white dots observed are $M_{23}C_6$ particles. This means that the kinetics for precipitation is faster than for recrystallization. The carbide particles being present before recrystallization is advantageous because they will act as barriers to grain boundary migration, retarding the annealing phenomena and resulting in finer grain size distributions.

From figure 6.4b it is possible to observe that a very fine and dispersed distribution of carbides was established after precipitation. No single $M_{23}C_6$ particle larger than 1 μm was detected, and there is a plentiful fraction of precipitates that have diameters in the range of tens of nanometers. This is very different when compared to the distribution after TMH (Figure 5.10). In Figure 6.4b it is also possible to see that deformation bands were a preferential nucleation site for the carbides, which is expected [42].

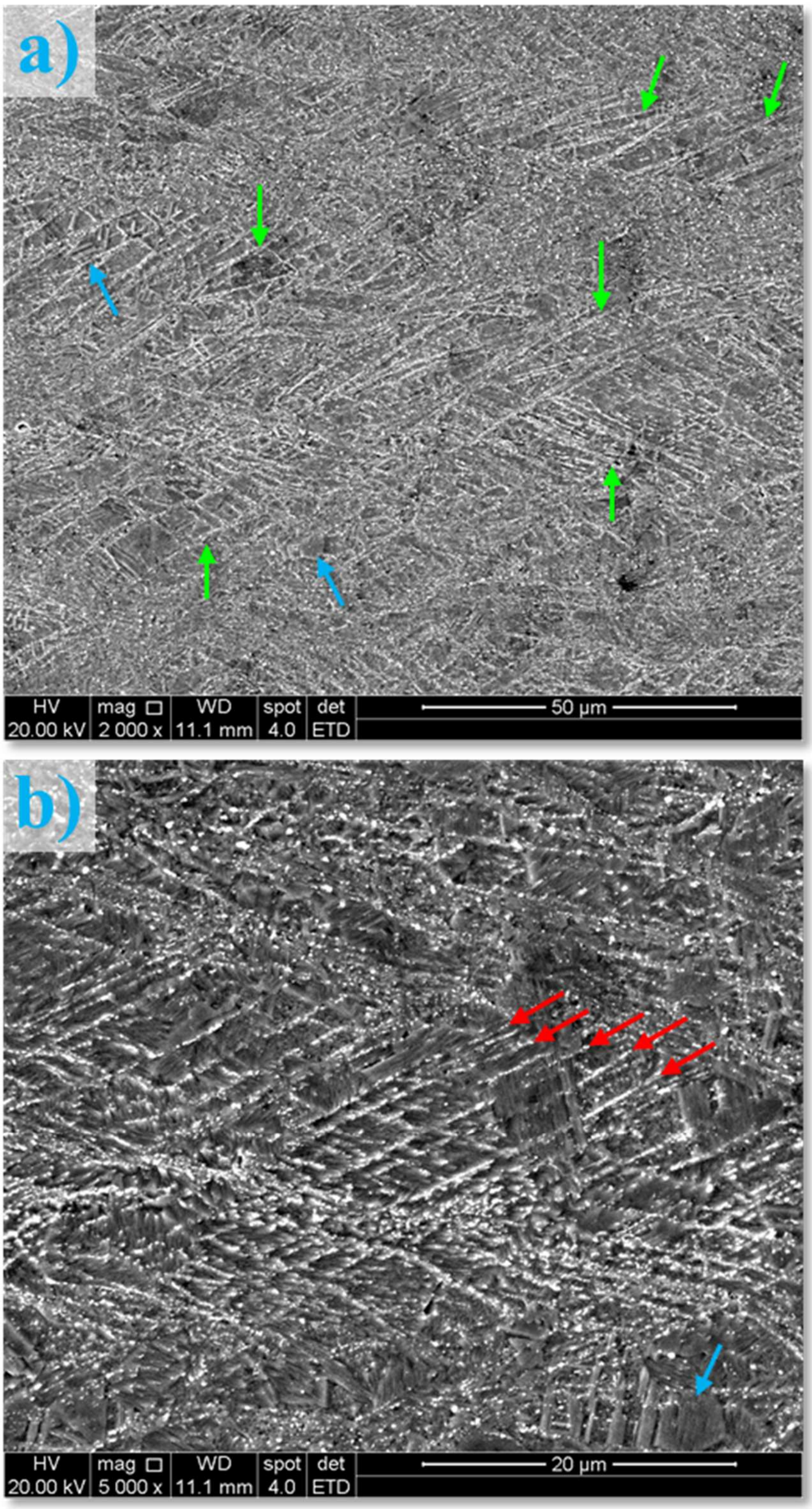

Figure 6.4. SEM-SE characterization of the CS-0.17h900 sample. Blue arrows point to recrystallized grains. In (a), non-recrystallized regions are exemplified by green arrows. In (b), red arrows indicate several parallel deformation bands with a high concentration of second-phase particles. Etched with Kallings N°II.

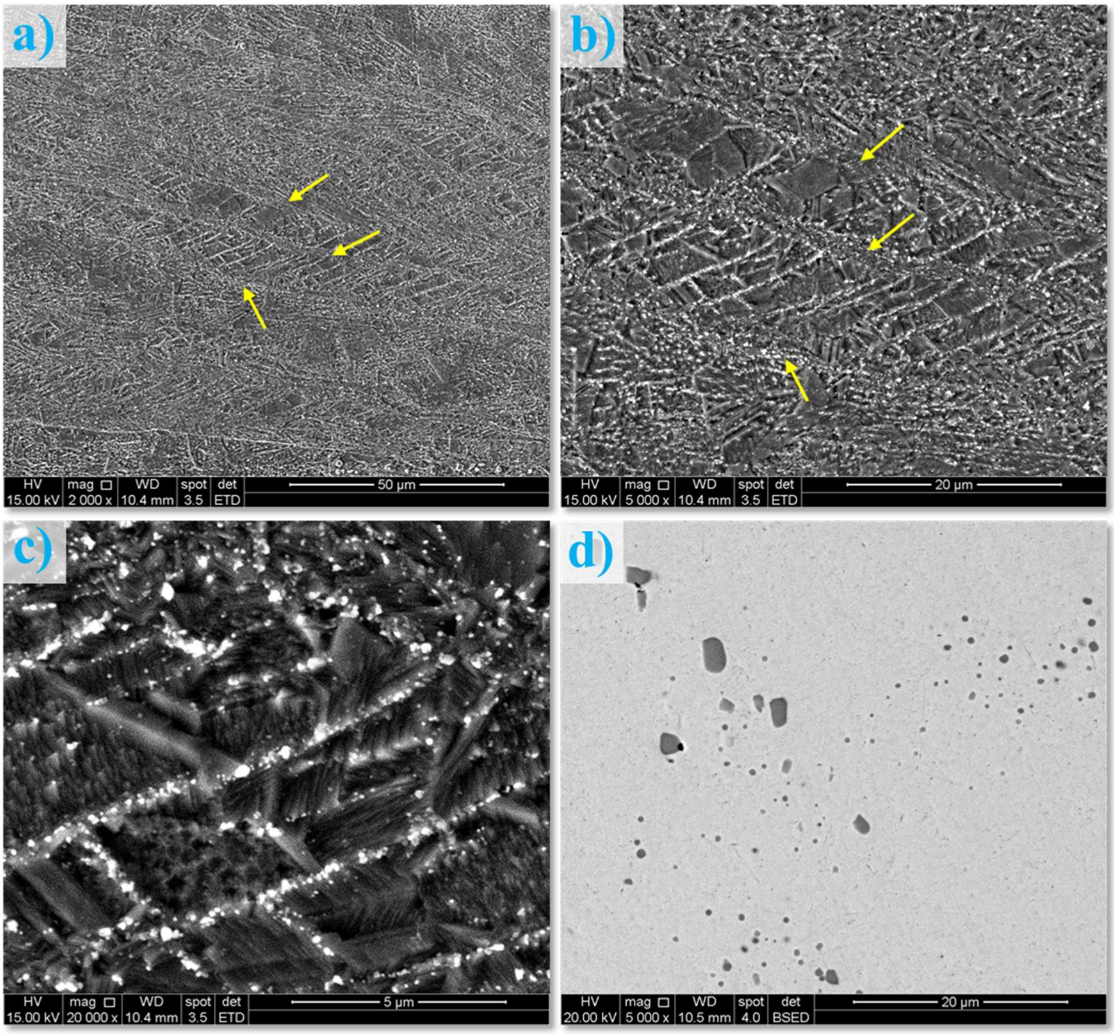

Figure 6.5. SEM-SE characterization of the (a-c) CS-0.17h900 sample at different magnifications. (a-c) are different magnifications of the same region. For comparison purposes, an example of the carbide dispersion in (d) C3 is represented. (a-c) Etched with Kallings N°II.

Figure 6.5 gives, for the CS-0.17h900 sample, a clear example of deformed and elongated grains with a high concentration of particles nucleated in deformation bands. Yellow arrows point to thick layers of what presumably are these grain boundaries. By comparing CS-0.17h900 (Figure 6.4b) to C3 (Figure 6.5d), at a same magnification, there is an obvious refinement of the second-phase particles dispersion (for the former). Even with lower amounts of carbon-doping, the $Cr_{39.9}Co_{30}Ni_{30}C_{0.1}$ alloy also showed precipitation before the end of recrystallization. This was observed for the microstructure of the BS-0.17h900 sample, showed in Figure 6.6, due to the presence of particles arranged linearly. The $Cr_{39.9}Co_{30}Ni_{30}C_{0.1}$ alloy showed this behavior even with a weaker driving force (less carbon content in a supersaturated state) than $Cr_{39.6}Co_{30}Ni_{30}C_{0.4}$. It is also interesting to observe that after annealing at 900 °C for 10 minutes material B was already fully recrystallized, which was not the case for C.

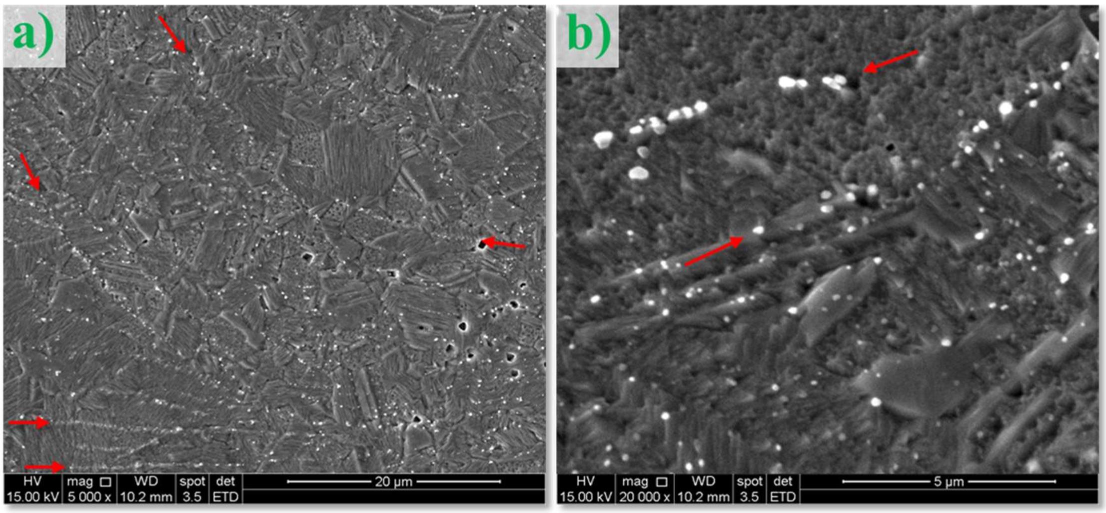

Figure 6.6. SEM-SE characterization of the BS-0.17h900 sample. Red arrows indicate particles there were nucleated in former deformation bands (linear arrangement). Etched with Kallings N°II.

When the annealing time is extended from 10 to 30 minutes (0.5 h), as seen in Figures 6.7a-b for the CS-0.5h900 sample, the carbide particles become slightly coarser due to coalescence and the microstructure is fully recrystallized. Nevertheless, the overall distribution remained as a fine and homogeneous dispersion. This seems even more the case when compared to the CS-0.17h900 sample, since the majority of particles arranged in the deformation bands were redistributed. Some carbides are still located where these features were present in the CR microstructure (red arrows in Figure 6.7). Besides coalescence, a mechanism that could have operated to promote carbide redistribution is the dissolution of particles followed by re-precipitation during the passage of boundaries [42].

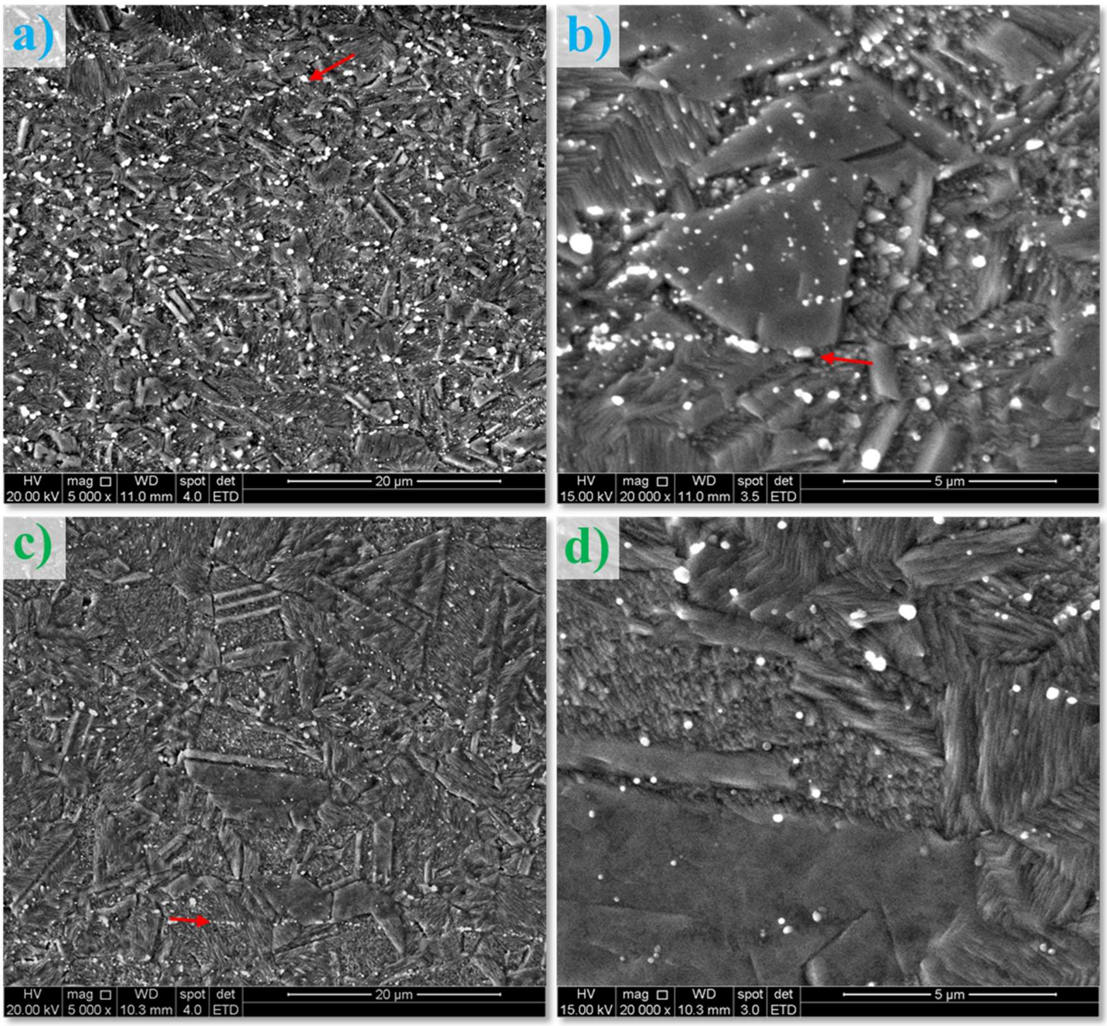

Figure 6.7. SEM-SE characterization of the (a-b) $Cr_{39.6}Co_{30}Ni_{30}C_{0.4}$ and (c-d) $Cr_{39.9}Co_{30}Ni_{30}C_{0.1}$ alloys after annealing at 900 °C for 30 minutes (0.5 h). Red arrows indicate particles there were nucleated in former deformation bands (linear arrangement). Etched with Kallings N°II.

The microstructure for BS-0.5h900 is shown at Figure 6.7 (c-d) and is also fully recrystallized. The dispersion is very similar to that of CS-0.5h900 except by the number of particles. This is expected since at 900 °C, in thermodynamic equilibrium, the carbides' volume fraction should be 0.28 and 1.37 % for $Cr_{39.9}Co_{30}Ni_{30}C_{0.1}$ and $Cr_{39.6}Co_{30}Ni_{30}C_{0.4}$ respectively. To better understand the carbide distribution in the fully recrystallized matrix, TEM analysis was carried out for the CS-0.5h900 sample. The results are shown at Figures 6.8 and 6.9. Just as observed by SEM, the carbides are mostly sub-micrometric, with the bigger ones located grain boundaries and triple points. Those situated in the bulk seem to have average sizes smaller than 100 nm. Dislocations and very small (< 1 µm) grains can also be seen in Figure 6.8.

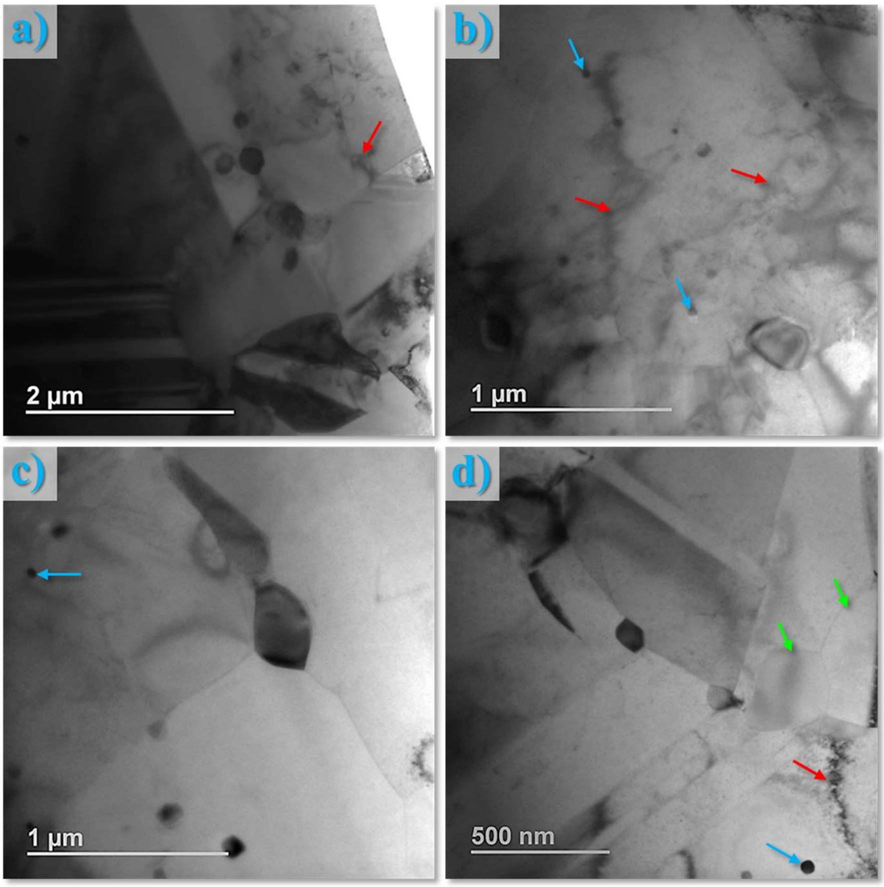

Figure 6.8. Bright Field TEM characterization at different magnifications of the $Cr_{39.6}Co_{30}Ni_{30}C_{0.4}$ alloy after annealing at 900 °C for 30 minutes (0.5 h). Red, green and blue arrows point to examples of dislocations, sub-micrometric grains and ultra-fine $M_{23}C_6$ particles, respectively.

In Figure 6.8c the Smith-Zener drag can be seen as the larger carbide is pinning a GB (which is curved in the particle's vicinity). The carbide dispersion could have been mostly formed before the start of annealing recrystallization. If so, they could have gotten coarser after pinning the GBs. Alternatively, Carbides concentrated in triple points may suggest that recrystallization occurred simultaneously with precipitation (to what extent is unknow).

In Figure 6.9 a peculiar phenomenon can be observed. After being pinned by a $M_{23}C_6$ particle, a GB changed direction abruptly (roughly 90°). This could possibly be a mechanism to ease its migration. Several lines are seen parallel to the same boundary, in a manner similar to dislocation pile-up, which may be the case. Differently than a dislocation, an interface between two grains (i.e., GB) is an impassable barrier. This means the latter cannot disentangle from an incoherent pinning particle through Orowan's bowing mechanism [23,42]. A hypothesis for Figure 6.9 is: the grain boundary pinned by the $M_{23}C_6$ particle (largest one in the image) bended itself as a mean to continue the grain growth. This is indicated by the red arrow, and the GG direction seems to be to the "southeast" of the figure. Additionally, it can be said that the pinning carbide is incoherent since it would have been easier for the GB to have cut through the coherent particle.

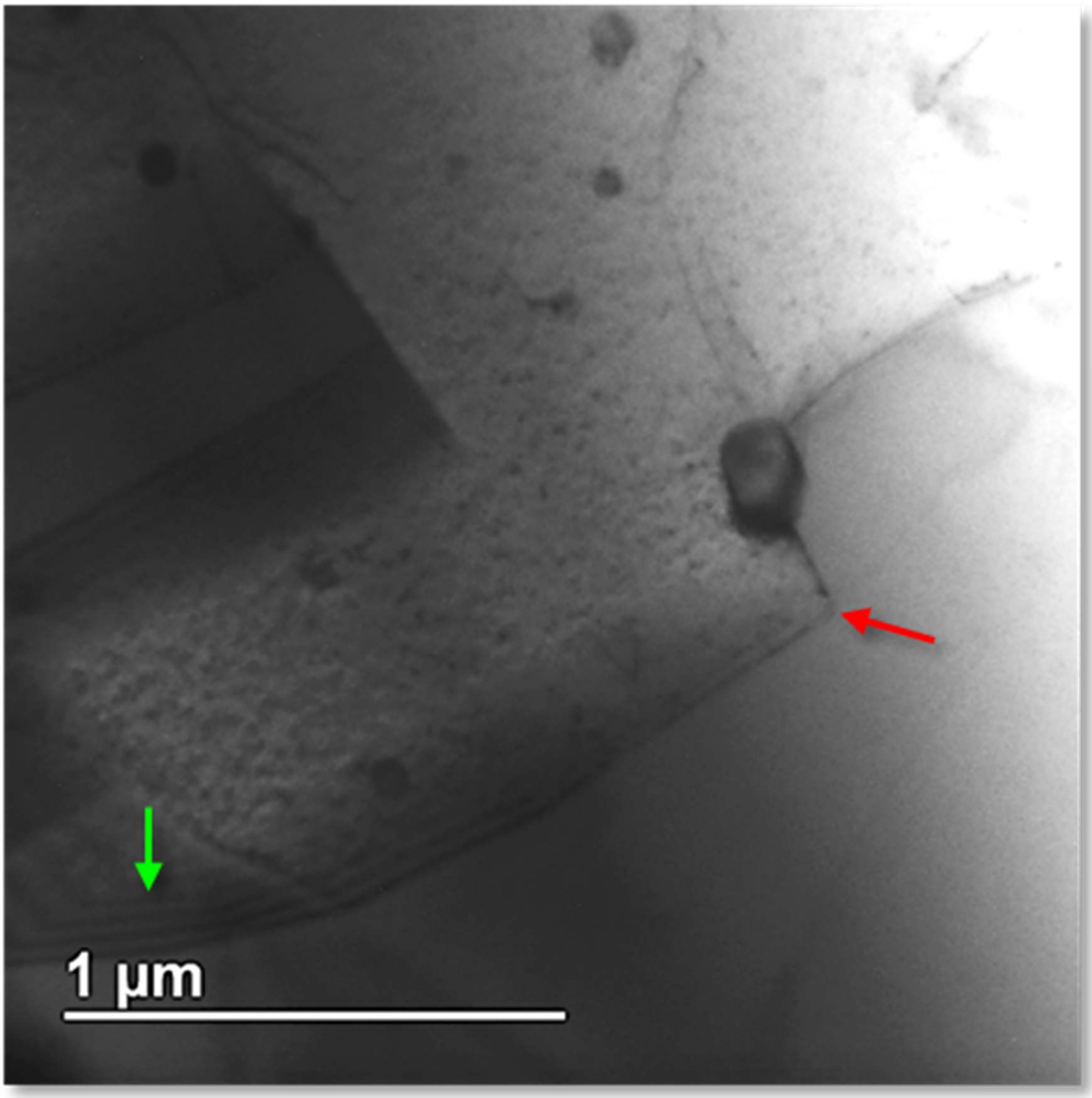

Figure 6.9. Bright Field TEM characterization of the $Cr_{39.6}Co_{30}Ni_{30}C_{0.4}$ alloy after annealing at 900 °C for 30 minutes (0.5 h). An abrupt change in direction for a pinned grain boundary is indicated by the red arrow. Fringes (green arrow) are TEM imaging features often associated with grain boundaries [62].

Differential Scanning Calorimetry (DSC) analysis was carried out for the CS-0.5h900 sample from 25 to 1200 °C with a heating rate of 10 °C/min. The results are shown in Figure 6.10. At 560 °C a wide exothermic peak appeared. It can be due to precipitation of the carbon content that was still in solid solution (at least 0.06 at.% in Figure 4.1). From 800 °C onwards, the heat flows increased (albeit some minor peaks were observed) until reaching a maximum at 1200 °C and then the experiment was over. The carbide dissolution could explain this behavior, since the carbon solvus curve goes from fully precipitated (around 600 to 700 °C) to full solid solution at roughly 1250 °C.

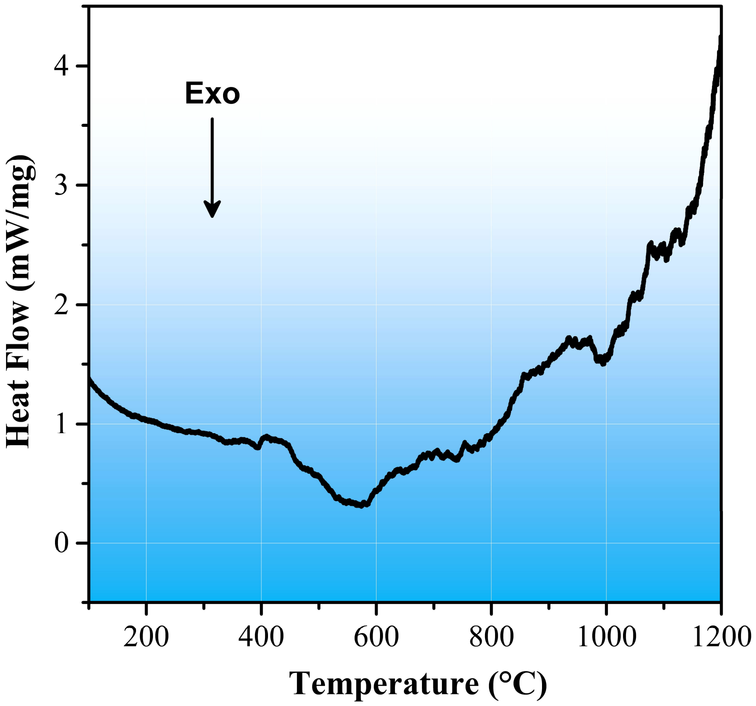

Figure 6.10. Differential scanning calorimetry analysis for the CS-0.5h900 sample. Testing made with a heating rate of 10 °C/min. Exothermal reactions are negative in the heat flow.

When the annealing time was increased from 0.5 h to 4 h (at 900 °C), not only did the carbides got coarser, but regions with almost no precipitation could be observed. This is shown in Figure 6.11 in the form of narrow bands that stretch across long distances and are oriented parallel to the rolling direction. In Figure 6.12 the microstructures for BS-4h900 and CS-4h900 are shown side by side (6.12a and 6.12b respectively). The former's microstructure also has regions with $M_{23}C_6$ depletion. They seem wider than for the $Cr_{39.6}Co_{30}Ni_{30}C_{0.4}$ alloy probably due to the lower volume fraction of the first one.

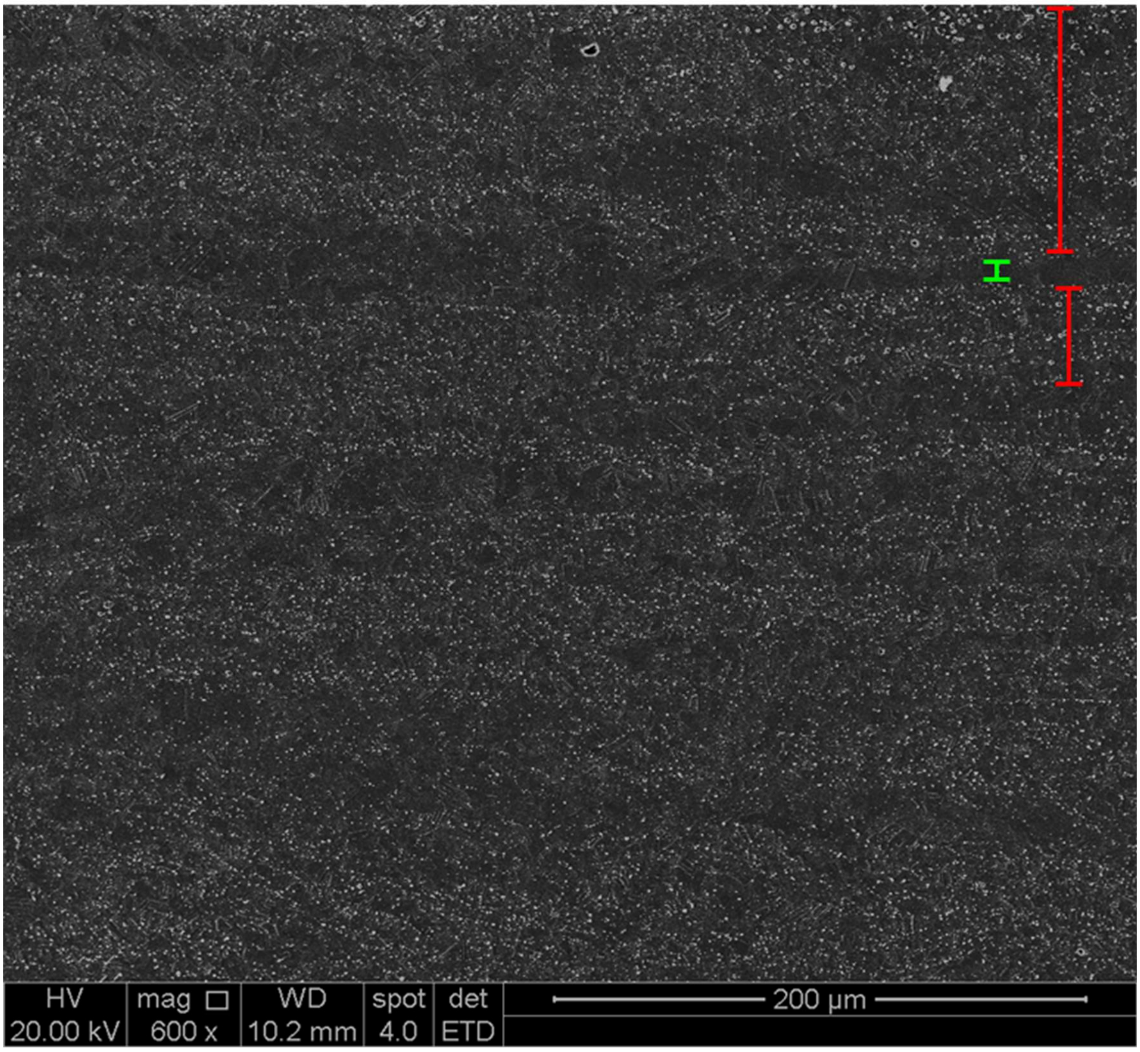

Figure 6.11. SEM-SE characterization of the precipitation distribution for the $Cr_{39.6}Co_{30}Ni_{30}C_{0.4}$ alloy after annealing at 900 °C for 4 hours. Image contrast was raised to highlight second-phase particles. A carbide depletion banded region width is depicted by a green bar. Red bars exemplify near random dispersion of particles. Etched with Kallings N°II.

With an even longer annealing time of 30 hours, the carbide depletion zones in the $Cr_{39.6}Co_{30}Ni_{30}C_{0.4}$ alloy did not seem to increase significantly (Figure 6.12c). However, the $M_{23}C_6$ average particle size did. In Figure 6.12d it could be better seen that for CS-30h900 there is a considerable number of particles with sizes larger than 1 μm.

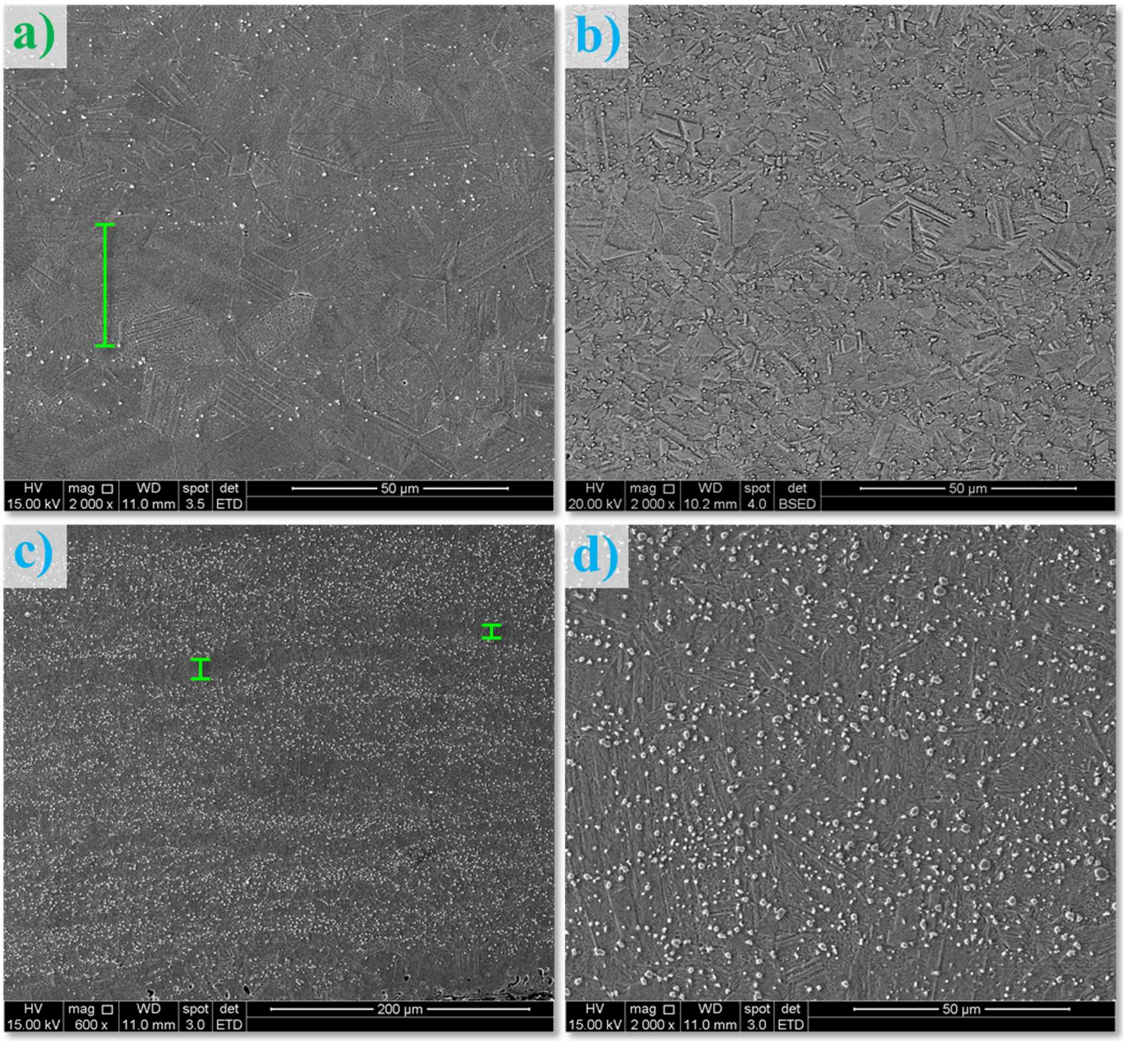

Figure 6.12. SEM-SE characterization of the (a) BS-4h900 sample and for the $Cr_{39.6}Co_{30}Ni_{30}C_{0.4}$ alloy after annealing at 900 °C for 4 hours (b) and 30 h (c-d). Carbide depletion banded regions widths are depicted by green bars. Etched with Kallings N°II.

Figure 6.13 depicts the microstructure for the AS-30h900 sample where second-phase particles were detected. Black features are probably pitting corrosion spots originated after etching. Through EDS punctual analyses it was observed that most of the particles are rich in Cr. Their average composition is presented in Table 6.1. From Figure 4.3, a volume fraction of 1.3 % of sigma phase is predicted at 900 °C for equilibrium. The calculated expected composition is also shown at Table. Chromium and Nickel contents for the observed particles are similar with those of the sigma phase given by thermodynamic analysis. The value for Cobalt is outside the error range. This could mean the second-phases seen in Figure 6.13 were a consequence of contamination.

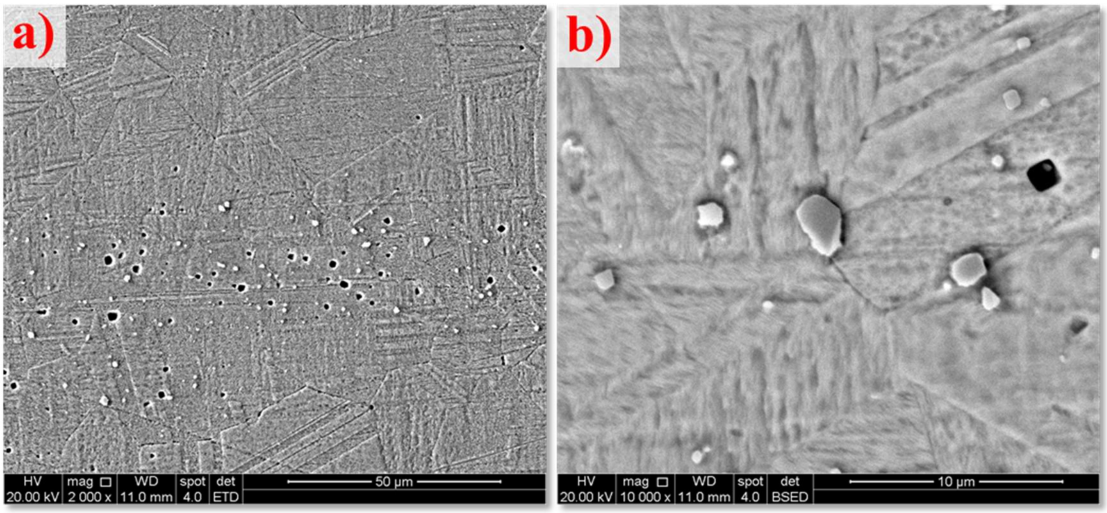

Figure 6.13. SEM characterization of the $Cr_{40}Co_{30}Ni_{30}$ alloy after annealing at 900 °C for 30 hours with (a) SEM-SE and (b) OM. Etched with Kallings N°II.

Table 6.1. EDS micro-analysis of the particles observed in the AS-30h900 sample.

Composition (at.%)	Cr	Co	Ni
Observed (unknown)	64 ± 16	17 ± 8	19 ± 8
Expected (sigma)	57	30	13

Outside of contamination, the analyses shown in Table 6.1 indicate that there was precipitation of sigma phase after annealing at 900 °C for 30 h. Zhang M et al. [49] annealed a CrCoNi alloy for 240 h at different temperatures (600, 700, 800, 900 and 1000 °C) and did not report any sigma phase formation. Likewise, most studies with the equiatomic alloy do not appear to show this phase when it is thermodynamically predicted [10,37,40].

For the $Cr_{40}Co_{30}Ni_{30}$ and $Cr_{39.6}Co_{30}Ni_{30}C_{0.4}$ alloys, heat treatments at 1100 °C (after the CR processing with 75 % thickness reduction) were carried out, for 0.5 and 4 h, to study the effects of temperature on the annealing (and consequently on the grain growth kinetics). Figure 6.15 shows the obtained microstructures. At low magnifications it is possible to see that the carbide dispersion has formed bands alternating between concentrated and depleted regions. This is the same phenomenon observed for CS-4h900 at Figure 6.11, albeit in larger scale (thicker depleted bands). And, CS-4h1100 shows (Figure 6.12c) the largest regions with seemingly no particles.

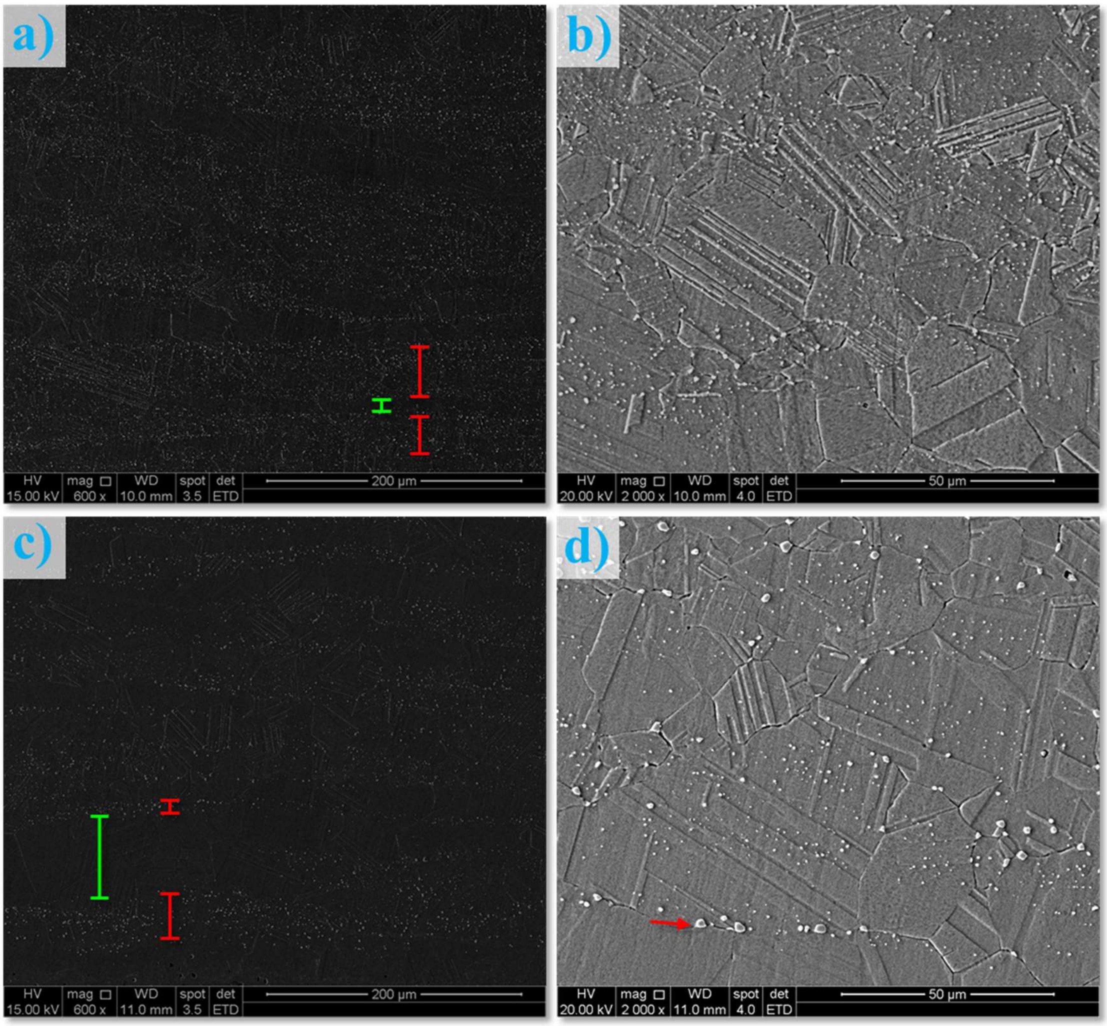

Figure 6.15. SEM-SE characterization of the $Cr_{39.6}Co_{30}Ni_{30}C_{0.4}$ alloy after annealing at 1100 °C for (a-b) 30 minutes and (c-d) 4 hours. At 600x magnification, the images contrast was highly raised to help visualize the carbides distribution. Carbide depletion banded regions widths are depicted by green bars. Red bars exemplify near random dispersion of particles. Red arrows indicate particles there were nucleated in former deformation bands. Etched with Kallings N°II.

It is not possible, with the current data, to say if the precipitation at 1100 °C occurred similarly to what was observed for the 900 °C annealing samples (i.e., before/concurrently to recrystallization). However, what appears to be particles oriented where used to be a deformation band is seen in Figure 6.15. Additionally, the banding is parallel to the rolling direction. This was not the case for the C3 alloy (Figure 5.12), in which the bands change orientation throughout the samples' length. And it should be reinforced that the carbides found in C3's microstructure were originally precipitated in the grain boundaries, i.e., heterogeneously (Figure 5.2). Higher magnifications of the 1100 °C samples are shown in Figure 6.16

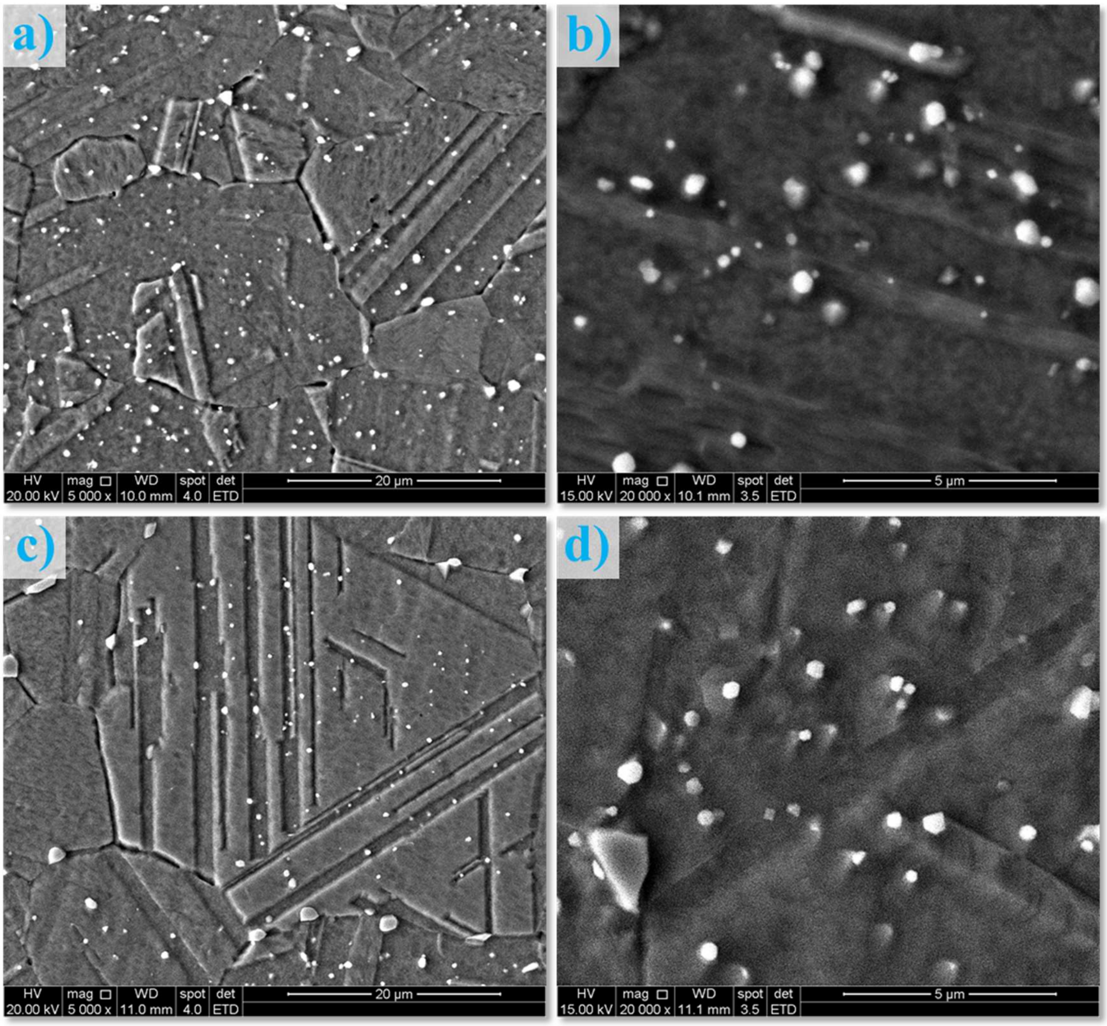

Figure 6.16. SEM-SE characterization of the $Cr_{39.6}Co_{30}Ni_{30}C_{0.4}$ alloy after annealing at 1100 °C for (a-b) 30 minutes and (c-d) 4 hours. Etched with Kallings N°II.

Just like at 900 °C the carbide distribution is located mainly in the samples' bulk, with few larger particles located at the grain boundaries. For $Cr_{39.6}Co_{30}Ni_{30}C_{0.4}$, the volume fraction in equilibrium at 1100 °C is roughly half of the predicted at 900 °C. This could explain why the particle size for both the CS-0.5h1100 and CS-4h1100 samples is similar to the observed for CS-4h900. However, it should be note that CS-4h1100 is the only out of the three to show a significative number of particles with more than 1 μm.

The average grain sizes for the different conditions (in the processing route discussed in this section) were analyzed. The results are shown in Figure 6.17. It is clear the effect of carbon-doping in refining the microstructures, since all C samples showed lower values when compared to materials A and B. The only exception was for the samples that underwent solution treatment at 1195 °C for 1 h. More will be discussed further in the text.

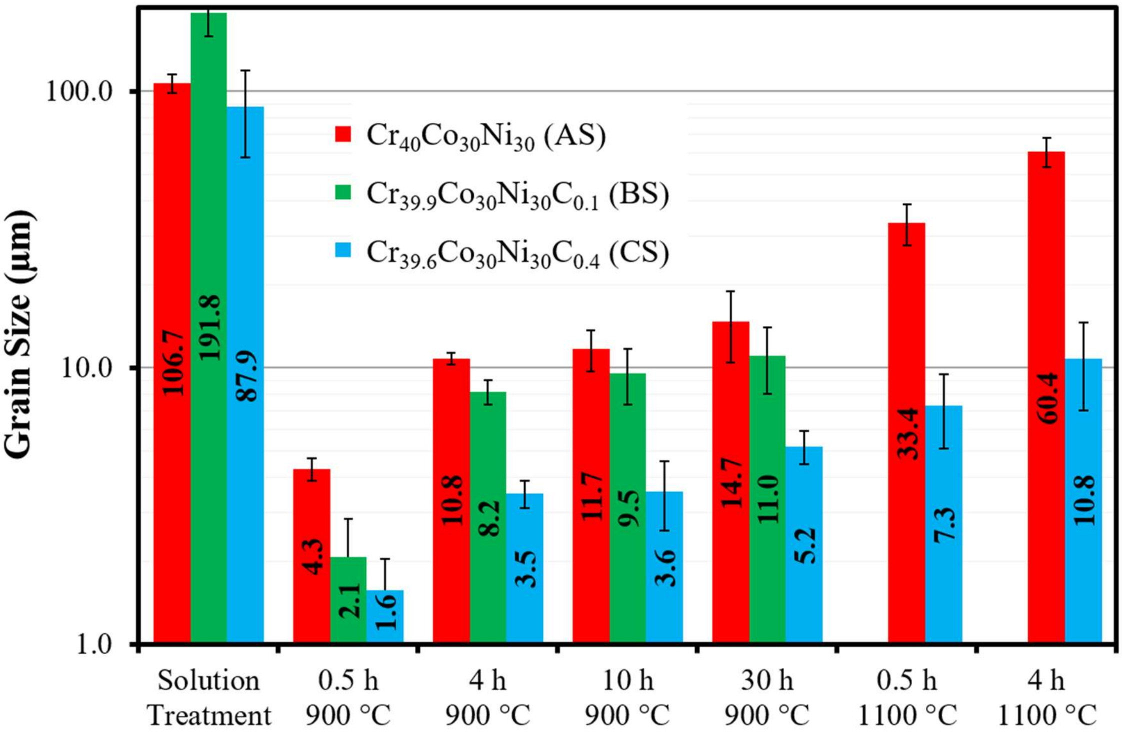

Figure 6.17. Average grain size value (intercept length) for the different conditions at the solution treatment processing route, in logarithmic scale. Twins were not considered in the measurements.

The microstructural evolution observed for the $Cr_{40}Co_{30}Ni_{30}$ and $Cr_{39.6}Co_{30}Ni_{30}C_{0.4}$ alloys is the solution treatment route is summarized in Figure 6.18. The image should help visualize the changes in the carbide distribution (for the C samples) and of grain sizes (for the A samples). In Figures 6.17 and 6.18 it is possible to observe that the grain sizes got larger as the annealing time was longer. Likewise, these values increased when the temperature was raised from 900 to 1100 °C. The observations made are all expected, since grain boundary mobility is favored at higher temperatures, and since grain size during grain growth (GG) is a function of time [23,42]. In fact, the relationship between these two variables is given by equation 6.1 [23,42].

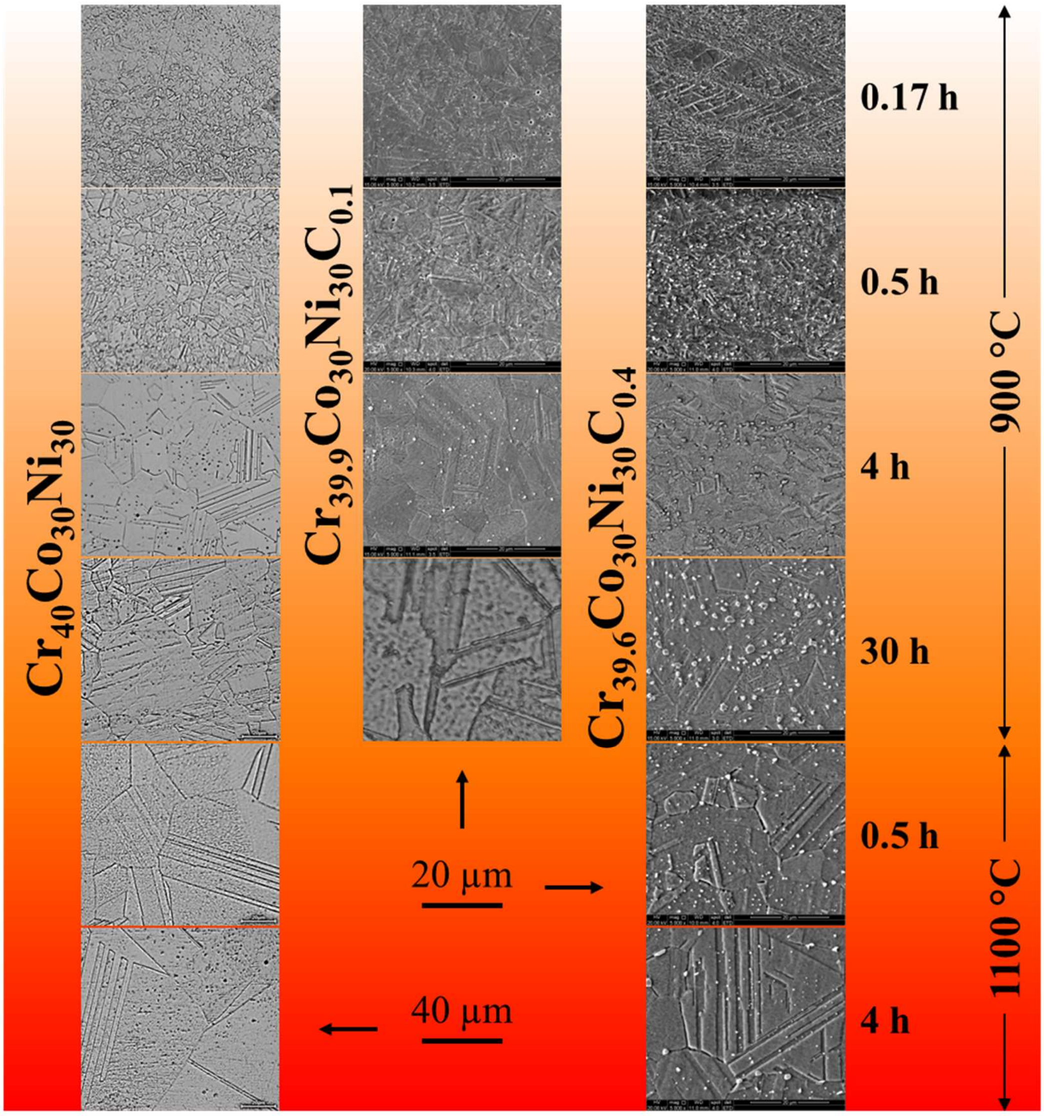

Figure 6.18. Microstructural evolution of the $Cr_{40}Co_{30}Ni_{30}$, $Cr_{39.6}Co_{30}Ni_{30}C_{0.4}$ and $Cr_{39.6}Co_{30}Ni_{30}C_{0.4}$ alloys in the solution treatment processing route after different annealing conditions.

$$D^{1/n} - l_0^{1/n} = K \cdot t \tag{6.1}$$

Where D is the average grain size after grain growth, n is the GG exponent, K is a constant that follows an Arrhenius relationship (increases with temperature) and t is the time since the start of GG. l_0 is the average grain size at the start of grain growth (i.e., at the end of recrystallization). Since l_0 is considerably smaller than D, equation 6.1 can be re-written as [23,42]:

$$D = A \cdot t^{n} \tag{6.2}$$

Where A is simply K^n. If one should take the natural logarithm of both sides of the equation, a linear relationship can be obtained, such that:

$$\ln(D) = \ln(A) + n \cdot ln(t) \tag{6.3}$$

The GG exponent will then be the linear slope and ln(A) the intercept. As such, the equation described above was used with the data given at Figure 6.17, to obtain the grain growth parameters. Figure 6.19 shows the observation points for each material and their respective fitted linear equations.

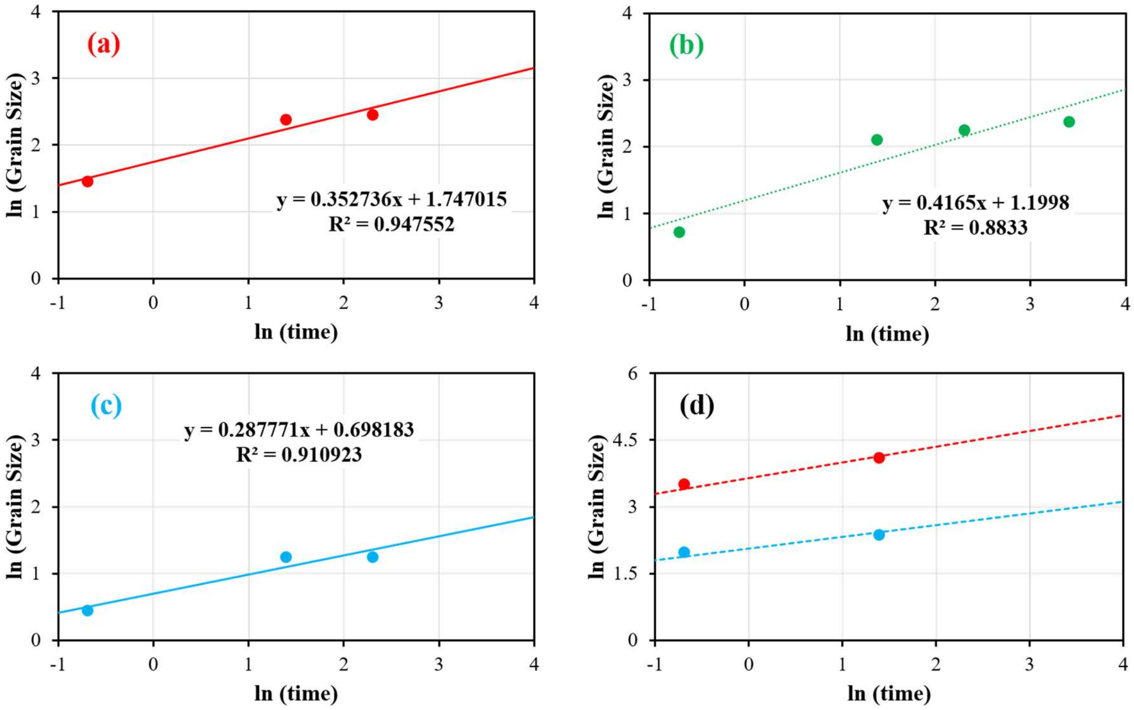

Figure 6.19. Linearized grain growth curves for the (a) $Cr_{40}Co_{30}Ni_{30}$, (b) $Cr_{39.9}Co_{30}Ni_{30}C_{0.1}$ and (c) $Cr_{39.6}Co_{30}Ni_{30}C_{0.4}$ alloys annealed at 900 °C in the solution treatment processing route. An extrapolation was made for the AS (red) and CS (blue) alloys annealed at 1100 °C and is shown in (d).

The experimental datum points seem to fit well ($R^2 > 0.9$) for $Cr_{40}Co_{30}Ni_{30}$ and $Cr_{39.6}Co_{30}Ni_{30}C_{0.4}$. It must be noted that the average grain size for AS-30h900 was not used due to the second-phase formation observed by SEM analysis (Figure 6.14). The linear fit could not be made for the samples annealed at 1100 °C because only two experimental conditions were studied. Nevertheless, considering that n does not change significantly from 900 to 1100 °C, the values of A (and K) for AS and CS were estimated through non-linear fitting with equation 5.3. With A and n, the natural logarithm curves were plotted and are shown in Figure 6.19d. It can be said that for both alloys, the extrapolation and fitting were well succeeded for the 1100 °C annealing samples. The value of n was highest (0.417) for the $Cr_{39.9}Co_{30}Ni_{30}C_{0.1}$ alloy. All the calculated GG parameters and respective correlation coefficients are presented in Table 6.2.

Table 6.2. Grain growth parameters obtained for AS, BS and CS

Material	Temperature (°C)	n	K	A	R^2
$Cr_{40}Co_{30}Ni_{30}$	**900**	0.353	149	5.8	0.948
	1100		30312	38.1	0.957
$Cr_{39.9}Co_{30}Ni_{30}C_{0.1}$	**900**	0.417	18	3.3	0.883
$Cr_{39.6}Co_{30}Ni_{30}C_{0.4}$	**900**	0.262	17	2.1	0.911
	1100		2565	7.8	0.864

Puosso et al. [38] obtained a grain growth exponent of 0.354 for a $Cr_{40}Co_{30}Ni_{30}$ alloy annealed at 1000 °C. This value is a near perfect match for the n obtained in this work. With the parameters described at Table 6.2, the proper grain growth curves could be plotted and are shown in Figure 6.20. Some of most noteworthy observations made were:

- The grain growth relationship obtained for AS and CS at both 900 and 1100 °C annealing temperatures describes well the experimental data;
- Carbon-doping the $Cr_{40}Co_{30}Ni_{30}$ alloy with 0.4 at.% was highly effective at hindering the GG kinetics. This is best shown when comparing the AS-900 °C samples' curve with that of the CS-1100 °C. They predict very similar grain growth, even though there is a 200 °C difference in the heat treatments.

Alternatively, the AS-1100 °C samples had a significantly more extreme grain growth when compared to all others curves;

- The effect of C in the GG kinetics can be evaluated by n, which decreased from 0.353 with no CD to 0.192 for the $Cr_{39.6}Co_{30}Ni_{30}C_{0.4}$ alloy (0.383 at.% carbon);
- For the BS alloy, it seems that CD (0.126 at.% carbon) resulted in an intermediate grain refining. However, n increased to 0.417.

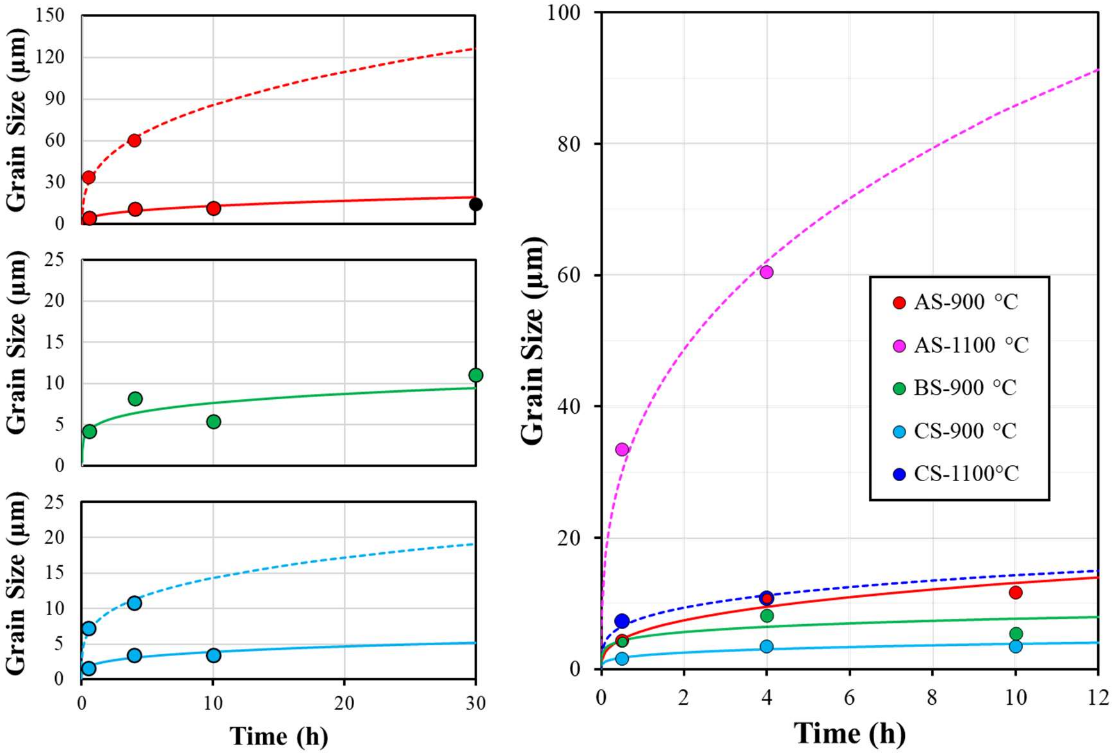

Figure 6.20. Grain size as a function of time for the $Cr_{40}Co_{30}Ni_{30}$ (red and pink), $Cr_{39.9}Co_{30}Ni_{30}C_{0.1}$ (green) and $Cr_{39.6}Co_{30}Ni_{30}C_{0.4}$ (blue) alloys annealed at 900 and (except for BS) 1100 °C. The back dot is the grain size measured for AS-30h900.

6.3 Mechanical Evolution in the Solution Treatment Route

After measuring the grain sizes, the mechanical strength was evaluated. Figure 6.21 shows the observed hardness values of all samples from the solution treatment processing route. There is a steep increase in hardness with cold rolling (CR) after the solution treatment (1195 °C for 1 hour) for all samples. Likewise, Vickers microhardness values fell with subsequently annealing, proportionally with increases in the heat treatments temperature and duration. Comparing the different materials, the general trend seems to indicate an increase of this mechanical property with C-Doping. To better illustrate this effect, plots indicating the relative variation in hardness values were plotted for each condition. Figure 6.22 compares CS to AS samples, while 6.23 is representative of BS to AS.

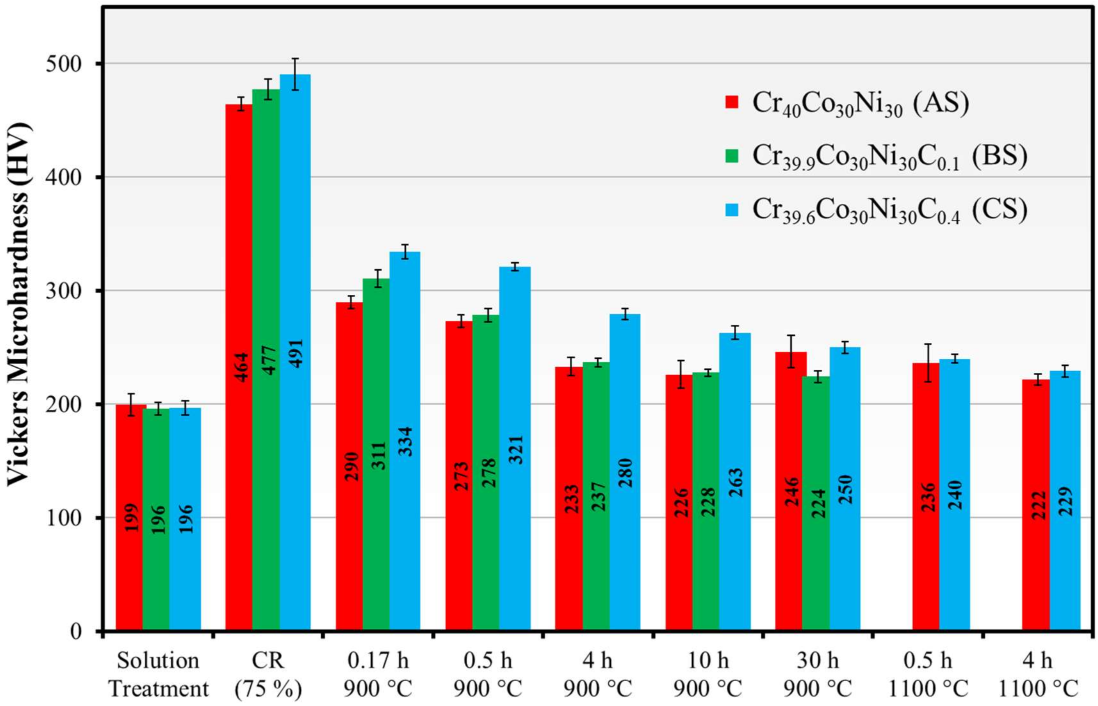

Figure 6.21. Hardness values for the solution treatment processing route.

In Figure 6.22, the conditions with no significant statistical variation in hardness (between the CS and AS sample, and evaluated with one-way ANOVA) are indicated with an asterisk (*). The observations made can be summarized as:

- With exception to 30 h, the $Cr_{39.6}Co_{30}Ni_{30}C_{0.4}$ samples annealed at 900 °C showed significantly higher (> 15 %) values of hardness than the $Cr_{40}Co_{30}Ni_{30}$ alloy;
- Adding carbon led to a minor increase in hardness during CR;
- CD resulted in little to no benefit to the evaluated property in samples heat-treated at 1100 °C. The same can be said for the samples after solution treatment;
- AS-30h900 showed a sudden increase in hardness. It was probably due to sigma phase precipitation (Figure 6.13).

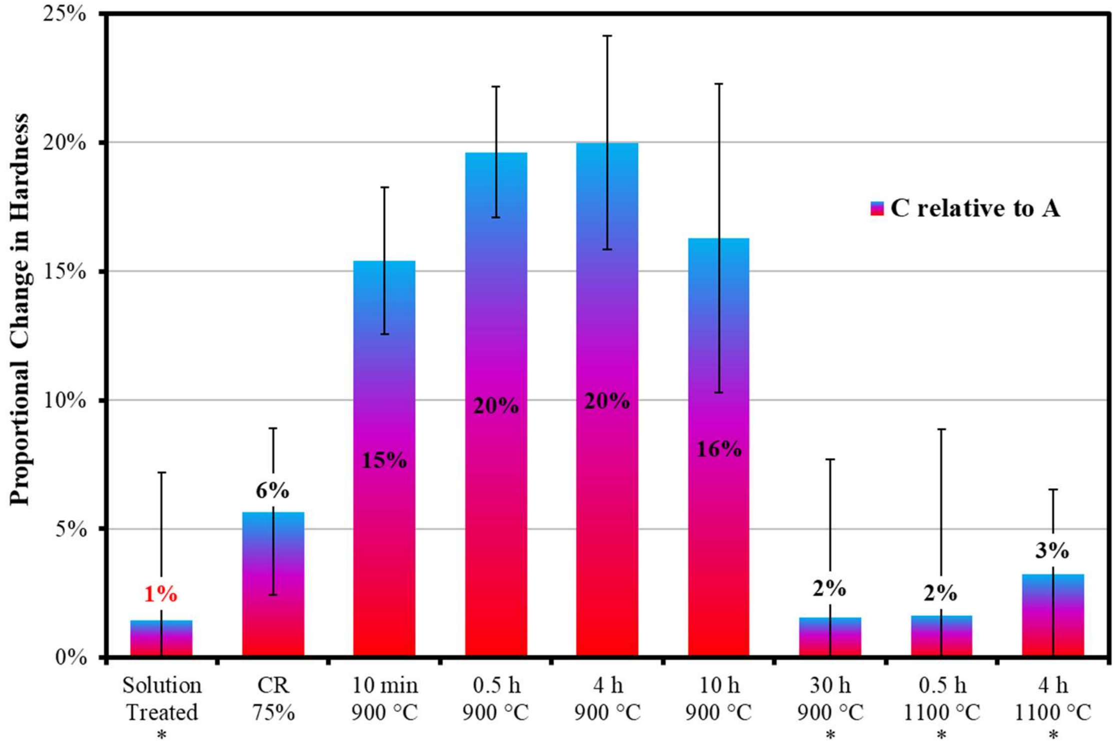

Figure 6.22. Percentual increase in Vickers microhardness values due to carbon-Doping for samples of the solution treatment processing route. Comparison between the $Cr_{39.6}Co_{30}Ni_{30}C_{0.4}$ (CS) and $Cr_{40}Co_{30}Ni_{30}$ (AS) alloys. Red font indicates decrease in hardness. There was no significative difference between the hardness for C and A in the conditions with an asterisk.

Differently than for CS, the carbon-doping of the $Cr_{39.9}Co_{30}Ni_{30}C_{0.1}$ samples resulted in fewer gains in hardness. For some conditions, these values even showed a decrease when compared to $Cr_{40}Co_{30}Ni_{30}$ (as indicated by red highlights in Figure 6.23). The main observations were:

- Only after annealing for 10 minutes did CD with 0.1 at.% resulted in higher values of hardness for BS;
- The other significant change was seen with 30 h annealing at 900 °C. However, it was the $Cr_{40}Co_{30}Ni_{30}$ sample that exhibited a better result, and probably due to sigma phase.

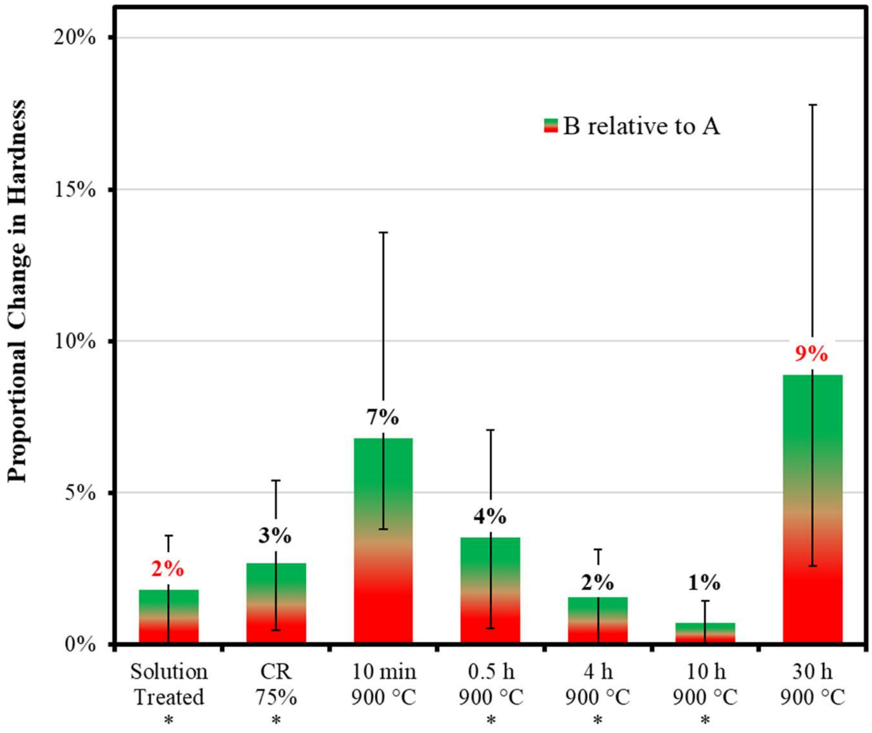

Figure 6.23. Percentual increase in Vickers microhardness values due to C-Doping for samples of the solution treatment processing route. Comparison between the $Cr_{39.9}Co_{30}Ni_{30}C_{0.1}$ (CS) and $Cr_{40}Co_{30}Ni_{30}$ (BS) alloys. Red font indicates decrease in hardness. There was no significative difference between the hardness for B and A in the conditions with an asterisk

Combining the results of average grain sizes for each sample (Figure 6.17) and their respective hardness values (Figure 6.21), Hall-Petch curves were plotted and are presented in Figure 6.24. For each alloy (A, B and C), the experimental points were fitted obtaining the linear relationship and HP parameters. These values are defined at Table 6.3. Samples AS-30h900, AS-0.5h1100 and AS-4h1100 were not used since their hardness values did not follow a logical decrease with grain growth. For AS-30h900 this could be, as discussed, due to the presence of second-phase particles. However, no plausible explanation was reached for the 1100 °C samples.

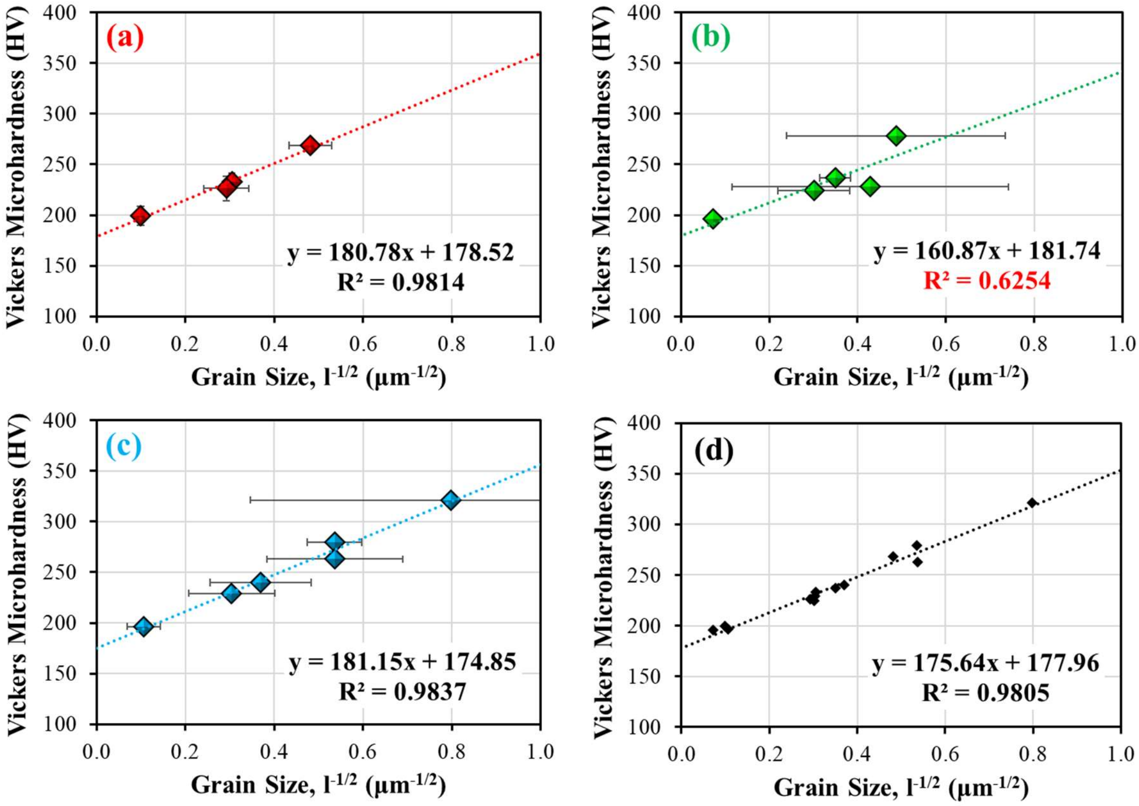

Figure 6.24. Hall-Petch relationship for the $Cr_{40}Co_{30}Ni_{30}$ (a), $Cr_{39.9}Co_{30}Ni_{30}C_{0.1}$ (b) and $Cr_{39.6}Co_{30}Ni_{30}C_{0.4}$ (c) alloys. (d) Was plotted by aggregating all the data points used in (a-c).

Table 6.3. Hall-Petch parameters obtained for AS, BS, CS and aggregation of all the data.

Material	H_0	k_H	R^2
$Cr_{40}Co_{30}Ni_{30}$	178.5	180.8	0.981
$Cr_{39.9}Co_{30}Ni_{30}C_{0.1}$	181.7	160.9	0.625
$Cr_{39.6}Co_{30}Ni_{30}C_{0.4}$	174.9	181.2	0.984
Combined	178.0	175.6	0.981

Just as it was for the GG analysis, the experimental data for $Cr_{39.9}Co_{30}Ni_{30}C_{0.1}$ did not fit well in the Hall-Petch relationship (R^2 of 0.625). Additionally, the $Cr_{40}Co_{30}Ni_{30}$ and $Cr_{39.6}Co_{30}Ni_{30}C_{0.4}$ alloys once again showed pretty reasonable results ($R^2 > 0.98$). Probably the most interesting observation from Figure 6.24 is the similarity between the H_0 and k_H parameters between both these materials (A and C). By having the same HP relationship, it would mean that, for an equal grain size, their hardness would also be equal. Consequently, carbon-doping (up to 0.4 at.%) could be considered effective mainly at grain size refinement. Additionally, this is the same as pointing out that the interstitial solid solution effect is negligible. The observation that the solution treatment samples all had virtually the same hardness corroborates to these ideas.

A Hall-Petch curve was also plotted with all the experiential values for A, B and C at once. This is shown at Figure 6.24d, and its respective parameters are on Table 6.3. With a correlation coefficient higher than 0.98, the aggregated HP curve also implies that the carbon-doping is mainly acting as a mean to reduce grain size, with no significant contribution to the mechanical strength. To further evaluate the effect of carbon-doping, the hardness dependency on time was also evaluated. Combining equations 3.22 and 6.2, the following relationship was established:

$$H = H_0 + k_H \cdot (A \cdot t^n)^{-1/2} \tag{6.4}$$

Utilizing the parameters obtained for HP and GG and equation 6.4, hardness versus time curves were calculated for each material. They are shown in Figure 6.25a-c together with the respective experimental points. AS-900, CS-900, CS-1100 were the only to show good correlation with the equation above. The R-value could not be measured for the 1100 °C alloys, because only two experimental points were available (in each case) for comparison. For alloy B (Figure 6.25b), R is low because the curve did not predict well the measured data. However, without Equation 6.4, the normalized hardness values were plotted for each group of samples and exponential fitting was tested. This is shown in Figure 3.40d, and it can be observed that good results were obtained all throughout.

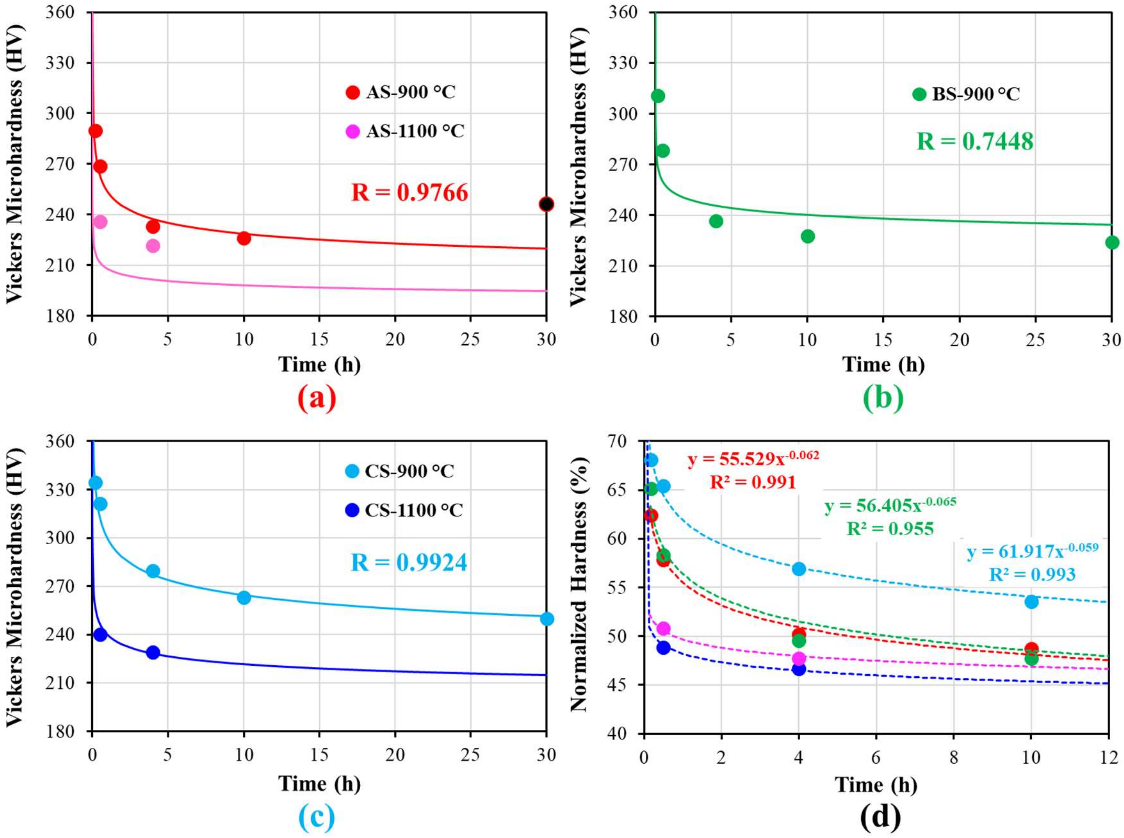

Figure 6.25. Relationships between hardness and annealing time for the different materials in the solution treatment processing route. The curves in (a-c) were plotted with equation 5.5 for the $Cr_{40}Co_{30}Ni_{30}$ (a), $Cr_{39.9}Co_{30}Ni_{30}C_{0.1}$ (b) and $Cr_{39.6}Co_{30}Ni_{30}C_{0.4}$ (c) alloys, and the respective experimental points are also depicted. In (d), for each group of samples, exponential regression was used to fit the experimental points normalized with the 75 % CR samples' hardness.

From Figure 6.25d it could be observed that $Cr_{39.9}Co_{30}Ni_{30}C_{0.1}$ showed almost the same reduction in hardness with annealing when compared to $Cr_{40}Co_{30}Ni_{30}$. For example, after 10 h, both alloys experienced roughly 52 % reduction in hardness when compared to cold rolling. For $Cr_{39.6}Co_{30}Ni_{30}C_{0.4}$ its value diminished only by 46 %. For 1100 °C, both alloys showed a steep reduction at lower durations, which is expected. The difference between AS-1100 °C and CS-1100 °C is not significative.

7 PROCESSING ROUTE WITHOUT SOLUTION TREATMENT

After TMH, the A, B and C alloys were cold rolled for 50 % thickness reduction, this is showed at Figure 4.6. However, as mentioned, processing was then divided in two routes. Here, the route following annealing directly after the 50 % CR is discussed. Namely, this was also called the processing route with no prior solution treatment (NS) to dissolve the carbides that formed during the TMH procedure. It is important to point out that the samples studied at the section 5.3 of this work were annealed after 50 % thickness reduction. As such, there is a difference of 70 % true strain between both scenarios. With less strain, the NS alloys also had less energy stored during plastic deformation, and consequently a lower driving force for recrystallization and precipitation. The hardness values for both processing routes were plotted in Figure 7.1.

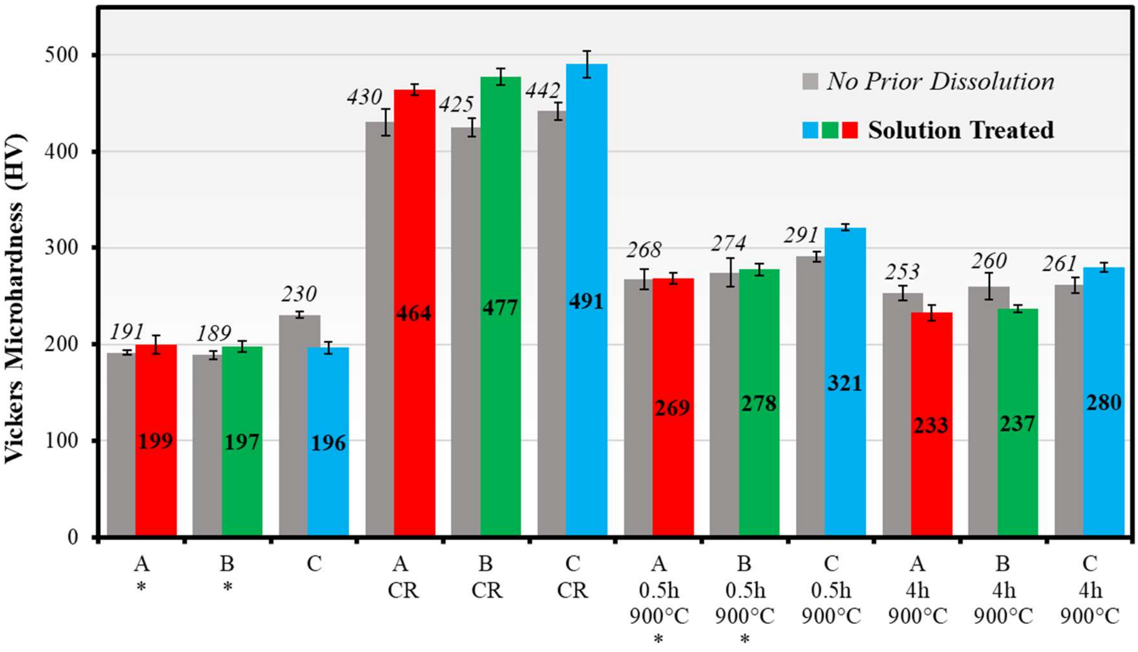

Figure 7.1. Hardness values for the NS processing route (grey) in comparison to the values obtained at the solution treatment route (red, green and blue). The starting conditions (A, B and C) are after TMH for the NS samples and after solution treatment for their respective samples. There was no significative difference between the hardness for the NS and S samples in the conditions with an asterisk

The main observations made from Figure 7.1 by comparing both processing routes were:

- The difference between A, B and C is very small in most conditions for the NS route, which is not the case for S samples;

- The average increase in hardness when comparing 75 % thickness reduction CR to 50 % was around 10 %;
- For A and B annealed at 900 °C for 4 h, hardness was higher for the NS route. In all cases after CR the hardness for C was higher for the S route.

To better illustrate the effect of carbon-doping in the NS route, plots indicating the relative variation in hardness values were plotted for each condition. Figure 7.2 compares CS to AS samples, while 7.3 is representative of BS to AS. In these figures, the Thermo-mechanically homogenized (TMH) and thermically homogenized (H, from the first stage of TMH) samples were also represented since carbon had precipitated heterogeneously (and that is the main difference from the solution treatment route).

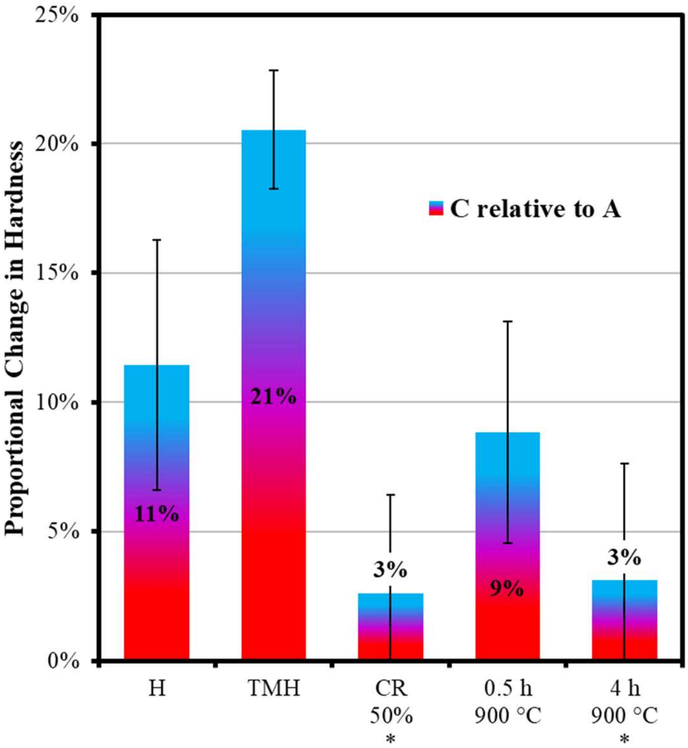

Figure 7.2. Percentual increase in Vickers microhardness values due to CD for samples of the processing route without carbide dissolution. Comparison between the $Cr_{39.6}Co_{30}Ni_{30}C_{0.4}$ (C) and $Cr_{40}Co_{30}Ni_{30}$ (A) alloys. Red font indicates decrease in hardness. There was no significative difference between the hardness for C and A in the conditions with an asterisk.

The main observations made by comparing the hardness of the C and A samples in the processing route with no solution treatment were:

- For H and TMH CD resulted in noticeable increases in hardness. In Figure 5.9 it was showed that C3 had a grain size less than half than those of A3 and B3;
- For the CR and annealed samples, the increases in hardness were subpar to those observed in the solution treatment route (Figure 6.22).

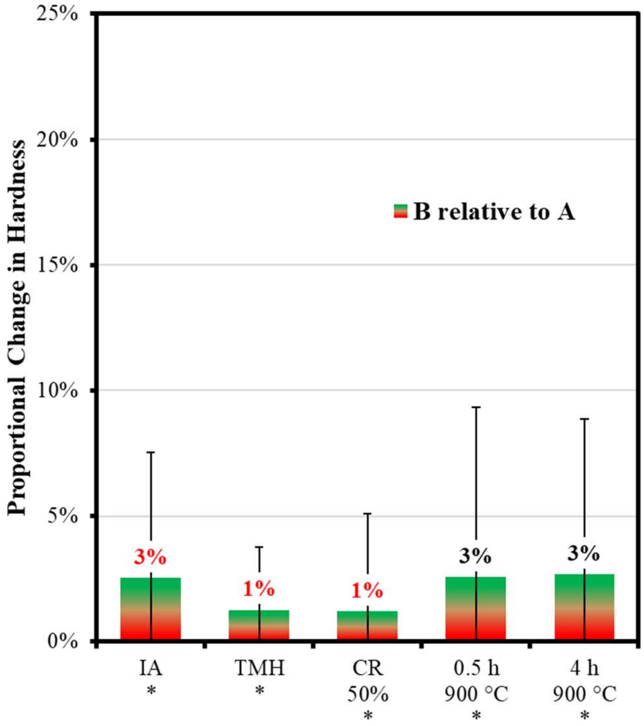

Figure 7.3. Percentual increase in Vickers microhardness values due to C-Doping for samples of the processing route without carbide dissolution. Comparison between the $Cr_{39.9}Co_{30}Ni_{30}C_{0.1}$ (B) and $Cr_{40}Co_{30}Ni_{30}$ (A) alloys. Red font indicates decrease in hardness. There was no significative difference between the hardness for B and A in the conditions with an asterisk.

Between the conditions compared in Figure 7.3 for the A and B alloys, there was no significative change in hardness. Likewise, in the solution treatment route, only for 10 min annealing did 0.1 at.% carbon-doping resulted in an effective increase in hardness (Figure 6.23). The microstructures of the ANS-4h900 and CNS-4h900 are shown in the appendix Figure A.2. A possible sigma formation was detected for ANS-4h900. The carbide’s distribution for CNS-4h900 has a clear banded arrangement, with very fine grains in the particle’s region and coarse grains in between.

8 SEVERE PLASTIC DEFORMATION PROCESSING ROUTE

Before cold rolling and after TMH, two samples were removed from the $Cr_{40}Co_{30}Ni_{30}$ and $Cr_{39.6}Co_{30}Ni_{30}C_{0.4}$ materials. These were then processed by High Pressure Torsion (HPT) at 6 GPa and for 5 rotations. Figure 8.1 shows the second-phase distribution for the C3 and C-HPT samples side by side. There was virtually no change in carbide dispersion. Since precipitation occurred heterogeneously in C2 (Figure 5.2.) the particles are mainly coarse. For C-HPT a higher magnification of the microstructure was analyzed with TEM imaging and is shown in Figure 8.2

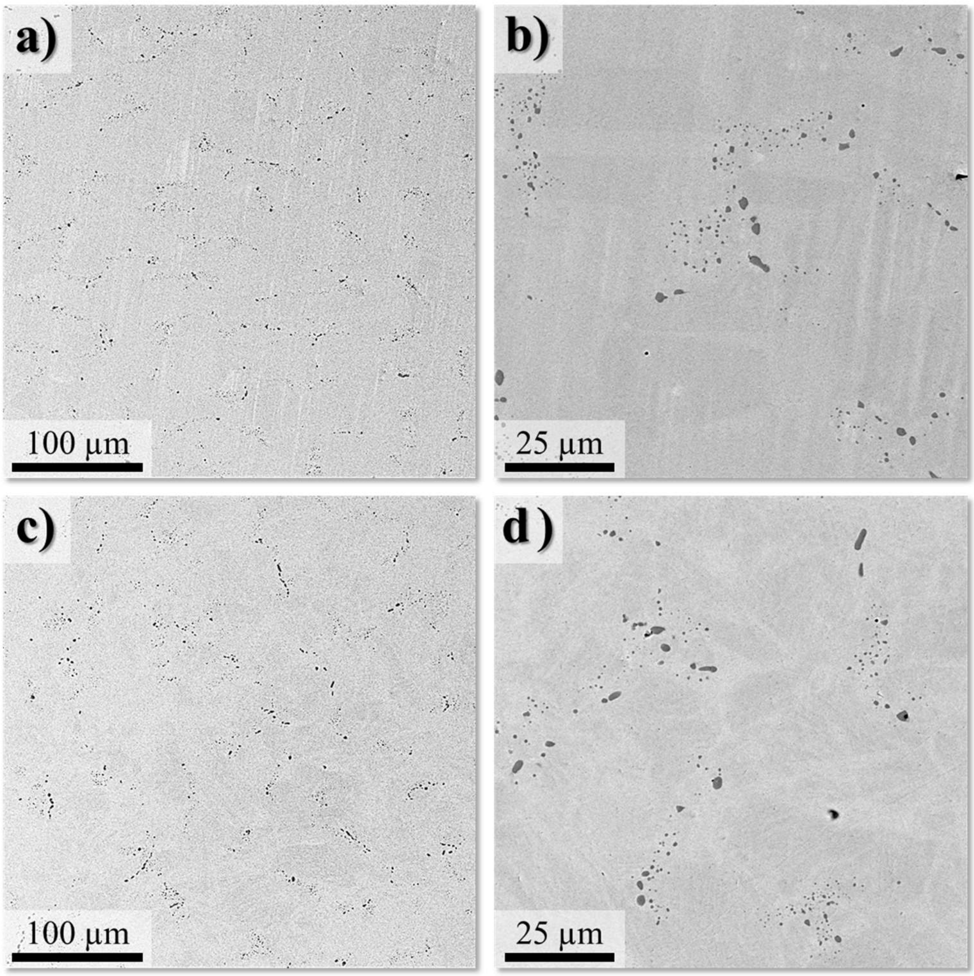

Figure 8.1. SEM-BSE characterization of the carbide distribution for the (a-b) C3 and (c-d) C-HPT samples

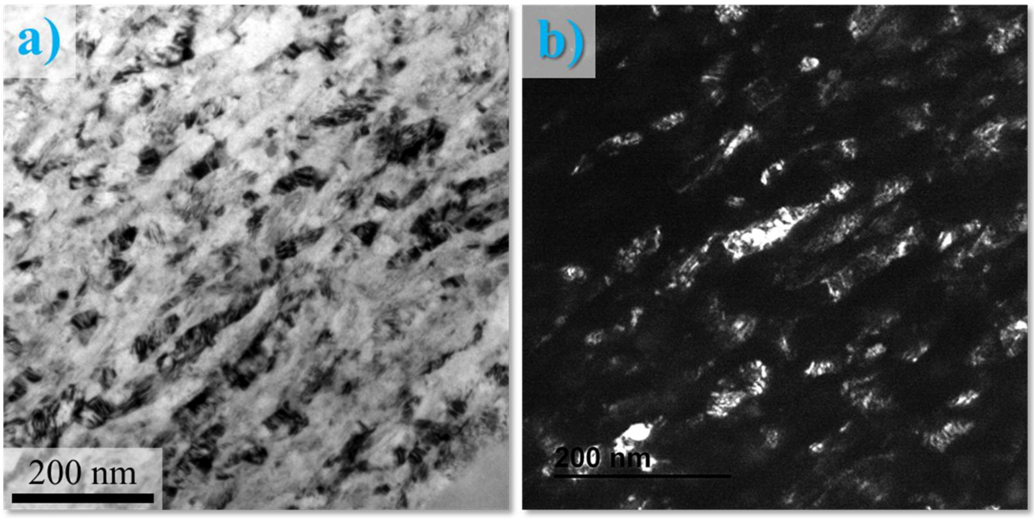

Figure 8.2. TEM characterization for the C-HPT sample with (a) BF and (b) DF. The lamella was removed perpendicularly from the torsion plane and to the disc radius and from a region at 0.9 mm from the sample's edge.

Through Figure 8.2 it is possible to see that a UFG distribution was achieved for the matrix and that the grains are elongated on the section analyzed (best seen in Figure 8.2b). Apparently, no carbide could be visually detected. However, SAED patterns were obtained for the regions observed with TEM imaging (10 separate fields were screened). These results are shown in Figure 8.3

Mostly matrix fcc spots could be detected for the SAEDs in Figure 8.3. These appeared arranged in circle-like patterns due to the selected area covering multiple grains. Image artifacts were also visible and some discrepant spots were faintly detected for some of the patterns (indicated by red arrows). Nevertheless, it seems that carbides are mostly found in coarse distribution. These particles were also not detected through the XRD technique, which can be observed in Figure 8.4. For the $Cr_{40}Co_{30}Ni_{30}$ alloy processed under HPT no hcp phase peak was detected (no TRIP effect indication).

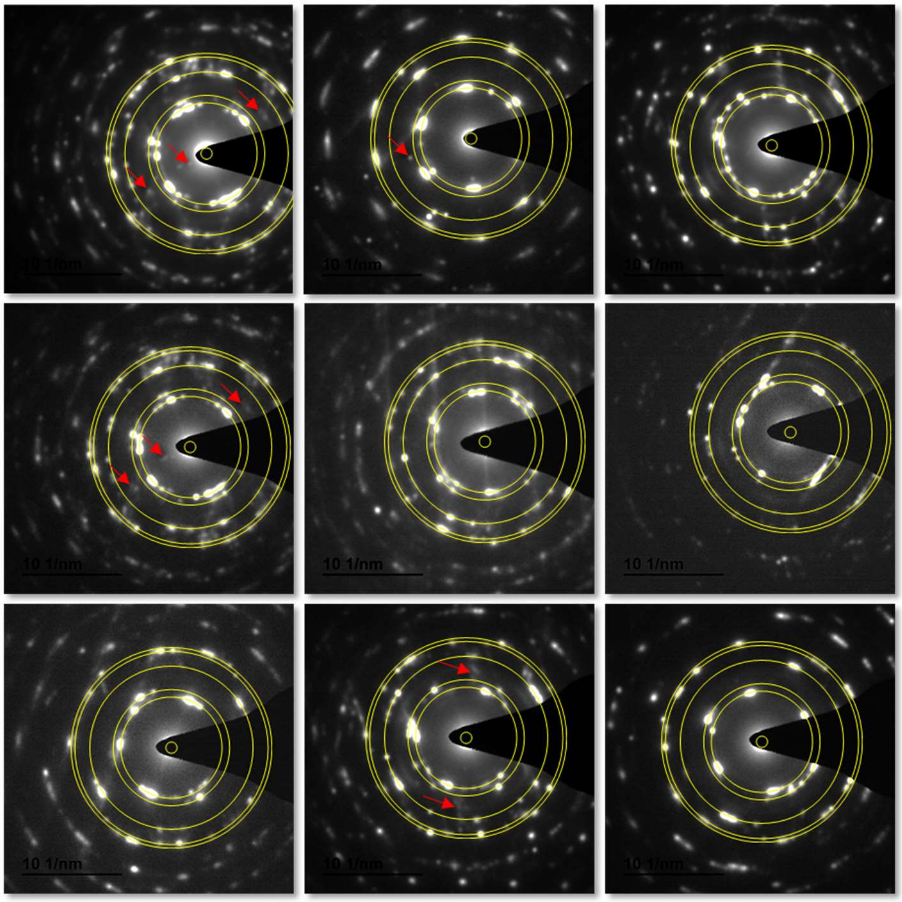

Figure 8.3. SAED patterns for different regions of the TEM lamella from the C-HPT sample, like those of Figure 8.2. Red arrows indicate diffraction spots not relative to the matrix.

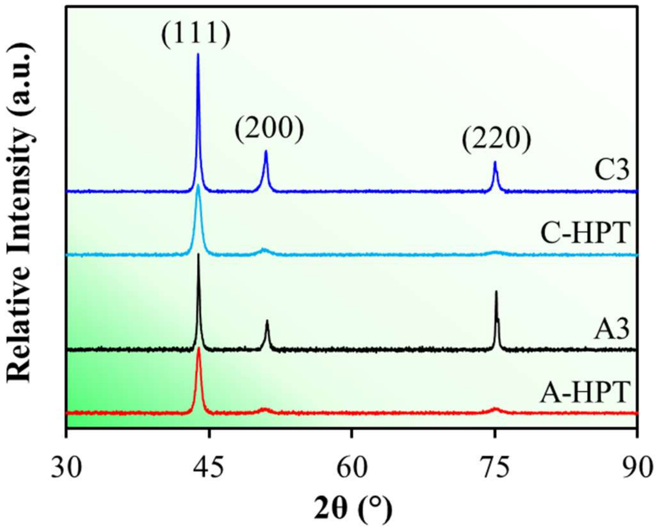

Figure 8.4. X-ray diffraction patterns for the A3, C3, A-HPT and C-HPT samples.

In the X-ray diffractograms, it was observed a strong {111} texture formation (in the torsion/normal plane) for the HPT samples when compared to the annealed samples (i.e., those after TMH). Peak broadening is also observed at this condition, and is likely a consequence of the UFG structures achieved [63]. Likewise, it could also be due to lattice distortion caused by the concentration of deformation defects such as dislocations [63].

Figure 8.5. shows the microstructures of the A-HPT and C-HPT samples under STEM analysis. Comparing them side by side, it is clear that carbon-doping was effective in grain size refinement even under severe plastic deformation. To measure the grain size more effectively, ASTAR analysis was carried out for both samples. Image cleanup was made with the grain dilation option with an angle limit of 5° and a minimal grain size of 5 pixels. Inverse pole figure (IPF) images, plotted with ASTAR results, are shown in Figure 8.6.

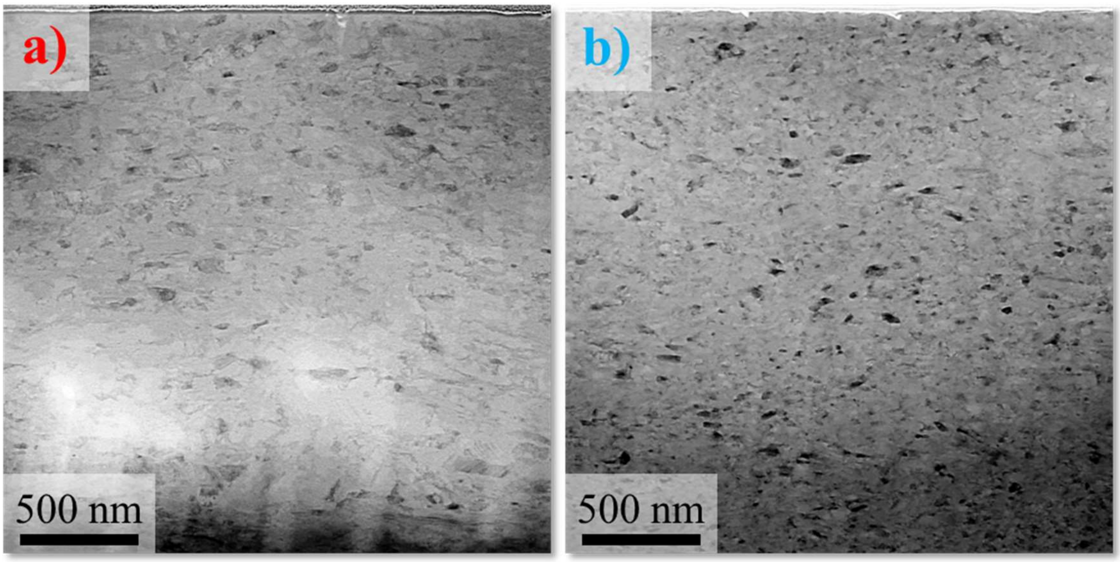

Figure 8.5. BF STEM micrographs for the (a) A-HPT and (b) C-HPT samples.

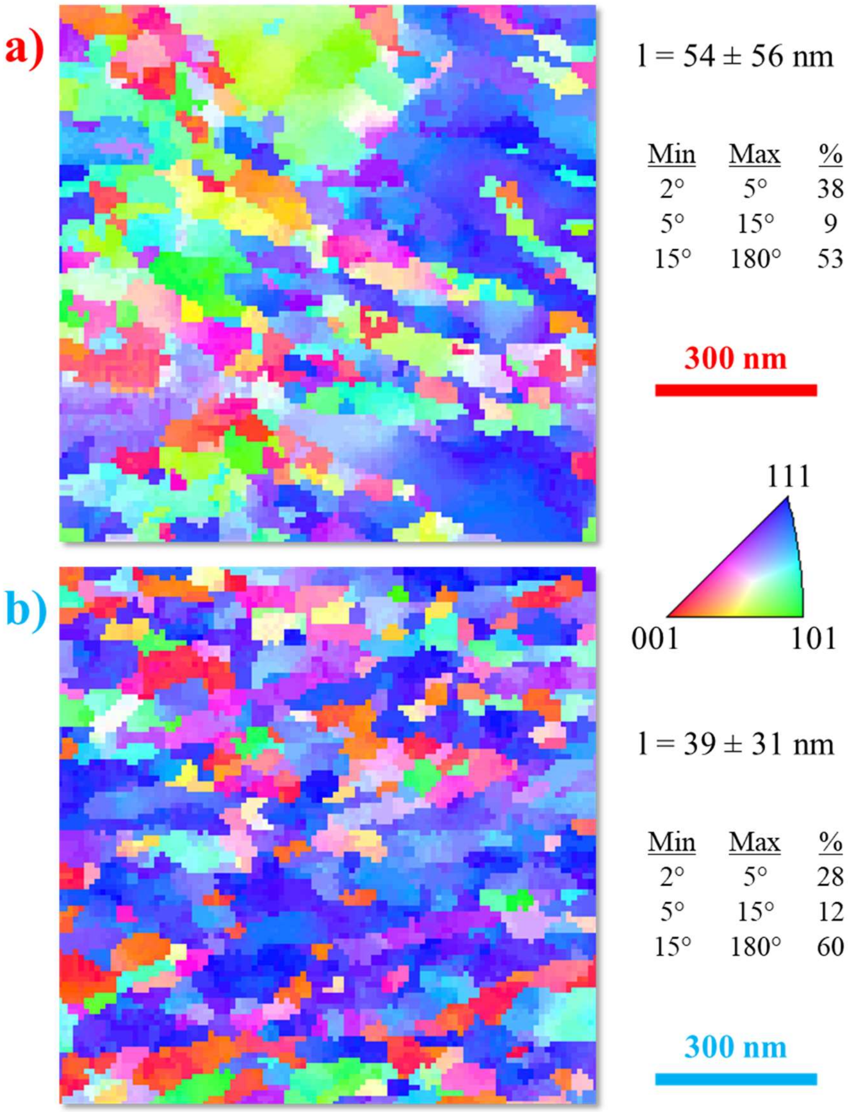

Figure 8.6. Inverse pole figure images rotated to match the torsion/normal plane of the HPT samples for the (a) $Cr_{40}Co_{30}Ni_{30}$ and (b) $Cr_{39.6}Co_{30}Ni_{30}C_{0.4}$ alloys. At the right of each image the respective values for average grain size (mean linear intercept) and boundaries fraction distribution are depicted.

Figure 8.6 presents “Inverse Pole Figure” (IPF) images for the HPT processed alloys. For which a {111} texture is observed, just like it was for the XRD analysis (Figure 8.4). To the right side of the images, their respective grain sizes and boundaries data are described. C-HPT showed a calculated (with 5 to 180° boundaries) grain size value of 39 ± 31 nm, 28 % smaller than the value obtained for A-HPT (54 ± 56 nm). Similarly, the value measured for C3 (12.9 ± 2.4 µm) was 60 % smaller than for A3 (32.2 ± 3.5 µm). The refinement presumably contributed, to some extent, in an increased hardness for C-HPT when compared to A-HPT. These values are shown in Figure 8.7. The ASTAR grain size measurements are in well agreement to an evaluation made with the intercept method on the TEM images.

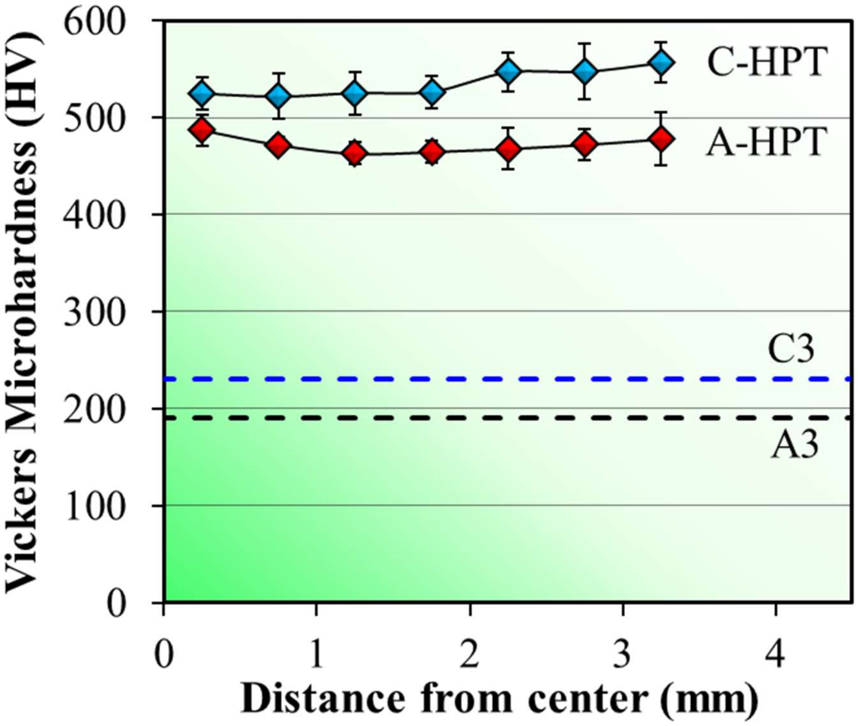

Figure 8.7. Vickers microhardness for the A3, C3, A-HPT and C-HPT samples. The distance from center of the disk is only applicable for the HPT samples. The annealed alloys' hardness values are represented for comparison.

For Figure 8.7, the hardness was measured throughout the HPT disks' diameter (the average values for A3 and C3, independent of distance from center, are also depicted for comparison). The 5 rotations HPT processing resulted in a hardness saturation for both alloys. C-HPT showed an average hardness of 536 ± 25 HV versus the 472 ± 18 HV observed for A-HPT. For both the annealed and HPT conditions CD resulted in similar increases in hardness (20 and 14 % respectively). To further evaluate the mechanical behavior of the alloys processed by HPT, a Plane strain compression (PSC) test [55] was carried out . The results are shown in Figure 8.8.

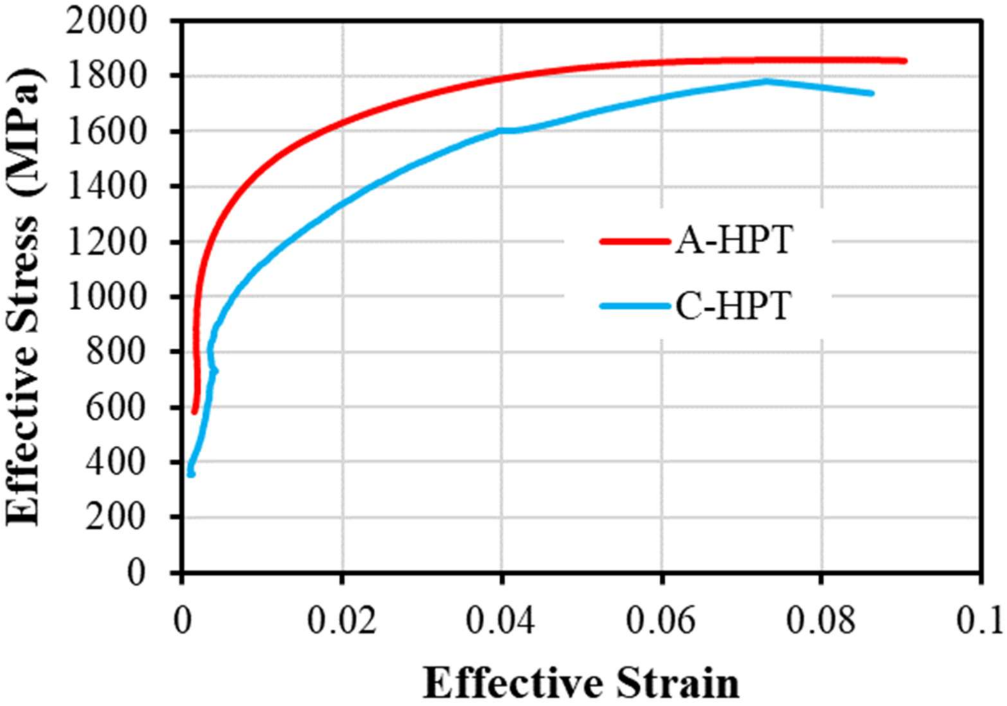

Figure 8.8. Plane strain compression curves for the alloys processed by HPT. Strain rate of 10^{-3} s^{-1}. The C-HPT sample failed during testing. The experiments were conducted once, for each sample, without replicates.

It is possible to see, in Figure 8.8 that the effective stresses reached by the samples under PSC deformation reached values higher than 1.7 GPa. A-HPT showed higher values of "strength" in the mechanical testing, but both curves were relatively close for all strain levels. Additionally, the PSC mechanical test is not highly accurate and can be affected by strain localization, the geometry of deformation zone and friction [55]. It must be pointed out that the PSC was not carried out for replicated (for statistical consistency) samples and that the C-HPT failed before the end of the test. Nevertheless, the results are at least valuable to portrait the very high levels of stress these samples could sustain. The fractography analysis of the C-HPT alloy after PSC is shown in Figure 8.9.

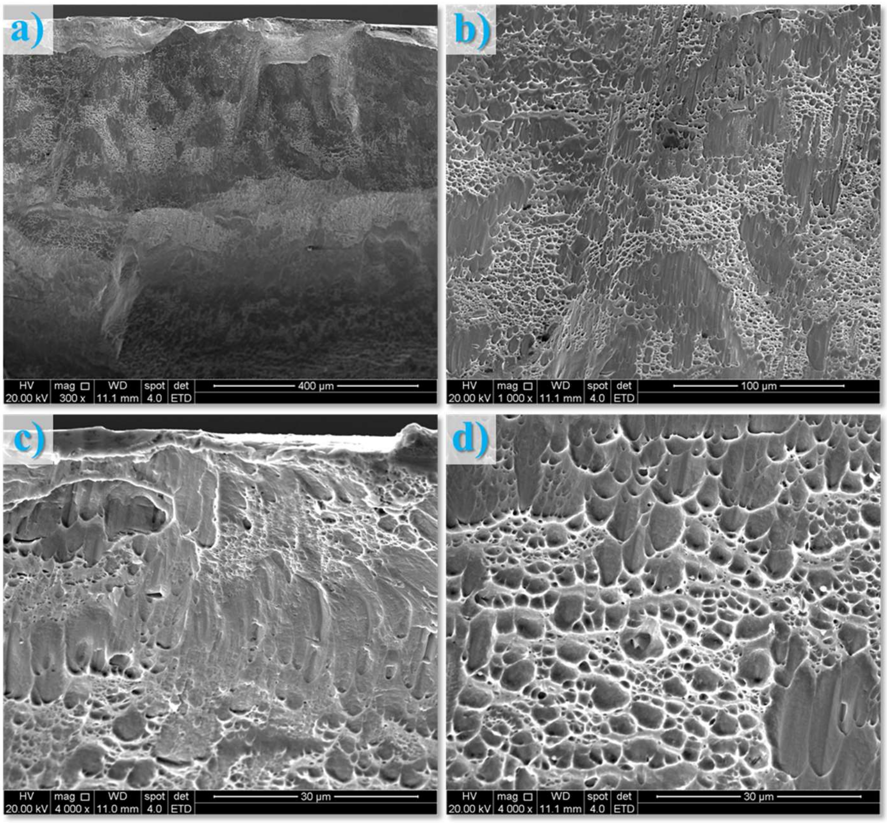

Figure 8.9. SEM-SE fractography analysis for the C-HPT sample after fracture during PSC testing. The fracture (observed) plane is parallel to the disk's radius and perpendicular to the torsion plane. Round microstructural features are dimples.

With some regions having a concentration of smaller and circular dimples, while others show these features in an elongated morphology (parabolic-shaped) and with larger individual sizes. Both are indicative of a ductile fracture [64]. The carbon-doped HPT alloy showed a fractography aspect that appears to have similar or higher ductility when compared to CrCoNi equiatomic alloys failed after tensile testing, be it at 293 K or 77 K [21,60,65,66]. Namely, the dimples in Figure 8.9 are larger than those of the CrCoNi materials found at literature after tensile testing (except that in the PSC the compression pressures should favor higher ductility). Well succeeded efforts in increasing the CrCoNi mechanical properties without compromising the ductility were achieved by Carbon-Doping (CD) the equiatomic alloy in small quantities (up to 1 at.%). These samples maintained similar amounts of elongation to fracture while increasing the strength and overall toughness [61,67]. However, it is important to remind that the sample without CD (A-HPT) did not fracture during the PSC test.

Severe plastic deformation can lead to dynamic recrystallization (DRX) and thus diminish the amount of stored deformation on a sample's bulk [50]. To evaluate this issue the substructures of the HPT samples was evaluated with grain orientation spread (GOS) and Kernel average misorientation (KAM) analyses. The results are depicted in Figures 8.10 (A-HPT) and 8.11 (C-HPT).

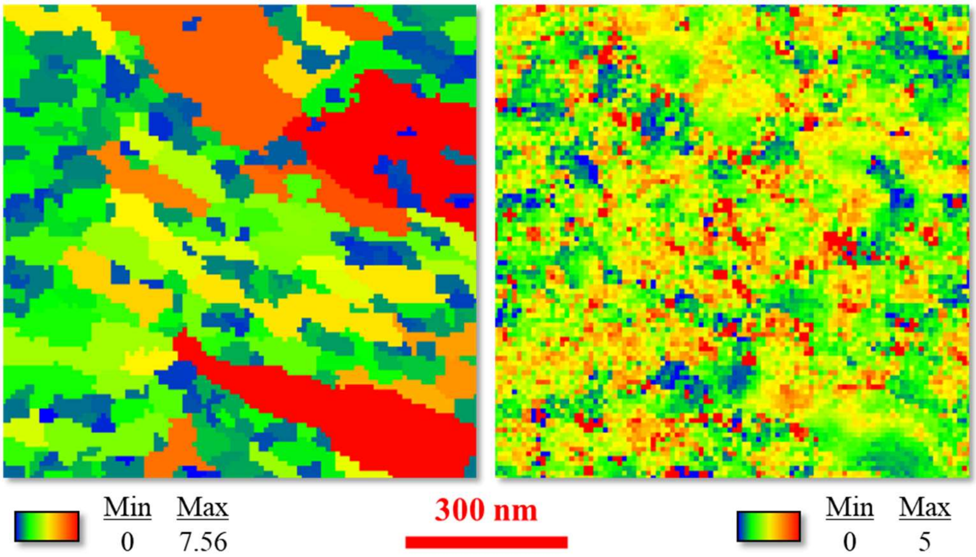

Figure 8.10. GOS (left) and KAM (right) maps for the $Cr_{40}Co_{30}Ni_{30}$ alloy processed by HPT. The respective intensity scales are located below each map.

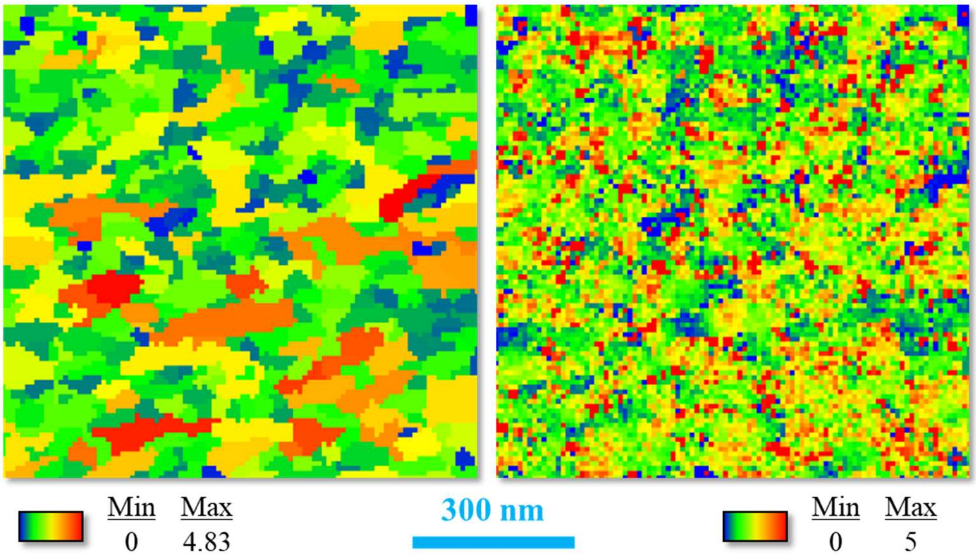

Figure 8.11. GOS (left) and KAM (right) maps for the $Cr_{39.6}Co_{30}Ni_{30}C_{0.4}$ alloy processed by HPT. The respective intensity scales are located below each map.

The GOS maps (Figures 8.10 and 8.11) show that continuous dynamic recrystallization (CDRX) took place for both samples. The fraction of CDRX was estimated with grains where GOS values were lower than 1° [68]. As such, A-HPT and C-HPT showed CDRX fractions of 25 and 34 % respectively. The steady-state hardness exhibited for both samples (Figure 8.7) corroborates to this observation. The KAM maps indicate that both samples have a similar amount of stored deformation (KAM values of 2. 18° for A-HPT and 2.15° for C-HPT). Albeit A-HPT has a slightly higher concentration of low angle grain boundaries (up to 5° misorientation, as indicated in Figure 8.6). The KAM maps reveal that both samples have similar amounts of stored deformation, with KAM values of 2.18° for A-HPT and 2.15° for C-HPT. However, A-HPT exhibits a slightly higher concentration of low-angle grain boundaries, with misorientations up to 5° as indicated in Figure 8.6.

The HPT processed samples were further characterized with STEM technique to study the substructure and its features. Individual grains in a <110> zone axis for both alloys are depicted in Figures 8.12 (for A-HPT) and 8.13 (for C-HPT). They appear in darker contrast for BF imaging. It is important to note that multiple grains were analyzed and these trends were consistently observed.

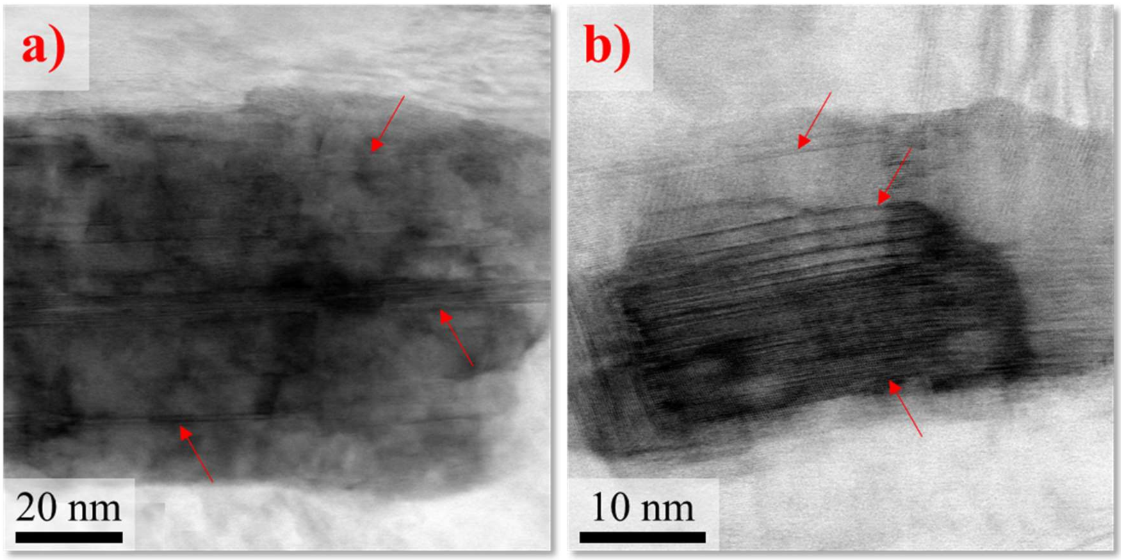

Figure 8.12. HR-STEM BF imaging for the $Cr_{40}Co_{30}Ni_{30}$ alloy processed by HPT. Red arrows indicate examples of fringes. Black grains are oriented in the <110> zone axis

Fringes indicating the presence of stacking faults (SFs) and nanotwins (or even hcp laths) [62] are present at large quantities for A-HPT (Figure 8.12). For the C-HPT alloy (Figure 8.13) there does not seem to be a considerable amount of these lines. Instead, it was detected a high fraction of smaller and intersecting lines composing a network of defects similar to dislocation slip lines for fcc materials, and they cross each other at an approximate angle of 70 degrees. Notably, 70.5° is the characteristic angle between the {111} planes visible in a <110> zone axis section, which is the case. It is important to note that multiple grains were analyzed and these trends were consistently observed.

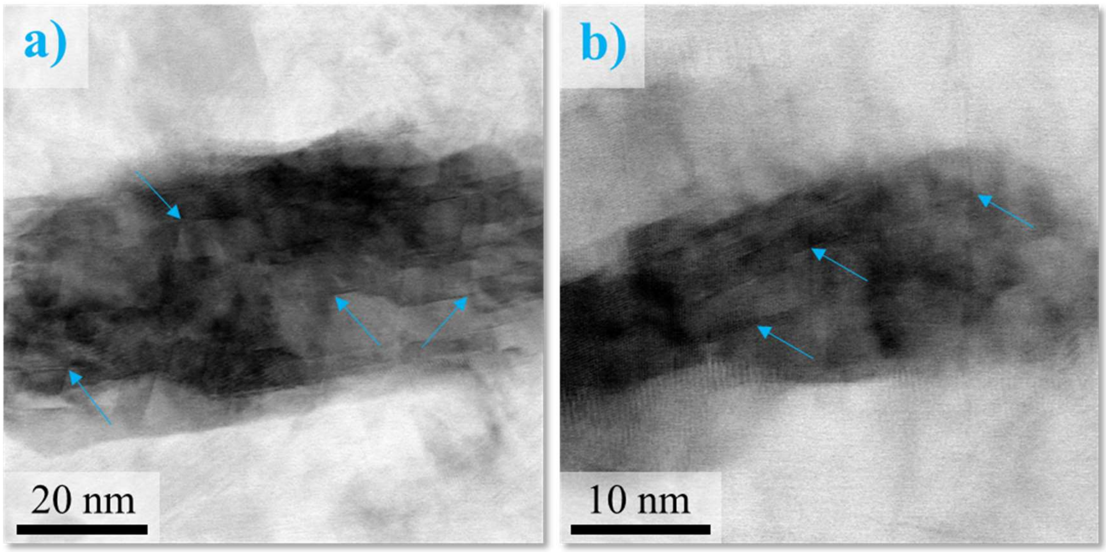

Figure 8.13. HR-STEM BF imaging for the $Cr_{39.6}Co_{30}Ni_{30}C_{0.4}$ alloy processed by HPT. Blue arrows indicate examples of intersection between fringes. Black grains are oriented in the <110> zone axis

Atomic scale HRSTEM was utilized to further investigate the HPT samples. Figure 8.14 shows HAADF-STEM images for A-HPT and C-HPT with highlights for a <110> zone axis. Center of Symmetry (COS) color maps [53] and Fast Fourier Transformation (FFT) images were plotted to help visualize the substructure features. These analyses are represented in Figures 8.15 and 8.16 for the A and C materials respectively and 8.14 for both.

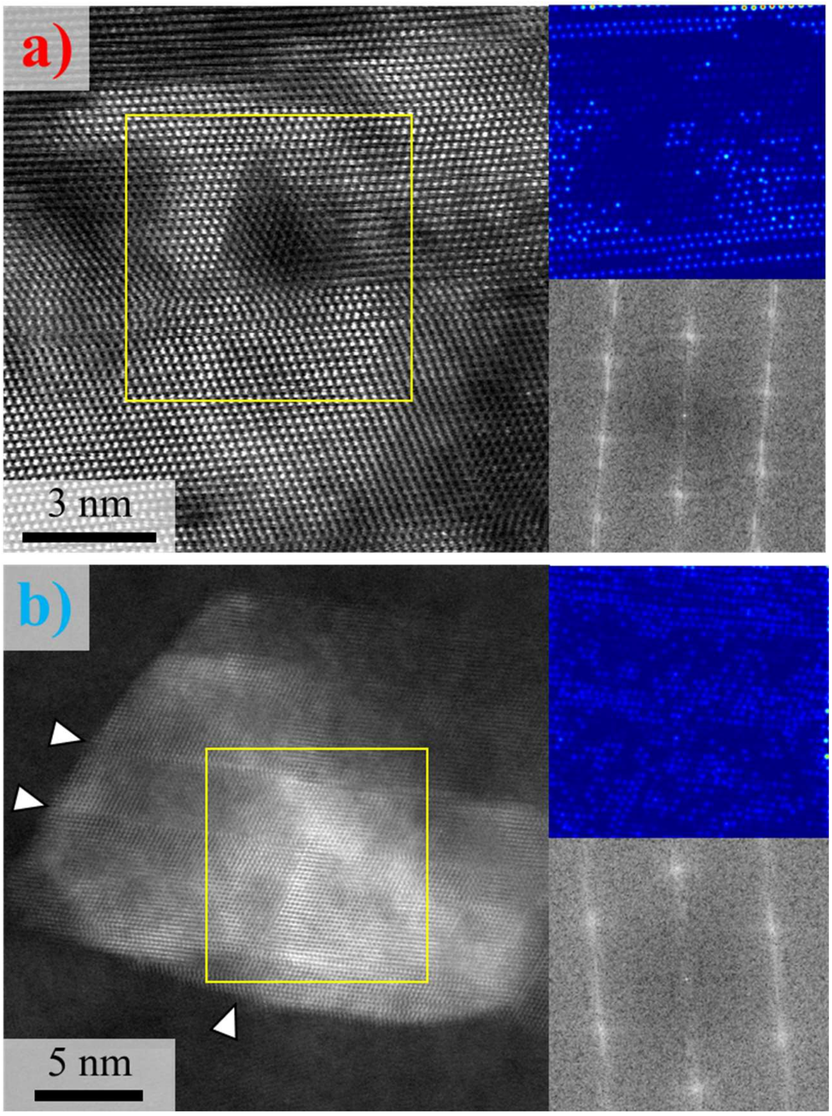

Figure 8.14. HAADF-STEM imaging for the (a) $Cr_{40}Co_{30}Ni_{30}$ and (b) $Cr_{39.6}Co_{30}Ni_{30}C_{0.4}$ alloys processed by HPT. The <110> zone axis is highlighted. COS maps and FFT were plotted for the regions indicated by yellow squares and are depicted in the right of the respective sub-micrographs. In (b) SFs are indicated by white arrows.

For A-HPT (Figures 8.14a and 8.15), fully developed nanotwins and hcp lamellae could be detected, and confirmed with the COS an FFT analyses. A large nanotwin was observed in the grain depicted at Figure 8.14a. The COS map shows that this region is separated from the matrix by multi-layered faults with hcp lamellae. In Figure 8.15 a fully developed hcp nano-lamella, with more than 10 atomic layers, is visible at the top-most part of the image.

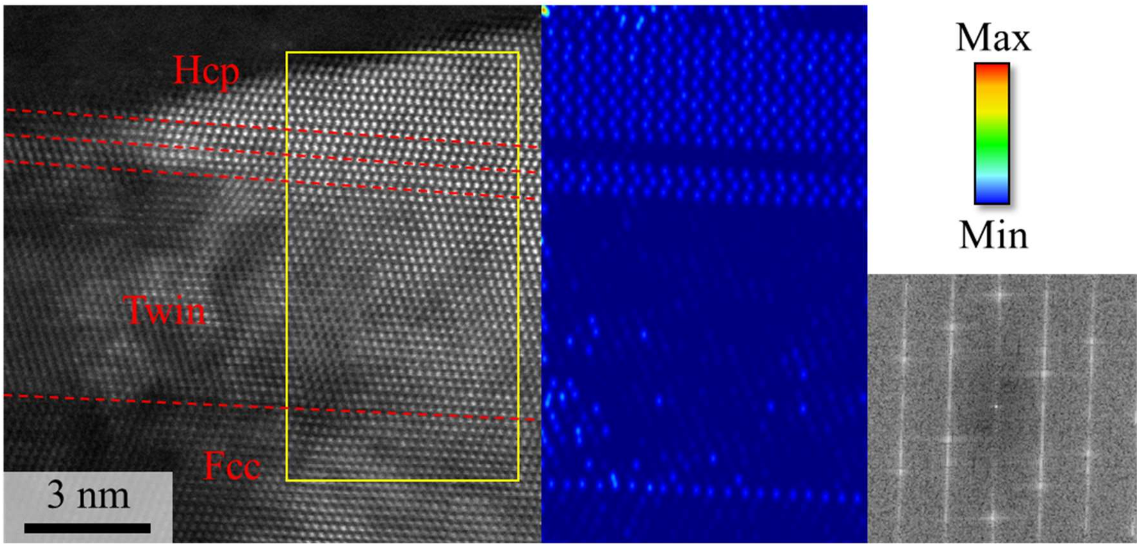

Figure 8.15. HAADF-STEM imaging for the $Cr_{40}Co_{30}Ni_{30}$ alloy processed by HPT. The <110> zone axis is highlighted. COS maps and FFT were plotted for the regions indicated by yellow squares and are depicted in the right of the respective sub-micrographs.

The A-HPT sample is shown to have stacking faults that evolved into multiple layers, resulting in the formation of considerable large lamellae of hcp and nanotwins. This is coherent with what is reported in the literature for Cr-Co-Ni fcc alloys and other similar MPEAs under quasi-static tensile testing [22,30,32–40]. At lower strains and room temperature (RT) planar slip is the primary mode of deformation, and mainly dislocations and slip bands constitute the substructure. With increasing strain, first stacking faults density rise, followed by the nucleation of nanotwins, and at the final stage of plasticity hcp transformation takes place. Miao J. et al. [30] pointed out that the hcp laths are observed mainly interspersed with nanotwins as a nanotwin-hcp lamellae configuration. This is true for the other literature researched in this study.

Just as with increasing strain, reducing the temperature has a similar effect at favoring TWIP and TRIP effects. At 77 K the SFE is inarguably lower than at RT, and this may be one of the reasons these effects are more recurrent [21,30,33,69]. This property is mainly controlled by chemical composition. Based on empiric predictions $Cr_{40}Co_{30}Ni_{30}$ should have an SFE value of 16 mJ/m^2 at RT when compared to the 20 mJ/m^2 from the equiatomic alloy [27]. When deformed at 70 % strain under quasi-static tensile testing at RT, the substructure of a $Cr_{40}Co_{30}Ni_{30}$ alloy has shown several well-developed hcp laths alternated with nanotwins [38].

For the C-HPT sample (Figures 8.14b and 8.16), neither twinning nor hcp regions could be detected at atomic resolution. The COS analyses of this sample show that the highlighted regions (relative to changes in the fcc stacking) are thin and can be characterized as simple SFs. Figure 8.16 is a higher magnification of Figure 8.13b, which confirms that the deformation defects seen in Figure 8.13b as SFs rather than nanotwins or hcp. In the FFTs only the fcc matrix spots are present, while for A-HPT twins and hcp spots also appeared. Streaking in the spots is visible for both samples due to stacking faults presence (C-HPT, resulting in a parallelogram shape in Figure 8.16) or border effects (A-HPT, vertical).

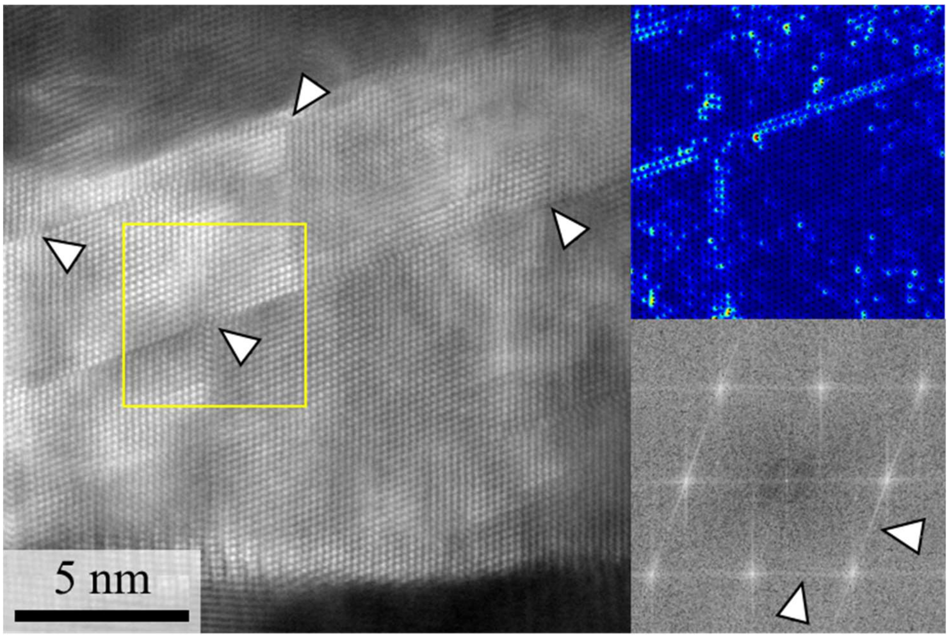

Figure 8.16. HAADF-STEM imaging for the $Cr_{39.6}Co_{30}Ni_{30}C_{0.4}$ alloy processed by HPT. The <110> zone axis is highlighted. COS maps and FFT were plotted for the regions indicated by yellow squares and are depicted in the right of the respective sub-micrographs. SFs and their presence in the FFT are indicated by white arrows

The Carbon-doping seems to have deactivated TWIP and TRIP effects, which can be a result of an increase in SFE. Shang Y. et al. observed an increase of 6 mJ/m^2 (to 24) in the SFE of a CrCoNi when alloyed with C at 0.25 at.% and homogenized at 1200 °C. The CD samples have similar quantity of C in solid solution (0.22 at.%), and should have a similar rise in its SFE. Furthermore, achieving a UFG distribution should also contribute to a higher SFE when compared to the coarser annealed samples [69,70]. The relationship of this property with grain size has been studied for Fe-Mn alloys, where a relationship between the increment of SFE due to grain size was stablished [69–73]:

$$SFE\ (mJ/m^2) = 2 \cdot [\rho] \cdot [\Delta G_{ex}] = 2 \cdot \left[\frac{4}{a^2 N_a \sqrt{3}}\right] \cdot \left[170.06 \cdot exp\left(\frac{-d}{18.55}\right)\right] \quad (8.1)$$

Where ρ is the molar surface density and ΔG_{ex} is the excess free energy due to grain size. Also, N_a is the Avogadro's number, *a* the lattice parameter (indicated in Figure 5.7) and *d* the grain size in µm. For both HPT samples, the calculated value was 10.15 mJ/m^2. There is no virtual difference due to the exponential character of the equation 8.1, which leads to a plateau at *d*'s smaller than 1 µm. This is best shown in Figure 8.17, in which the values for the SFE increments, due to reduction in grain size, were calculated for the material A with the parameters mentioned above.

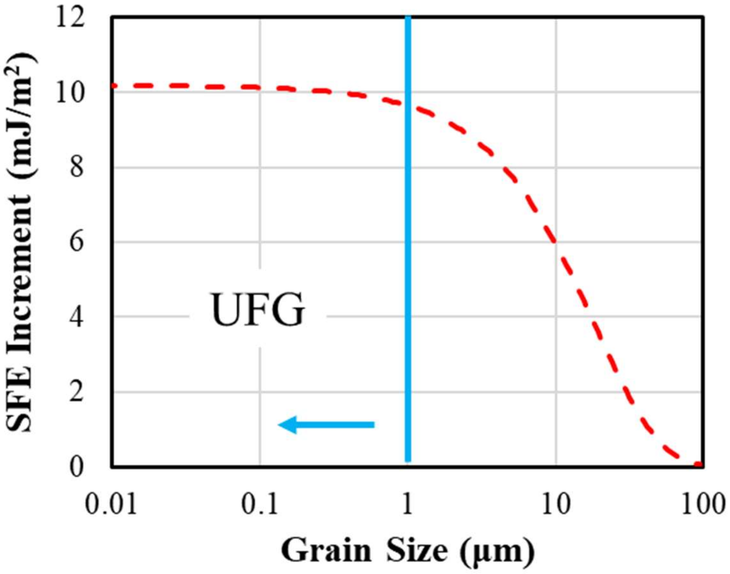

Figure 8.17. Calculated SFE increment due to the average grain size. The graph was plotted using equation 8.1 with the lattice parameter for $Cr_{40}Co_{30}Ni_{30}$ (Figure 5.6).

As discussed above and demonstrated with Figure 8.17, SFE increase with grain size should not explain the difference in substructure for the HPT samples, since they have UFG structures. However, grain refinement is also known to increase the critical stress for twinning, which could be a decisive for deactivating TWIP effect [29,69]. Likewise, d is very similar between samples and may not have a significant role.

It seems that by increasing the overall SFE there was a suppression of the plasticity induced effects (TWIP/TRIP) in favor of the formation of a network of stacking faults in multiple slip systems. Both are expected to occur together with dislocation slip. Partial dislocations slip and the formation of stacking faults are the first step proposed for nucleation of TWIP/TRIP deformation products [26,69,74]. However, as discussed previously, the severe strain levels have already led to a steady-state of CDRX on C-HPT. Therefore, this material should not develop twins nor hcp with further deformation at room temperature. These features are most likely to appear if the temperature is greatly reduced at the HPT processing.

The drag effect of interstitial carbon is also believed to be primordial in generating the SFs network, since it can impinge partial dislocations thus diminishing TWIP and TRIP effects [42,75]. This mechanism also impacts the boundaries migration (as discussed before), consequently promoting grain refinement (as seen by the IPF results). Additionally, the interstitial solid solution strengthening may also have had some contribution to the higher values of hardness of the $Cr_{39.6}Co_{30}Ni_{30}C_{0.4}$ samples, which was the case for other CD CrCoNi alloys [61,67]. However, as discussed in section 6 of this work, the effect of interstitial carbon in the alloy's hardness is negligible even at higher amounts (which was the case for the sample after the carbide dissolution treatment, CS).

Due to the more planar deformation character of the A-HPT sample and its lower yield strength, most of the deformation products are concentrated on the main slip system. Alternatively, CD has led to an increase of the critical stress for twinning and hcp formation. This should facilitate cross-slip [24], allowing for a higher occurrence of slip on the conjugate planes before the formation of well-developed twins and hcp which leads to SFs appearing on multiple slip planes. Additionally, with this mechanism facilitated, dislocation climb could have been less favored in the C-HPT alloy, hindering stacking fault's thickening as shown by Miao J. et al. work [30]. Namely, the climb of extended dislocations in the vicinity of a nanotwin boundary can extend it into a multi-layered hcp lamella.

In contrast with the present work, Chang H. et al. [76] reported a similar pattern in the substructure of a $CrCoNiSi_{0.3}$ alloy. However, it was achieved with the decrease of SFE by adding Si and consisted on inter-crossed twins constituting the network, that was relatively coarser (not by much). This is not unexpected since both features develop on {111} planes. An actually virtually identical network of SFs was predicted by atomistic simulation for a polycrystalline CrMnFeCoNi alloy under tension at 77K with an average grain size of 48.6 nm [77]. At 10 % applied strain the SFs and partial dislocations started to appear significantly in the 3 distinct {111} deformation planes. In their simulations, Liu et al. demonstrated that these SFs acted as barriers to slip leading to increments of stress or even the trap of partials. Figures 8.18a and 8.18b show a schematic representation of the substructure formed in A-HPT and C-HPT samples respectively.

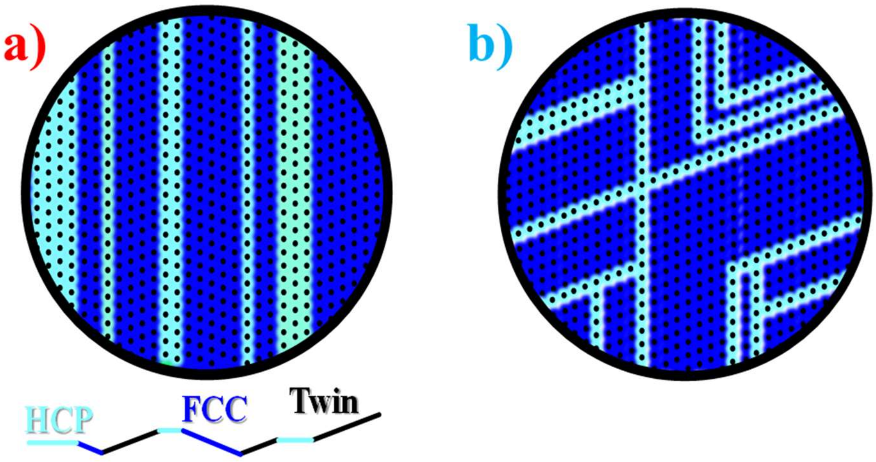

Figure 8.18. Schematic representations for the substructure, as seen in COS maps, after high levels of strain for a Cr-Co-Ni fcc sample (a) without and (b) with carbon-doping. They represent the defects configurations observed for (a) A-HPT and (b) C-HPT.

Figure 8.18a also represents the commonly reported configuration for Cr-Co-Ni alloys at high strain levels and/or lower temperatures. Based solely on quantity, the increase in the fraction of this types of obstacles to dislocation motion in C-HPT (mostly SFs), when compared to A-HPT (SFs, nanotwins and hcp/fcc boundaries) should be partly responsible for the increase in hardness. Nevertheless, the fraction of grain boundaries is also higher since the structure is more refined. Another effect that could be responsible for the higher hardness is the presence of the $M_{23}C_6$ precipitate. However, microhardness tests comparing regions with a carbide concentration versus those with no apparent precipitation showed no significant difference. And, as discussed in section 6, there was no significant contribution of the carbide distribution to the hardness outside the indirect effect of grain refinement.

In summary, carbon as an interstitial raised the SFE and refined the grain sizes. Coupled with the drag effect, CD has led to TWIP and TRIP deactivation. As such, the $Cr_{39.6}Co_{30}Ni_{30}C_{0.4}$ alloy processed via HPT developed a nanostructured network of SFs. This, combined with the interstitial solid solution strengthening and grain refinement resulted in higher values of hardness when compared to the unalloyed HPT sample, whilst maintaining a certain degree of ductility. Alternatively, the $Cr_{40}Co_{30}Ni_{30}$ alloy showed a nanotwin-hcp lamellae configuration after the severe plastic deformation even at room temperature and with a UFG substructure.

9 OVERALL EVALUATION OF CARBON-DOPING

On sections 5 through 8 of this dissertation, the discussion focused mostly on the initial processing stages and then at the different processing routes respectively. Here it will be stablished the overall observed effects of carbon-doping on the studied $Cr_{40}Co_{30}Ni_{30}$ alloy. When comparing the S and NS routes it is important to point out that the "solution treatment" was in regard to the material C. The $Cr_{40}Co_{30}Ni_{30}$ and $Cr_{39.9}Co_{30}Ni_{30}C_{0.1}$ alloys did not have any precipitation prior to the annealing at 900 °C. As such, the only differences between routes for these materials were the amount of stored deformation before annealing and the prior grain size.

The carbides' distributions for material C in the NS route (and for the C2 and C3 samples) were coarser and more heterogeneously concentrated in grain boundaries than for the solution treatment (S) processing route. As discussed in section 3.4.1 of this work, the particle distribution affects the Smith-Zener pinning pressure (SZPP) and the limiting grain size. Comparing equations 3.10 (homogeneous dispersion with particle interspacing, l_p, smaller than the average grain size: Figure 3.11c) and 3.18 (heterogeneous dispersion: Figure 3.11d) the SZPP is higher for the former. This could be the main explanation for why the increase in hardness (in relation to $Cr_{40}Co_{30}Ni_{30}$) for the C samples were subpar when compared to the S route (Figure 7.1). Additionally, the carbides at the CNS-4h900 sample were significantly banded (Figure A.2), which can have variable values of SZPP depending on the ratio between L and h_B (equation 3.17).

After TMH there was a significant refinement and increase in hardness for C3 when comparing to A3 and B3; A hypothesis is that the SZPP was effective because of the larger grain size (12.9 µm, Figure 5.12) when compared to those of the samples annealed at 900 °C for 0.5 and 4 h (less than 4 µm for the S route, Figure 6.17) . To help evaluate why the NS route was less efficient, the predicted hardness was modeled with limiting grain sizes calculated with the theory discussed at section 3.4.1. As such, first it was important to determine how the $M_{23}C_6$ average particle size varied with time. A relationship between this parameter and time can be modeled by the Lifshitz, Slyzov and Wagner (LSW) theory, and is given by equation 9.1 [78–80].

$$r^3 - r_0^3 = \beta \cdot t \tag{9.1}$$

Where r_0 is the particle size at the start of the diffusion condition and β is a constant. The average particle size was measured with the ImageJ™ software for the CS-0.17h900, CS0.5h900, CS-4h900 and CS-30h900 samples. Considering a r_0 equal to zero, since most of the carbon was in solid solution, then the cube of the results were then plotted versus time (in hours) and is shown at Figure 9.1.

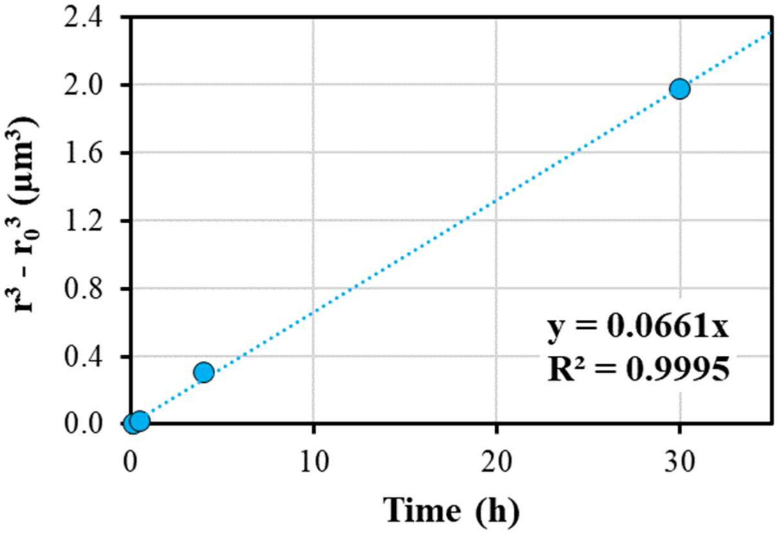

Figure 9.1. Relationship between the average particle ($M_{23}C_6$) size versus annealing time. For the $Cr_{39.6}Co_{30}Ni_{30}C_{0.4}$ alloy annealed at 900 °C in the solution treatment processing route.

From figure 9.1 it is possible to affirm that equation 9.1 models extremely well the particle growth for the $Cr_{39.6}Co_{30}Ni_{30}C_{0.4}$ alloy's carbides at 900 °C. With this, the limiting grain size for a homogeneous distribution versus time could be calculated combining equations 3.20 and 9.1. The result is shown in the left graph of Figure 9.2 by the blue curve. It must be noted that for simplification it was considered that both grain growth and precipitation start at the same time. Additionally, α was set as 0.1 and f_v considered constant (0.014 from figure 5.3). A similar modelling was also proposed for a heterogeneous distribution but with use of equation 3.21 (instead of 3.20), however with r_0 as the average particle size measured for the C2 sample (since it represents the carbide size for 0 s into annealing). This is represented by the grey curve in Figure 9.2 (left). At last, for a particle dispersion of planar banding, modeling was done with equation 3.22 (instead of 3.21) and with the r_0 observed for C2. L and h_B were measured for the CNS-4h900 sample, and the proposed curve (orange) is shown in the left side of Figure 9.2.

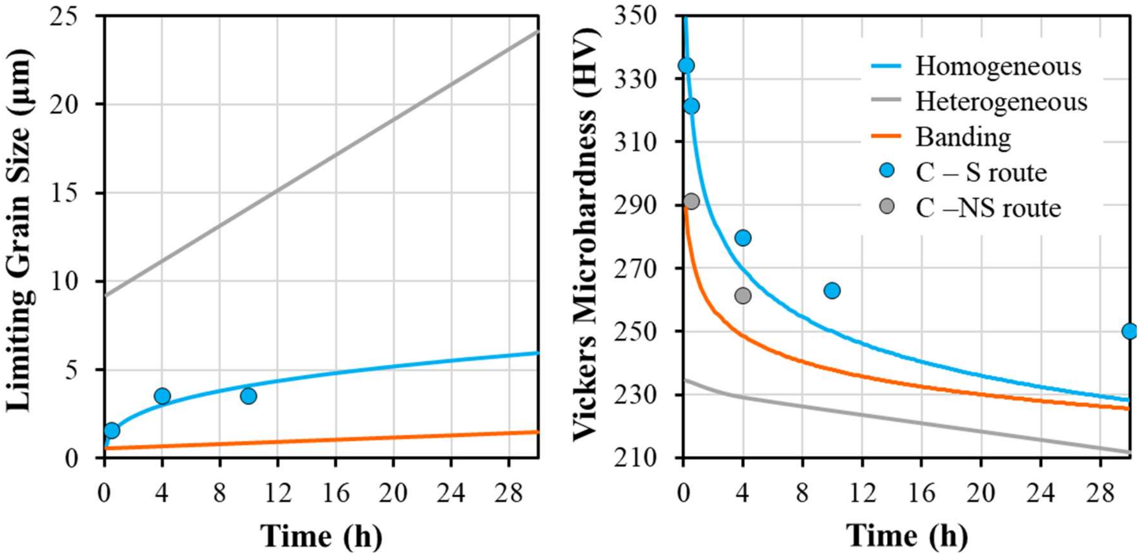

Figure 9.2. Predictions made for the $Cr_{39.6}Co_{30}Ni_{30}C_{0.4}$ alloy with the limiting grain size and Smith-Zener pinning pressure theories. Modeled for different particle distributions: heterogeneous (grey), homogeneous (blue) and with planar banding (orange). In the left, limiting grain size versus annealing time (at 900 °C) with particle size varying according to Figure 9.1

From Figure 9.2, it is interesting to observe that the limiting grain size modeled for particle banding is lower than for a homogeneous distribution in the same amount of annealing time. However, this is only true for the regions affected by the SZPP, which are those with the carbide bands, and in between SZPP tends to zero. This is what was observed for CNS-4h900 (Figure A.2d). The experimental points of the S processing route (blue dots) were well fitted by the limiting grain size modeling.

The right part of Figure 9.2 is an additional modeling that utilizes the limiting grain sizes from the left graph to estimate the decrease in hardness with time. For this, the HP equation obtained in Figure 6.24c was utilized. As such, the homogeneous and heterogeneous hardness curves were calculated simply by substituting the values from limiting grain size in the HP equation. However, for the scenario were precipitation occurs in planar bands, the hardness was modeled considering the individual contributions from the coarse and fine grained regions. Namely, for the regions with the bands of particles the values of limiting grain sizes from figure 9.2 (left) were utilized. Whereas, the contribution from the regions with carbide depletion was estimated with grain sizes predicted for the $Cr_{40}Co_{30}Ni_{30}$ alloy (Figure 6.19a). The fraction of hardness was them calculated with contributions of $h_B/(h_B + L)$ and and $L/(h_B + L)$ for the banding and single-phase regions respectively. This is a rough approximation since deformation can be concentrated in the “softer” regions with greater grain sizes.

It must be called out again that the modeling made for the curves in Figure 9.2 considers isolated cases. However, as discussed before, the samples in the NS route showed heterogeneously dispersed carbides, as well as particle banding. Additionally, a fraction of the particles was also consistently observed in the grains' bulk. As such, it is plausible to assume individual contributions from each of the models for the overall limiting grain size. Moreover, Figure 9.2 (right) seems to have predicted relatively well the hardness for the C samples in the NS route (grey dots), since the values calculated are the "minimal hardness" (i.e., relative to the limiting grain size). Additionally, it can be pointed out that since the curves predict a lower boundary and not the exact value, it is reasonable that the experimental data points for the S route are above (rather than below) the homogeneous curve. For the NS experimental points, banding seems to be the primary mode of particle distribution.

Regarding the $Cr_{39.6}Co_{30}Ni_{30}C_{0.4}$ sample processed by HPT, the average grain size achieved was significantly smaller than any predicted limiting grain size (Figure 8.6). This is a consequence of the severe plastic deformation. Nevertheless, the measured average hardness for C-HPT (which is virtually independent to the distance from the center of the disk due to saturation) was “only” 536 ± 25 HV (Figure 8.7). This value is significantly below the predicted from the Hall-Petch curve of Figure 6.24d (1067 HV). Likewise, the average hardness for A-HPT (472 ± 18 HV) also shown a subpar value. The values for both samples were plotted in the HP curve of Figure 6.d, and the result is shown in Figure 9.3

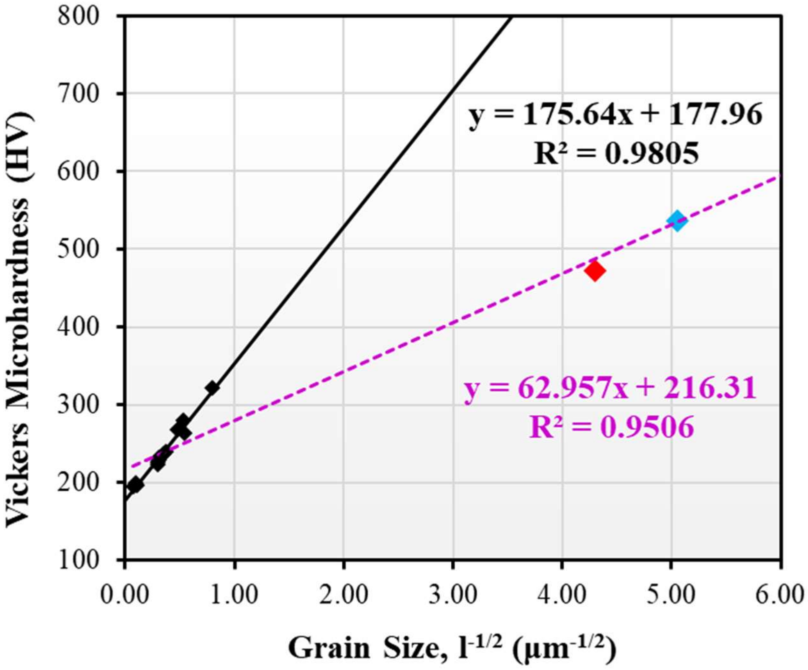

Figure 9.3. Hardness versus the negative inverse square root of grain size plot. In black, the results for the solution treatment processing route from Figure 6.24d (for the A, B and C materials) and their respective Hall-Petch curve and equation. The A-HPT and C-HPT experimental points are depicted by red and blue colors respectively. A linear relationship between all the data set contained in the figure was fitted (purple),

From Figure 9.3 it is possible to see that the HPT samples did not follow the general HP relationship obtained before (black). Their hardness values were significantly lower than expected, even though less than half of their grains were recrystallized (Figure 8.10). Alternatively, it is not unusual for HPT samples to show lower values of hardness in the as-processed condition due to the lack of grain relaxation [81]. Alas, it can be argued that the difference from the expected value would still be significant for both samples nonetheless. In any case, when both samples were also used to fit a HP relation with the data from the S route, the result obtained (purple) was rather good ($R^2 > 0.95$). Deviations from the HP relation are often reported, most consisting in a somewhat “inverse” Hall-Petch configuration after a minimal grain size (usually ~15 nm) [77,82]. This does not seem to be the case, since the measured hardness for C-HPT was considerably higher than for A-HPT (which has a larger grain size). From Figure 9.3 it seems that a weaking of the HP relation was experienced, since the new relation was well fitted. Nevertheless, the current data is insufficient to reach a conclusion since other matters could be influencing the hardness value, such as the difference between the substructures for A-HPT and C-HPT (Figure 8.18) and the presence of additional strengthening mechanisms.

10 CONCLUSIONS

In this work it was possible to study the effects of carbon-doping (CD) throughout different processing routes with the help of microstructural and mechanical analyses. More specifically, CD was evaluated in the presences of solution treatment, of a non-homogeneous particle dispersion and after severe plastic deformation processing (HPT). The main results observed were:

- A homogeneous distribution of $M_{23}C_6$ carbides was effective in retarding grain growth for 0.4 at.% CD, whereas for 0.1 at.% there was no significant increase in hardness;
- Carbon in solid solution (up to approximately 0.4 at.%) did not seem to significantly influence the hardness or grain size values. The main effect of CD appears to be inducing grain size refinement: the C samples fit well in the HP equation for the base alloy ($Cr_{40}Co_{30}Ni_{30}$);
- The absence of solution treatment led to a partly heterogeneous and partly banded particle distribution, that was less effective in retarding grain growth;
- For $Cr_{40}Co_{30}Ni_{30}$, severe plastic deformation induced a substructure of interpenetrated nanotwin-hcp lamellae even at room temperature and with the increase in SFE due to grain size refinement;
- CD deactivated TWIP and TRIP effects, resulting in a nanosized network of SFs;
- The classic theory for Smith-Zener pinning pressure and limiting grain sizes were able to model the predicted hardness for different particle distribution configurations;
- A deviation from the HP relation was observed for the alloys processed by HPT (which achieved UFG substructures). The new linear fit obtained with the addition of both these samples indicates a weakening in the HP relation rather than an inverse disposition.

10.1 Conclusões

Neste trabalho, foi possível estudar os efeitos da adição de carbono (AC) em diferentes rotas de processamento com a ajuda de análises microestruturais e mecânicas. Mais especificamente, o AC foi avaliado na presença de tratamento dissolução de precipitados, de uma dispersão não homogênea de partículas e após o processamento por deformação plástica severa (DPS). Os principais resultados observados foram:

- Uma distribuição homogênea de carbonetos $M_{23}C_6$ foi eficaz na retardação do crescimento de grãos para 0,4 at.% de AC, enquanto que para 0,1 at.% não houve aumento significativo na dureza;
- Carbono em solução sólida (até aproximadamente 0,4 at.%) não parece influenciar significativamente os valores de dureza ou tamanho de grão. O principal efeito da AC parece ser a redução do tamanho de grão: as amostras com C se encaixam bem na equação de HP (Hall-Petch) para a liga base ($Cr_{40}Co_{30}Ni_{30}$);
- A ausência de tratamento de dissolução resultou em uma distribuição de partículas parcialmente heterogênea e parcialmente em bandas, que foi menos eficaz na retardação do crescimento de grãos;
- Para a liga $Cr_{40}Co_{30}Ni_{30}$, a DPS induziu uma subestrutura de lamelas nanomaclas de fase hc (hexagonal compacta) interpenetradas, mesmo em temperatura ambiente e com o aumento na energia de falha de empilhamento (EFE) devido ao refino de grão;
- A AC desativou os efeitos TWIP e TRIP, resultando em uma rede nanométrica de FEs;
- A teoria clássica da pressão de ancoragem de Smith-Zener e tamanho de grão limite foi capaz de modelar a dureza prevista para diferentes configurações de distribuição de partículas;
- Foi observada uma divergência em relação a relação de HP para as ligas processadas por DPS (que alcançaram subestruturas com tamanhos de grão menores que 100 nm). O novo ajuste linear obtido com a adição dessas amostras indica um enfraquecimento na relação de HP em vez de uma relação inversa.

11 REFERENCES

[1] R.F. Tylecote, A History of Metallurgy, 2nd ed., Maney Publishing, London, 1992.

[2] S. Gorsse, J.P. Couzinié, D.B. Miracle, From high-entropy alloys to complex concentrated alloys, Comptes Rendus Phys. 19 (2018) 721–736. https://doi.org/10.1016/j.crhy.2018.09.004.

[3] B. Cantor, Multicomponent and high entropy alloys, Entropy. 16 (2014) 4749–4768. https://doi.org/10.3390/e16094749.

[4] A. Inoue, Stabilization of metallic supercooled liquid and bulk amorphous alloys, Acta Mater. 48 (2000) 279–306. https://doi.org/10.1016/S1359-6454(99)00300-6.

[5] B. Cantor, K.B. Kim, P.J. Warren, Novel multicomponent amorphous alloys, Mater. Sci. Forum. 386–388 (2002) 27–32. https://doi.org/10.4028/www.scientific.net/msf.386-388.27.

[6] H.S. Oh, S.J. Kim, K. Odbadrakh, W.H. Ryu, K.N. Yoon, S. Mu, F. Körmann, Y. Ikeda, C.C. Tasan, D. Raabe, T. Egami, E.S. Park, Engineering atomic-level complexity in high-entropy and complex concentrated alloys, Nat. Commun. 10 (2019). https://doi.org/10.1038/s41467-019-10012-7.

[7] M.C.G. Gao, J.-W. Yeh, P.K. Liaw, Y. Zhang, High-Entropy Alloys, 1st ed., Springer International Publishing, Cham, 2016. https://doi.org/10.1007/978-3-319-27013-5.

[8] B. Cantor, I.T.H. Chang, P. Knight, A.J.B. Vincent, Microstructural development in equiatomic multicomponent alloys, Mater. Sci. Eng. A. 375–377 (2004) 213–218. https://doi.org/10.1016/j.msea.2003.10.257.

[9] J.W. Yeh, S.K. Chen, S.J. Lin, J.Y. Gan, T.S. Chin, T.T. Shun, C.H. Tsau, S.Y. Chang, Nanostructured high-entropy alloys with multiple principal elements: Novel alloy design concepts and outcomes, Adv. Eng. Mater. 6 (2004) 299–303. https://doi.org/10.1002/adem.200300567.

[10] F.G. Coury, G. Zepon, C. Bolfarini, Multi-principal element alloys from the CrCoNi family: outlook and perspectives, J. Mater. Res. Technol. 15 (2021) 3461–3480. https://doi.org/10.1016/j.jmrt.2021.09.095.

[11] D.B. Miracle, O.N. Senkov, A critical review of high entropy alloys and related concepts, Acta Mater. 122 (2017) 448–511. https://doi.org/10.1016/j.actamat.2016.08.081.

[12] F. Otto, Y. Yang, H. Bei, E.P. George, Relative effects of enthalpy and entropy on the phase stability of equiatomic high-entropy alloys, Acta Mater. 61 (2013) 2628–2638. https://doi.org/10.1016/j.actamat.2013.01.042.

[13] J.W. Yeh, Alloy design strategies and future trends in high-entropy alloys, JOM. 65 (2013) 1759–1771. https://doi.org/10.1007/s11837-013-0761-6.

[14] C. Varvenne, A. Luque, W.A. Curtin, Theory of strengthening in fcc high entropy alloys, Acta Mater. 118 (2016) 164–176. https://doi.org/10.1016/j.actamat.2016.07.040.

[15] J. Liu, X. Wang, A.P. Singh, H. Xu, F. Kong, F. Yang, The evolution of intermetallic compounds in high-entropy alloys: From the secondary phase to the main phase, Metals (Basel). 11 (2021). https://doi.org/10.3390/met11122054.

[16] E.P. George, W.A. Curtin, C.C. Tasan, High entropy alloys: A focused review of mechanical properties and deformation mechanisms, Acta Mater. 188 (2020) 435–474. https://doi.org/10.1016/j.actamat.2019.12.015.

[17] Z. Wu, H. Bei, G.M. Pharr, E.P. George, ScienceDirect Temperature dependence of the mechanical properties of equiatomic solid solution alloys with face-centered cubic crystal structures, 81 (2014) 428–441. https://doi.org/10.1016/j.actamat.2014.08.026.

[18] Z. Wu, H. Bei, F. Otto, G.M. Pharr, E.P. George, Intermetallics Recovery , recrystallization , grain growth and phase stability of a family of FCC-structured multi-component equiatomic solid solution alloys, 46 (2014) 131–140. https://doi.org/10.1016/j.intermet.2013.10.024.

[19] Y.-C. Huang, C.-H. Su, S.-K. Wu, C. Lin, A Study on the Hall – Petch Relationship and Grain Growth Kinetics in FCC-Structured High/Medium Entropy Alloys, Entropy. 21 (2019) 13. https://doi.org/10.3390/e21030297.

[20] G. Laplanche, A. Kostka, C. Reinhart, J. Hunfeld, G. Eggeler, E.P. George, Reasons for the superior mechanical properties of medium-entropy CrCoNi compared to high-entropy CrMnFeCoNi, Acta Mater. 128 (2017) 292–303. https://doi.org/10.1016/j.actamat.2017.02.036.

[21] B. Gludovatz, A. Hohenwarter, K.V.S. Thurston, H. Bei, Z. Wu, E.P. George, R.O. Ritchie, Exceptional damage-tolerance of a medium-entropy alloy CrCoNi at cryogenic temperatures, Nat. Commun. 7 (2016) 1–8.

https://doi.org/10.1038/ncomms10602.

[22] C. Niu, C.R. LaRosa, J. Miao, M.J. Mills, M. Ghazisaeidi, Magnetically-driven phase transformation strengthening in high entropy alloys, Nat. Commun. 9 (2018) 1–9. https://doi.org/10.1038/s41467-018-03846-0.

[23] R. Abbaschian, L. Abbaschian, R.E. Reed-Hill, Physical Metallurgy Principles, 4th ed., Cngage Learning, Stamford, n.d.

[24] D. Hull, D.J. Bacon, Introduction to Dislocations, 5th ed., Elsevier Ltd, Oxford, n.d.

[25] D.A. Porter, K.E. Easterling, M.Y. Sherif, Phase Transformations in Metals and Alloys, 3rd ed., Taylor & Francis Group, Boca Raton, 2009.

[26] S. Kibey, J.B. Liu, D.D. Johnson, H. Sehitoglu, Predicting twinning stress in fcc metals: Linking twin-energy pathways to twin nucleation, Acta Mater. 55 (2007) 6843–6851. https://doi.org/10.1016/j.actamat.2007.08.042.

[27] G. Bertoli, L.B. Otani, A.J. Clarke, C.S. Kiminami, F.G. Coury, Hall-Petch and grain growth kinetics of the low stacking fault energy TRIP Cr40Co40Ni20 multi-principal element alloy, Appl. Phys. Lett. 119 (2021). https://doi.org/10.1063/5.0057888.

[28] W. Li, S. Lu, Q.M. Hu, S.K. Kwon, B. Johansson, L. Vitos, Generalized stacking fault energies of alloys, J. Phys. Condens. Matter. 26 (2014). https://doi.org/10.1088/0953-8984/26/26/265005.

[29] X.H. An, S.D. Wu, Z.G. Wang, Z.F. Zhang, Significance of stacking fault energy in bulk nanostructured materials: Insights from Cu and its binary alloys as model systems, Prog. Mater. Sci. 101 (2019) 1–45. https://doi.org/10.1016/j.pmatsci.2018.11.001.

[30] J. Miao, C.E. Slone, T.M. Smith, C. Niu, H. Bei, M. Ghazisaeidi, G.M. Pharr, M.J. Mills, The evolution of the deformation substructure in a Ni-Co-Cr equiatomic solid solution alloy, Acta Mater. 132 (2017) 35–48. https://doi.org/10.1016/j.actamat.2017.04.033.

[31] Y. Chen, X. An, Z. Zhou, P. Munroe, S. Zhang, X. Liao, Z. Xie, Size-dependent deformation behavior of dual-phase, nanostructured CrCoNi medium-entropy alloy, Sci. China Mater. 64 (2021) 209–222. https://doi.org/10.1007/s40843-020-1377-2.

[32] S. Zhao, Z. Li, C. Zhu, W. Yang, Z. Zhang, D.E.J. Armstrong, P.S. Grant, R.O. Ritchie, M.A. Meyers, Amorphization in extreme deformation of the CrMnFeCoNi high-entropy alloy, Sci. Adv. 7 (2021) 1–7. https://doi.org/10.1126/SCIADV.ABB3108.

[33] D. Liu, Q. Yu, S. Kabra, M. Jiang, P. Forna-Kreutzer, R. Zhang, M. Payne, F. Walsh, B. Gludovatz, M. Asta, A.M. Minor, E.P. George, R.O. Ritchie, Exceptional fracture toughness of CrCoNi-based medium- and high-entropy alloys at 20 kelvin, Science (80-.). 378 (2022) 978–983. https://doi.org/10.1126/science.abp8070.

[34] C.E. Slone, J. Miao, E.P. George, M.J. Mills, Achieving ultra-high strength and ductility in equiatomic CrCoNi with partially recrystallized microstructures, Acta Mater. 165 (2019) 496–507. https://doi.org/10.1016/j.actamat.2018.12.015.

[35] W. Guo, Z. Pei, X. Sang, J.D. Poplawsky, S. Bruschi, J. Qu, D. Raabe, H. Bei, Shape-preserving machining produces gradient nanolaminate medium entropy alloys with high strain hardening capability, Acta Mater. 170 (2019) 176–186. https://doi.org/10.1016/j.actamat.2019.03.024.

[36] Y. Ma, M. Yang, F. Yuan, X. Wu, Deformation induced hcp nano-lamella and its size effect on the strengthening in a CoCrNi medium-entropy alloy, J. Mater. Sci. Technol. 82 (2021) 122–134. https://doi.org/10.1016/j.jmst.2020.12.017.

[37] S. Bajpai, B.E. MacDonald, T.J. Rupert, H. Hahn, E.J. Lavernia, D. Apelian, Recent progress in the CoCrNi alloy system, Materialia. 24 (2022) 101476. https://doi.org/10.1016/j.mtla.2022.101476.

[38] F.C. Puosso, G. Bertoli, F.G. Coury, A Hall–Petch study of the high toughness Cr40Co30Ni30 multi-principal element alloy, J. Mater. Res. (2022) 1–13. https://doi.org/10.1557/s43578-022-00729-5.

[39] L. Ding, A. Hilhorst, H. Idrissi, P.J. Jacques, Potential TRIP/TWIP coupled effects in equiatomic CrCoNi medium-entropy alloy, Acta Mater. 234 (2022) 118049. https://doi.org/10.1016/j.actamat.2022.118049.

[40] D. Xu, M. Wang, T. Li, X. Wei, Y. Lu, A critical review of the mechanical properties of CoCrNi-based medium-entropy alloys, Microstructures. (2022). https://doi.org/10.20517/microstructures.2021.10.

[41] N.N. Greenwood, A. Earnshaw, Chemistry of the Elements, 2nd ed., Elsevier Ltd,

1997.

[42] J. Humphreys, G.S. Rohrer, A. Rollett, Recrystallization and Related Annealing Phenomena, 2nd ed., Elsevier, 2004. https://doi.org/10.1016/B978-0-08-044164-1.X5000-2.

[43] K. Lu, Stabilizing nanostructures in metals, (2016). https://doi.org/10.1038/natrevmats.2016.19.

[44] J. Hu, Y.N. Shi, X. Sauvage, G. Sha, K. Lu, Grain boundary stability governs hardening and softening in extremely fine nanograined metals, Science (80-.). 355 (2017) 1292–1296. https://doi.org/10.1126/science.aal5166.

[45] B. Yin, S. Yoshida, N. Tsuji, W.A. Curtin, Yield strength and misfit volumes of NiCoCr and implications for short-range-order, Nat. Commun. (n.d.) 1–7. https://doi.org/10.1038/s41467-020-16083-1.

[46] S. Yoshida, T. Ikeuchi, T. Bhattacharjee, Y. Bai, Acta Materialia Effect of elemental combination on friction stress and Hall-Petch relationship in face-centered cubic high / medium entropy alloys, Acta Mater. 171 (2019) 201–215. https://doi.org/10.1016/j.actamat.2019.04.017.

[47] M. Schneider, F. Werner, D. Langenkämper, C. Reinhart, Effect of Temperature and Texture on Hall – Petch Strengthening by Grain and Annealing Twin Boundaries in the MnFeNi Medium-Entropy Alloy, (2019). https://doi.org/10.3390/met9010084.

[48] H. Huang, X. Li, Z. Dong, W. Li, S. Huang, D. Meng, X. Lai, T. Liu, S. Zhu, L. Vitos, Critical stress for twinning nucleation in CrCoNi-based medium and high entropy alloys, Acta Mater. 149 (2018) 388–396. https://doi.org/10.1016/j.actamat.2018.02.037.

[49] M. Zhang, Q. Yu, C. Frey, F. Walsh, M.I. Payne, P. Kumar, D. Liu, T.M. Pollock, M.D. Asta, R.O. Ritchie, A.M. Minor, Determination of peak ordering in the CrCoNi medium-entropy alloy via nanoindentation, Acta Mater. 241 (2022) 118380. https://doi.org/https://doi.org/10.1016/j.actamat.2022.118380.

[50] K. Edalati, A. Bachmaier, V.A. Beloshenko, Y. Beygelzimer, V.D. Blank, W.J. Botta, K. Bryła, J. Čížek, S. Divinski, N.A. Enikeev, Y. Estrin, G. Faraji, R.B. Figueiredo, M. Fuji, T. Furuta, T. Grosdidier, J. Gubicza, A. Hohenwarter, Z. Horita, J. Huot, Y. Ikoma, M. Janeček, M. Kawasaki, P. Král, S. Kuramoto, T.G.

Langdon, D.R. Leiva, V.I. Levitas, A. Mazilkin, M. Mito, H. Miyamoto, T. Nishizaki, R. Pippan, V. V. Popov, E.N. Popova, G. Purcek, O. Renk, Á. Révész, X. Sauvage, V. Sklenicka, W. Skrotzki, B.B. Straumal, S. Suwas, L.S. Toth, N. Tsuji, R.Z. Valiev, G. Wilde, M.J. Zehetbauer, X. Zhu, Nanomaterials by severe plastic deformation: review of historical developments and recent advances, Mater. Res. Lett. 10 (2022) 163–256. https://doi.org/10.1080/21663831.2022.2029779.

[51] B.L. Bramfitt, A.O. Benscoter, Metallographer's Guide Practices and Procedures for Irons and Steels, ASM International, 2002.

[52] A. INTERNATIONAL, Standard Test Methods for Determining Average Grain Size, Astm E112-10. (2010) 1–27. https://doi.org/10.1520/E0112-13.1.4.

[53] V.A. Vorontsov, L. Kovarik, M.J. Mills, C.M.F. Rae, High-resolution electron microscopy of dislocation ribbons in a CMSX-4 superalloy single crystal, Acta Mater. 60 (2012) 4866–4878. https://doi.org/10.1016/j.actamat.2012.05.014.

[54] ASTM International, Standard Test Method for Microindentation Hardness of Materials, Am. Soc. Test. Mater. Handb. (2017) 281–293. https://doi.org/10.1520/E0384-17.

[55] A.P. Carvalho, L.M. Reis, R.P.R.P. Pinheiro, P.H.R. Pereira, T.G. Langdon, R.B. Figueiredo, Using Plane Strain Compression Test to Evaluate the Mechanical Behavior of Magnesium Processed by HPT, (2022).

[56] J. Gegner, Decarburization - controlled internal oxidation of rolling bearing steel SAE 52100 at the dissociation pressure of wüstite, Int. J. Mater. Res. 94 (2003) 30–35.

[57] A. Kruk, A. Gil, S. Lech, G. Cempura, A. Agüero, A. Czyrska-Filemonowicz, Multiscale characterization of an oxide scale formed on the creep-resistant ati 718plus superalloy during high-temperature oxidation, Materials (Basel). 14 (2021). https://doi.org/10.3390/ma14216327.

[58] D.J. Young, Alloy Oxidation II, in: High Temp. Oxid. Corros. Met., Elsevier, 2016: pp. 261–333. https://doi.org/10.1016/B978-0-08-100101-1.00006-6.

[59] C. Stephan-Scherb, W. Schulz, M. Schneider, S. Karafiludis, G. Laplanche, (2021) Stephan-Scherb C. - High-Temperature Oxidation in Dry and Humid Atmospheres of the Equiatomic CrMnFeCoNi and CrCoNiHigh- and Medium-Entropy Alloys.pdf, Oxid. Met. 95 (2020) 105–133. https://doi.org/10.1007/s11085-020-

10014-7.

[60] P. Xue, L. Zhu, P. Xu, H. Lu, S. Wang, Z. Yang, J. Ning, S.L. Sing, Y. Ren, Microstructure evolution and enhanced mechanical properties of additively manufactured CrCoNi medium-entropy alloy composites, J. Alloys Compd. 928 (2022) 167169. https://doi.org/10.1016/j.jallcom.2022.167169.

[61] I. Moravcik, V. Hornik, P. Minárik, L. Li, I. Dlouhy, M. Janovska, D. Raabe, Z. Li, Interstitial doping enhances the strength-ductility synergy in a CoCrNi medium entropy alloy, Mater. Sci. Eng. A. 781 (2020) 1–14. https://doi.org/10.1016/j.msea.2020.139242.

[62] D.B. Williams, C.B. Carter, Transmission Electron Microscopy, 2nd ed., Springer US, Boston, MA, 2009. https://doi.org/10.1007/978-0-387-76501-3.

[63] I. V. Minin, O. V. Minin, Elements of diffraction quasi-optics, 1994.

[64] W.D. Callister, D.G. Rethwisch, Materials Science and Engineering: An Introduction, 10th ed., Wiley-VCH Verlag, 2019. https://www.wiley.com/en-us/Materials+Science+and+Engineering%3A+An+Introduction%2C+10th+Edition-p-9781119405498.

[65] J. Rackwitz, Q. Yu, Y. Yang, G. Laplanche, E.P. George, A.M. Minor, R.O. Ritchie, Acta Materialia Effects of cryogenic temperature and grain size on fatigue-crack propagation in the medium-entropy CrCoNi alloy, Acta Mater. 200 (2020) 351–365. https://doi.org/10.1016/j.actamat.2020.09.021.

[66] P. Xue, L. Zhu, J. Ning, P. Xu, S. Wang, Z. Yang, The crystallographic texture and dependent mechanical properties of the CrCoNi medium-entropy alloy by laser remelting strategy, J. Mater. Sci. Technol. 111 (2022) 245–255. https://doi.org/10.1016/j.jmst.2021.08.094.

[67] Y.Y. Shang, Y. Wu, J.Y. He, X.Y. Zhu, S.F. Liu, H.L. Huang, K. An, Y. Chen, S.H. Jiang, H. Wang, X.J. Liu, Z.P. Lu, Solving the strength-ductility tradeoff in the medium-entropy NiCoCr alloy via interstitial strengthening of carbon, Intermetallics. 106 (2019) 77–87. https://doi.org/10.1016/j.intermet.2018.12.009.

[68] H. Azzeddine, D. Bradai, T. Baudin, T.G. Langdon, Texture evolution in high-pressure torsion processing, Prog. Mater. Sci. 125 (2022) 100886. https://doi.org/10.1016/j.pmatsci.2021.100886.

[69] B.C. De Cooman, Y. Estrin, S.K. Kim, Twinning-induced plasticity (TWIP) steels,

Acta Mater. 142 (2018) 283–362. https://doi.org/10.1016/j.actamat.2017.06.046.

[70] J.H. Jun, C.S. Choi, Variation of stacking fault energy with austenite grain size and its effect on the MS temperature of γ → ε martensitic transformation in Fe-Mn alloy, Mater. Sci. Eng. A. 257 (1998) 353–356. https://doi.org/10.1016/S0921-5093(98)00994-0.

[71] S.J. Lee, J. Han, S. Lee, S.H. Kang, S.M. Lee, Y.K. Lee, Design for Fe-high Mn alloy with an improved combination of strength and ductility, Sci. Rep. 7 (2017) 1–9. https://doi.org/10.1038/s41598-017-03862-y.

[72] A. Saeed-Akbari, J. Imlau, U. Prahl, W. Bleck, Derivation and variation in composition-dependent stacking fault energy maps based on subregular solution model in high-manganese steels, Metall. Mater. Trans. A Phys. Metall. Mater. Sci. 40 (2009) 3076–3090. https://doi.org/10.1007/s11661-009-0050-8.

[73] Y. Lee, C. Choi, Driving force for γ→ε martensitic transformation and stacking fault energy of γ in Fe-Mn binary system, Metall. Mater. Trans. A. 31 (2000) 355–360. https://doi.org/10.1007/s11661-000-0271-3.

[74] H. He, M. Naeem, F. Zhang, Y. Zhao, S. Harjo, T. Kawasaki, B. Wang, X. Wu, S. Lan, Z. Wu, W. Yin, Y. Wu, Z. Lu, J.J. Kai, C.T. Liu, X.L. Wang, Stacking Fault Driven Phase Transformation in CrCoNi Medium Entropy Alloy, Nano Lett. 21 (2021) 1419–1426. https://doi.org/10.1021/acs.nanolett.0c04244.

[75] K. Gan, D. Yan, S. Zhu, Z. Li, Interstitial effects on the incipient plasticity and dislocation behavior of a metastable high-entropy alloy: Nanoindentation experiments and statistical modeling, Acta Mater. 206 (2021) 116633. https://doi.org/10.1016/j.actamat.2021.116633.

[76] H. Chang, T.W. Zhang, S.G. Ma, D. Zhao, R.L. Xiong, T. Wang, Z.Q. Li, Z.H. Wang, Novel Si-added CrCoNi medium entropy alloys achieving the breakthrough of strength-ductility trade-off, Mater. Des. 197 (2021) 0–11. https://doi.org/10.1016/j.matdes.2020.109202.

[77] R. Liu, J. Tang, J. Jiang, X. Li, Y. Wei, Stacking fault induced hardening and grain size effect in nanocrystalline CoNiCrFeMn high-entropy alloy, Extrem. Mech. Lett. 56 (2022) 101875. https://doi.org/10.1016/j.eml.2022.101875.

[78] D.A. Santana, K.R. Santos, C.S. Kiminami, F.G. Coury, Design, phase equilibria, and coarsening kinetics of a new γ/γ′ precipitation-hardened multi-principal

element alloy, J. Alloys Compd. 882 (2021) 160729. https://doi.org/10.1016/j.jallcom.2021.160729.

[79] I.M. Lifshitz, V. V. Slyozov, The kinetics of precipitation from supersaturated solid solutions, J. Phys. Chem. Solids. 19 (1961) 35–50. https://doi.org/10.1016/0022-3697(61)90054-3.

[80] C. Wagner, Theory of the aging of precipitation by dissolution (Ostwald maturation), Rep. Bunsen Soc. Phys. Chem. 65 (1961) 581–591. http://onlinelibrary.wiley.com/doi/10.1002/bbpc.19610650704/abstract.

[81] S. Praveen, J.W. Bae, P. Asghari-Rad, J.M. Park, H.S. Kim, Annealing-induced hardening in high-pressure torsion processed CoCrNi medium entropy alloy, Mater. Sci. Eng. A. 734 (2018) 338–340. https://doi.org/10.1016/j.msea.2018.07.107.

[82] S.N. Naik, S.M. Walley, The Hall–Petch and inverse Hall–Petch relations and the hardness of nanocrystalline metals, J. Mater. Sci. 55 (2020) 2661–2681. https://doi.org/10.1007/s10853-019-04160-w.

12 APPENDIX A

Figure A.1. Macrography for the C2 sample. Scale in cm. The microstructure was equivalent for A2 and B2 samples.

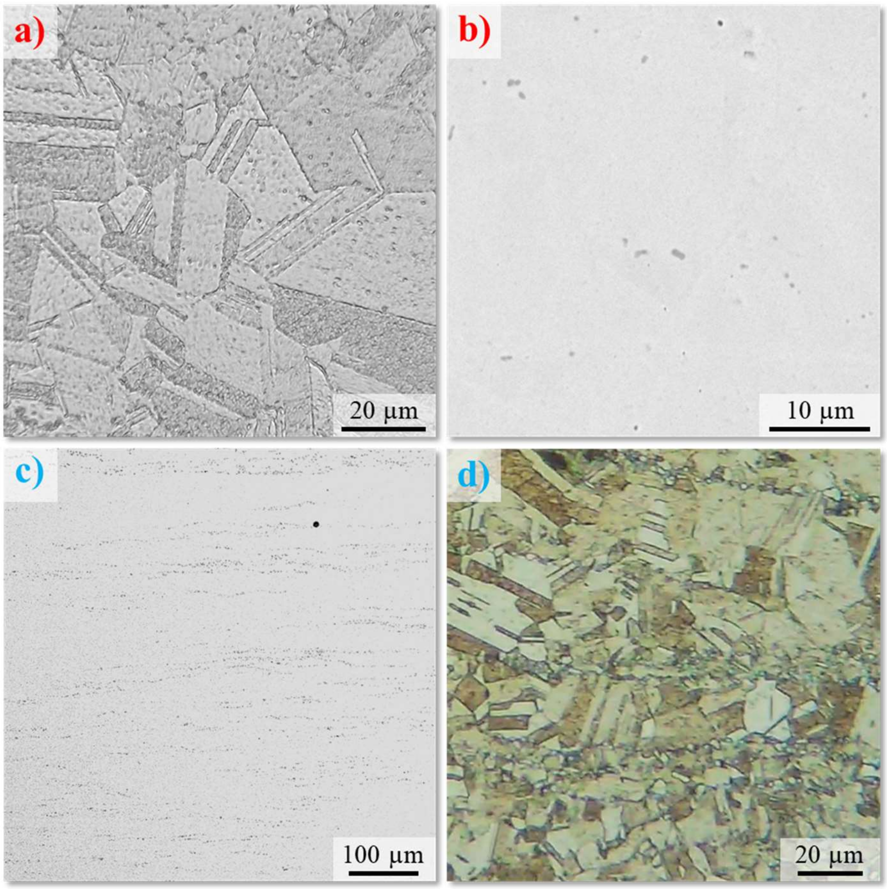

Figure A.2. Microstructural characterization of the $Cr_{40}Co_{30}Ni_{30}$ (a-b) and $Cr_{39.6}Co_{30}Ni_{30}C_{0.4}$ (c-d) samples after annealing at 900 °C for 4 h in the NS processing route. OM imaging and etching with Kallings N°II (a and d) and SEM-BSE (b-c).

Sample	Processing Route
A1	As-Cast
B1	
C1	
A2	$\mathrm{IA}_{10\ \mathrm{h}}^{1100^\circ\mathrm{C}}$
B2	
C2	
A3	$\mathrm{TMH} = \mathrm{H}_{10\ \mathrm{h}}^{1100^\circ\mathrm{C}}\ \mathrm{CR}_{50\ \%}\ \mathrm{IA}_{1\ \mathrm{h}}^{1100^\circ\mathrm{C}}\ \mathrm{CR}_{35\ \%}\ \mathrm{IA}_{1\ \mathrm{h}}^{1100^\circ\mathrm{C}}$
B3	
C3	
A4	$\mathrm{TMH} > \mathrm{CR}_{50\ \%}$
B4	
C4	
AS	$\mathrm{TMH} > \mathrm{CR}_{50\ \%} > \mathrm{ST}_{1\ \mathrm{h}}^{1195^\circ\mathrm{C}}$
BS	
CS	
AS-CR	$\mathrm{TMH} > \mathrm{CR}_{50\ \%} > \mathrm{ST}_{1\ \mathrm{h}}^{1195^\circ\mathrm{C}} > \mathrm{CR}_{75\ \%}$
BS-CR	
CS-CR	
AS-0.17h900	$\mathrm{TMH} > \mathrm{CR}_{50\ \%} > \mathrm{ST}_{1\ \mathrm{h}}^{1195^\circ\mathrm{C}} > \mathrm{CR}_{75\ \%} > \mathrm{A}_{10\ \mathrm{min}}^{900^\circ\mathrm{C}}$
BS-0.17h900	
CS-0.17h900	
AS-0.5h900	$\mathrm{TMH} > \mathrm{CR}_{50\ \%} > \mathrm{ST}_{1\ \mathrm{h}}^{1195^\circ\mathrm{C}} > \mathrm{CR}_{75\ \%} > \mathrm{A}_{30\ \mathrm{min}}^{900^\circ\mathrm{C}}$
BS-0.5h900	
CS-0.5h900	
AS-4h900	$\mathrm{TMH} > \mathrm{CR}_{50\ \%} > \mathrm{ST}_{1\ \mathrm{h}}^{1195^\circ\mathrm{C}} > \mathrm{CR}_{75\ \%} > \mathrm{A}_{4\ \mathrm{h}}^{900^\circ\mathrm{C}}$
BS-4h900	
CS-4h900	
AS-10h900	$\mathrm{TMH} > \mathrm{CR}_{50\ \%} > \mathrm{ST}_{1\ \mathrm{h}}^{1195^\circ\mathrm{C}} > \mathrm{CR}_{75\ \%} > \mathrm{A}_{10\ \mathrm{h}}^{900^\circ\mathrm{C}}$
BS-10h900	
CS-10h900	
AS-30h900	$\mathrm{TMH} > \mathrm{CR}_{50\ \%} > \mathrm{ST}_{1\ \mathrm{h}}^{1195^\circ\mathrm{C}} > \mathrm{CR}_{75\ \%} > \mathrm{A}_{30\ \mathrm{h}}^{900^\circ\mathrm{C}}$
BS-30h900	
CS-30h1100	
AS-0.5h1100	$\mathrm{TMH} > \mathrm{CR}_{50\ \%} > \mathrm{ST}_{1\ \mathrm{h}}^{1195^\circ\mathrm{C}} > \mathrm{CR}_{75\ \%} > \mathrm{A}_{0.5\ \mathrm{h}}^{1100^\circ\mathrm{C}}$
CS-0.5h1100	
AS-4h1100	$\mathrm{TMH} > \mathrm{CR}_{50\ \%} > \mathrm{ST}_{1\ \mathrm{h}}^{1195^\circ\mathrm{C}} > \mathrm{CR}_{75\ \%} > \mathrm{A}_{4\ \mathrm{h}}^{1100^\circ\mathrm{C}}$
CS-4h1100	
ANS-0.5h900	$\mathrm{TMH} > \mathrm{CR}_{50\ \%} > \mathrm{A}_{0.5\ \mathrm{h}}^{900^\circ\mathrm{C}}$
BNS-0.5h900	
CNS-0.5h900	
ANS-4h900	$\mathrm{TMH} > \mathrm{CR}_{50\ \%} > \mathrm{A}_{4\ \mathrm{h}}^{900^\circ\mathrm{C}}$
BNS-4h900	
CNS-4h900	
A-HPT	$\mathrm{TMH} > \mathrm{HPT}_{5\ \mathrm{turns}}$
C-HPT	

Figure A.3. Nominal identification for all samples and their respective processing.

13 APPENDIX B

Here, the code used for the Center of Symmetry (COS) is described. The analysis was carried out for the atomic resolution HAADF-STEM images. This technique facilitates the visualization of changes in the FCC stacking sequence, since it measures the distance of the center of the atoms to each of their six nearest neighbors. As such, stacking faults and HCP regions appear highlighted as rows (or multiple rows) of atoms in the COS maps (from dark to light blue, for example). The coding for this analysis was made following the guideline proposed by Vorontsov et al [53] and is written below.

```
% MATLAB (filter image to increase quality and then find the center of each atom):
A = imread(HAADF-TEM image.tif');
se = strel('disk',3,4);
B = imtophat(A,se);
C = rgb2gray(B);
D = imadjust (C);
E = imgaussfilt(D,0.5);
Filtered image = imgaussfilt(E,0.5);

image = imread("filtered image.tif");
image = rgb2gray(image);
A = image;
image = imcrop(image,[310 225 170 170]);
image = imresize(image, 2);
original_image = image;

se = strel("disk", 6);
image = imtophat(image, se);

PSF = fspecial("gaussian", 6, 6);
UNDERPSF = ones(size(PSF)-4);
OVERPSF = padarray(UNDERPSF, [6 6], "replicate", "both");
[image,P1] = deconvblind(image, OVERPSF);
```

```
image = imgaussfilt(image, 2);

image = imsharpen(image, 'Radius', 6, 'Amount', 1);

image = localcontrast(image, 1, 1);
image = imbinarize(image, 0.99);
se = strel('diamond',1);
image = imerode(image, se);
image = imdilate(image, se);
image = edge(image, 'Canny');

[c,r] = imfindcircles(image,[1,8]);

figure(1);
imshow(original_image);
hold on;
plot(c(:, 1), c(:, 2), '.k', 'MarkerSize', 2.5);

% Export vector “c” as a .csl file (values separated with comma)
% In Python (Google Colab for this example), import vector “c” and  run the code:
!pip install imagecodecs

import numpy as np
import pandas as pd
from scipy.spatial import cKDTree
import matplotlib.pyplot as plt
from scipy.ndimage.filters import gaussian_filter
import tifffile
PATH_CSV = "/content/c.csv"
data = pd.read_csv(PATH_CSV, header=None)
data = data.to_numpy().astype(float)
```

```
data.shape

plt.figure(figsize=(10, 10))
plt.scatter(data[:, 0], data[:, 1])
plt.show()

ctree = cKDTree(data)
_, inds =  ctree.query(data, 7)

plt.figure(figsize=(10, 10))
plt.scatter(data[:, 0], data[:, 1])
plt.scatter(data[inds[0], 0], data[inds[0], 1],)
plt.show()

symmetry_map = []
index = 0
for index in range(inds.shape[0]):
    central_point = data[inds[index, 0]]
    relative_positions = np.array([central_point - data[inds[index, i]] for i in range(1, 7)])

    list_smallest_distance = list()
    for position in relative_positions:
        list_modules = list()
        for position_compare in relative_positions:
            list_modules.append(np.linalg.norm(position + position_compare)**2)
        list_smallest_distance.append(min(list_modules))

    symmetry_parameter = (.5 * np.sum(list_smallest_distance)) / (2 *
np.sum([np.linalg.norm(i)**2 for i in relative_positions]))

    symmetry_map.append([*central_point, symmetry_parameter])
symmetry_map = np.array(symmetry_map)
```

```
symmetry_map

plt.figure(figsize=(10, 10))
plt.scatter(symmetry_map[:, 0], symmetry_map[:, 1], s=100, c=symmetry_map[:, 2],
cmap='gray')
plt.show()

plt.figure(figsize=(9, 9))
heatmap, xedges, yedges = np.histogram2d(symmetry_map[:, 0], symmetry_map[:, 1],
bins=100, weights=symmetry_map[:, 2])
extent = [xedges[0], xedges[-1], yedges[0], yedges[-1]]

#plt.imshow(image_data)
# plt.scatter(data[:, 0], data[:, 1])
plt.imshow(heatmap.T, extent=extent, origin='lower', alpha=0.8,
cmap=plt.get_cmap('jet') )
plt.show()

def myplot(x, y, s, bins=801):
   heatmap, xedges, yedges = np.histogram2d(x, y, bins=bins, weights=s)
   heatmap = gaussian_filter(heatmap, sigma=3)

   extent = [xedges[0], xedges[-1], yedges[0], yedges[-1]]
   return heatmap.T, extent

bins = 801
slice_size = (14, 787), (14, 787)

img, extent = myplot(x=symmetry_map[:, 0],
                     y=symmetry_map[:, 1],
                     s=symmetry_map[:, 2],
```

```
                   bins=bins)
scatter_correction = (bins - extent[1] + slice_size[0][0],
                    bins - extent[3] + slice_size[1][0])

plt.figure(figsize=(21, 9))
plt.imshow(img[slice_size[0][0]:slice_size[0][1],slice_size[1][0]:slice_size[1][1]],
          origin='lower',
          cmap=plt.get_cmap('jet'),
          alpha=1)
# plt.imshow(img,
#           origin='lower',
#           cmap=plt.get_cmap('jet'),
#           alpha=1)
plt.scatter(symmetry_map[:, 0] - scatter_correction[0], symmetry_map[:, 1] - scatter_correction[1], s=0, color="black")
plt.show()
```

% The value for bins should be equivalent to the maximum value for the centroids in vector “c”.